LEABHARLANN CHOLÁISTE NA TRÍONÓIDE, BAILE ÁTHA CLIATH
Ollscoil Átha Cliath

TRINITY COLLEGE LIBRARY DUBLIN
The University of Dublin

Terms and Conditions of Use of Digitised Theses from Trinity College Library Dublin

Copyright statement

All material supplied by Trinity College Library is protected by copyright (under the Copyright and Related Rights Act, 2000 as amended) and other relevant Intellectual Property Rights. By accessing and using a Digitised Thesis from Trinity College Library you acknowledge that all Intellectual Property Rights in any Works supplied are the sole and exclusive property of the copyright and/or other IPR holder. Specific copyright holders may not be explicitly identified. Use of materials from other sources within a thesis should not be construed as a claim over them.

A non-exclusive, non-transferable licence is hereby granted to those using or reproducing, in whole or in part, the material for valid purposes, providing the copyright owners are acknowledged using the normal conventions. Where specific permission to use material is required, this is identified and such permission must be sought from the copyright holder or agency cited.

Liability statement

By using a Digitised Thesis, I accept that Trinity College Dublin bears no legal responsibility for the accuracy, legality or comprehensiveness of materials contained within the thesis, and that Trinity College Dublin accepts no liability for indirect, consequential, or incidental, damages or losses arising from use of the thesis for whatever reason. Information located in a thesis may be subject to specific use constraints, details of which may not be explicitly described. It is the responsibility of potential and actual users to be aware of such constraints and to abide by them. By making use of material from a digitised thesis, you accept these copyright and disclaimer provisions. Where it is brought to the attention of Trinity College Library that there may be a breach of copyright or other restraint, it is the policy to withdraw or take down access to a thesis while the issue is being resolved.

Access Agreement

By using a Digitised Thesis from Trinity College Library you are bound by the following Terms & Conditions. Please read them carefully.

I have read and I understand the following statement: All material supplied via a Digitised Thesis from Trinity College Library is protected by copyright and other intellectual property rights, and duplication or sale of all or part of any of a thesis is not permitted, except that material may be duplicated by you for your research use or for educational purposes in electronic or print form providing the copyright owners are acknowledged using the normal conventions. You must obtain permission for any other use. Electronic or print copies may not be offered, whether for sale or otherwise to anyone. This copy has been supplied on the understanding that it is copyright material and that no quotation from the thesis may be published without proper acknowledgement.

Electro-Magnetic control of laser produced plasma

Clelia Pagano

A thesis presented for the degree of
Doctor of Philosophy

School of Physics
Trinity College Dublin
Ireland

February 2011

Declaration

This thesis has not been submitted as an exercise for a degree at this or any other university. The work described in this thesis is entirely my own,with exception of assistance recognised in the acknowledgments and the collaborative work noted in the publications. I agree that Trinity College may lend or copy this thesis on request.

[redacted]

Summary

This thesis describes the results of experiments to investigate the effects of magnetic and electric fields on the expansion dynamics of a low temperature laser produced plasma. The experiments were done in vacuum using different configurations of magnetic and electric fields, with the magnetic fields produced by permanent magnets.

For each configuration considered here, the effects of external magnetic and electric fields on the expansion dynamics, ion yield, electron temperature and deposition rate were studied. The results clearly show that the plasma changes its physical properties during expansion in the presence of an external field and these ultimately affect the emission characteristics and shape of the expanding plume. Several experimental techniques were used to demonstrate these effects and these included time-of-flight Langmuir ion probes, time-resolved optical imaging, time- and space-resolved optical emission spectroscopy and thin film depositions.

The experimental work presented here is divided into three main sections. In the first, plasma confinement was investigated using a magnetic field directed normal to the plasma expansion axis. In the second, plasma collimation was investigated using a magnetic field directed parallel to the plasma expansion axis. In the third part, plasma focusing was investigated using a combination of magnetic and electric fields. Two different setups were used in the third part: the first setup consisted of a converging magnetic field (parallel to the plasma flow) and an electric field (applied with an electrode); in the second setup a plasma lens was used as a novel deposition device.

Acknowledgements

I would like to thank all the people who contributed to the success of this work.

In particular my supervisor Prof. J. Lunney for giving me the opportunity to work in the group, for his valuable advice and constant support.

Thanks to Science Foundation Ireland for the funding.

Thanks to Prof. T. Ray for his advice about the MHD theory.

All past and current members of the group. Enrique and Tony for helping me get started in the lab. Isaac, Gearoid and Inam for their friendship and for many scientific and not so scientific discussions.

To all the staff members from the School of Physics for their constant support. A particular thank to Nigel and Chris for their help.

To my friends for the good time.

To my family and in particular my parents, even though far away I could always count on you, thanks for everything.

A special thank to Kevin, thank you for your constant support, encouragement and love.

Contents

Introduction

This work explores the use of magnetic and electric fields to control the expansion properties of a plasma produced by laser ablation (LPP). The laser ablation process is used in a wide range of applications in research and manufacturing such as laser machining in microelectronics, laser induced breakdown spectroscopy (LIBS) for material analysis and in pulsed laser deposition (PLD) of thin films.

In particular, pulsed laser deposition is an important method for the deposition of thin films for research and it is used to deposit a range of materials. Essentially the PLD technique involves focusing a high power laser beam on a target placed inside a vacuum chamber, producing a vapor during the laser pulse. This vapour is further heated by the laser to form plasma. The pressure gradient in this plasma layer drives the plasma to expand mainly in the direction normal to the target surface, i.e. the transverse component of velocity is much smaller than the forward component. By placing a substrate in the trajectory of the expanding plasma, material from the plasma can be deposited as a thin film.

The physical mechanisms involved in PLD including the ablation of the target, the expansion dynamics of the plasma and the growth of the film are quite complex. Within the physical mechanisms, the properties of the film produced are further affected by experimental parameters like target material, laser pulse characteristics and ambient conditions. Despite this physical complexity, PLD has become an increasingly popular technique for the deposition of a variety of materials in research. This is due mainly to its simplicity and unique ability to retain the stoichiometry of the target in the growing film. Recently PLD turned out to be a useful tool in the production of nanoparticle films [1, 2] and in the growth of carbon nanotubes [3]. The current interest in nanoparticles and nanostructured films is due to their novel optical, catalytic and electronic properties that differ significantly to that of bulk materials.

There are however some drawbacks associated with the PLD technique. The most significant is the contamination of the deposited film with micrometer size particles expelled in the ablation process. Such particles include liquid droplets and solid clusters. These particles are undesirable because they produce local defects in the film surface. Curved solenoidal magnetic fields have been widely used in both vacuum arc [4, 5, 6] and pulsed laser [7] deposition in order to address the particulate contamination problem. Permanent magnets have also been used to deflect the laser produced plasma [8, 9, 10, 11]. These filters use a curved magnetic field of moderate strength ($\sim 100\ mT$) to guide the plasma on a curved path between target and substrate. The undesirable particles are carried by their inertia in a straight trajectory to the filter wall leaving the substrate uncontaminated. Although particulate-free films were produced, these filters come with the cost of a significant loss in transmission efficiency, which means a decrease in the film growth rate. Contamination and deposition rate are both of fundamental importance in PLD. Of course it is desirable to have a simple means of complete macroparticle removal with plasma losses as low as possible. What is clear from the work done to date is that the various techniques proposed have not worked sufficiently well to find wide applications.

An additional issue arising in the deposition process is the forward peaked nature of the ablation plume. The plume expands assuming an ellipsoidal shape. Such a distribution leads to a non uniform deposition flux resulting in a non uniform thickness in the deposited film.

Since the film properties are significantly affected by the plasma characteristics, a better understanding of the formation and expansion of the laser produced plasma, as well as the exploration of new techniques to control them, is of great interest in PLD. This work then explores the use of magnetic and electric fields to achieve better control of the expansion properties of the plasma. Usually a LPP has a substantial ion fraction, it is then expected that the moving plasma will interact with external magnetic and electric fields. Several studies have demonstrated that a magnetic field can substantially modify the properties of the plasma. Plasma expansion both transverse [12, 13, 14] and parallel [15, 16] to the magnetic field has been investigated. In addition, both uniform [12, 13] and non-uniform

[14, 17] magnetic fields have been used. These studies have shown that when a LPP expands away from the ablation target in a magnetic field a wide range of effects can arise, such as change in the degree of plume excitation [12, 13], excitation of plasma instabilities [4, 14, 18] and plasma plume confinement [12, 16].

These effects are of interest not only for PLD, but for a wide range of applications. As an example, high magnetic field values ($\sim 20\ T$) have been used with high temperature LPPs [15, 16], where the aim was to magnetically confine a plasma column for soft X-ray laser development. Also, the increase in the excitation state of a LPP expanding across a magnetic field has been investigated with the aim of enhancing the sensitivity of the LIBS system [19]. The rotation induced in the plasma by a magnetic field ($E \times B$ drift) has been investigated in vacuum arc plasma centrifuges as a means to separate isotopes [20, 21]. A miniature magnetic cusp configuration has also been suggested for confinement of plasma produced by a femtosecond laser with a view to increasing the neutron yield [22]. For PLD application it is worth mentioning the work of Kobayashi et al. [17]. They demonstrated that placing a permanent magnet behind the substrate improves the high temperature PLD of superconductor materials. They also obtained room temperature epitaxy of NiO.

The aim of this work was then the modification of laser plasma expansion dynamics using magnetic and electric fields. Particular attention was dedicated to explore the possibility of collimating and focusing the plasma to increase the uniformity of the deposition flux and the deposition rate for PLD applications. The influence of magnetic and electric fields on the shape of plume expansion, spectral emission, ion yield and deposition rate of LPP was studied. Two approaches were mainly used: 1) magnetic field only and 2) combined magnetic and electric field.

This work is divided into 7 chapters. In Chapter 1 a general overview of the theoretical background is reported. The description of the equipment and the techniques used for data analysis is given in Chapter 2. Chapters 3 to 6 (inclusive) describe the results of the experiments obtained using different magnetic and electric field configurations. Finally, in Chapter 7 the main conclusions from previous chapters are summarized and new possibilities are discussed to continue this work.

Chapter 1

Theory

In this chapter a general overview of the theoretical background is reported. First, the main features of the nanosecond laser ablation process (including plasma formation and expansion in vacuum) are described. Then, the relevant fluid theory is given to describe the expansion of the plasma in magnetic and electric fields. The final part of this chapter describes the emission and absorption properties of the laser produced plasma. Calculations of these properties, obtained using a spectral synthesis code, are also detailed.

1.1 Laser ablation process

Laser ablation is the process of removing material from a solid or liquid surface by irradiating it with a laser beam. The laser ablation process is used in a wide range of applications in research and manufacturing such as laser machining in microelectronics, laser induced breakdown spectroscopy (LIBS) for material analysis and in pulsed laser deposition (PLD) of thin films. Despite the wide range of applications, the exact mechanisms of laser ablation are not yet fully understood. Several studies on laser absorption, material removal and its expansion can be found in the literature, but they cannot be considered exhaustive [23, 24, 25, 26]. To understand the exact mechanisms of this process is to understand the complex thermo-physical properties of the target and how they interact with the optical properties of the laser beam itself. This complexity makes a predictive analysis very challenging.

In this section the basic processes occurring during the irradiation of a metallic target with nanosecond laser pulses are described. Typical laser irradiances used in the nanosecond laser ablation and deposition experiments are $\geq 10^8\ W\ cm^{-2}$. These irradiances, which are also used in this work, are sufficient to create plasma. When the laser beam hits the target, electrons will absorb quanta of optical energy. The excited electrons thermalise rapidly by electron-electron collisions with a characteristic relaxation time τ_e. The energy from the electrons is then transferred to the lattice by electron-phonon interactions, characterised by a time $\tau_l > \tau_e$. For metals, the energy relaxation time, τ_e, is of the order of $10^{-13}\ s$, while τ_l is of the order of several picoseconds, both much smaller than the laser pulse duration τ_L ($\approx 10\ ns$) - $\tau_e << \tau_l << \tau_L$. For laser ablation with a nanosecond pulse, because of the small value of τ_e, the optical energy can be considered as being instantaneously turned into heat. Therefore the concept of temperature and heat conduction can be applied. Furthermore, since the temperature of the electron and ion subsystems equilibrate very early during the laser pulse, one temperature can be assumed for both subsystems, $T_e = T_i$.

During the laser pulse, the absorbed laser energy, first heats the target to the melting point and then to the boiling point. At this moment evaporation occurs from the liquid metal and vapor is formed on the target surface during the laser pulse. The vapor begins to absorb the laser pulse leading to heating of the vapor, ionisation and plasma formation. After the termination of the laser pulse there exists a thin ($\approx 10\ \mu m$) layer of hot (few eV) dense ($\approx 10^{18} - 10^{19}\ atoms/ions\ cm^{-3}$) plasma that expands due to internal pressure gradients, assuming a semi-ellipsoidal shape. The time required for laser absorption in the target, target heating, vaporization and plasma formation is much smaller than the time of expansion of the ablated material (which is of the order of a few μs). Therefore the laser ablation process can be schematically divided into two main phases, which are: plasma formation and plasma expansion.

1.1.1 Plasma formation

In the plasma formation phase there is a need to consider reflection and absorption of the laser beam by the target, thermal conduction, evaporation and absorption of the laser in the vapor. As discussed above, since $\tau_e << \tau_l << \tau_L$ many models are based on the standard heat conduction equation. During laser irradiation of a metal surface the laser pulse is absorbed in a thin layer of the target determined by the optical absorption coefficient, α:

$$d_{opt} = \alpha^{-1} = \left(\frac{4\pi k_{ext}}{\lambda}\right)^{-1} \tag{1.1}$$

where d_{opt} is the optical absorption depth, k_{ext} is the extinction coefficient of the target and λ is the incident laser wavelength. Typically, d_{opt} is of the order of $10\ nm$ [27]. As an example, for an incident laser wavelength of $248\ nm$, the extinction coefficient of copper is 1.8 [27], which gives $d_{opt} = 11\ nm$. Since this is much smaller than the typical laser beam diameters ($\approx 0.1 - 1\ mm$) the heat conduction equation can be solved in one dimension [28].

Another important parameter for the laser material interaction is the heat diffusion depth, d_{th}:

$$d_{th} = 2(D\tau_L)^{1/2} \tag{1.2}$$

where D is the thermal diffusivity of the metal and is:

$$D = \frac{k_c}{C\rho} \tag{1.3}$$

ρ is the target material density, k_c is the bulk thermal conductivity and C is the specific heat capacity. As an example, for solid copper $k_c = 380\ W\ m^{-1}\ K^{-1}$, $C = 420\ J\ kg^{-1}K^{-1}$ and $\rho = 8960\ kg\ m^{-3}$ [25], which, considering a laser pulse of $\tau_L = 20\ ns$, give $d_{th} \approx 4\ \mu m$. Since $d_{th} >> d_{opt}$ the laser absorption can be modeled as a surface heat source and the heat conduction equation is:

$$\rho C\frac{\partial T}{\partial t} = \frac{\partial T}{\partial z}\left(k_c\frac{\partial T}{\partial z}\right) + \alpha(1-R)I_0 exp(-\alpha z) \tag{1.4}$$

where I_0 is the incident laser irradiance, z is the distance into the target, T temperature and R the reflectivity of the target surface. Equation (1.4) is difficult to solve analytically because both the thermal and optical properties of the target material, expressed by the parameters ρ, k_c, C and R, are temperature dependent. A significant simplification is obtained by taking these parameters to be constant. Lunney et al. [24] used temperature averaged values. Then the surface temperature change of the target is described by:

$$T_S(t) = T_0 - \frac{L_F}{C} + \frac{1}{\sqrt{\pi k_c \rho C}} \int_0^t \frac{I_S(t-\tau)}{\sqrt{\tau}} d\tau \tag{1.5}$$

where L_F is the latent heat of fusion, T_0 is the initial target temperature and I_S is the irradiance reaching the target surface and it is given by:

$$I_S = (1 - R_L) I_L exp\left(-\frac{\sigma N l}{cos\theta}\right) + I_p(1 - R_p) - \left(\frac{d(Nl)}{dt}\right) L_V \tag{1.6}$$

where I_L and I_p are respectively the laser and plasma irradiance, θ is the angle of incidence of the laser, R_L and R_p are respectively the target reflectivities with respect to the laser and plasma emission, L_V is the latent heat of vaporisation, N is the average ion/atom density in the vapor, l is the vapor layer thickness and σ is the total absorption cross section of the vapor. The product $Nl\sigma$ is the optical opacity of the layer of plasma. The first term in equation (1.6) accounts for the absorption of the incident laser irradiance, I_L, by the evaporated particles, the second term accounts for the irradiance due to the plasma self emission and the last term accounts for the heat of vaporisation loss by the target material.

The evaporation rate at the target surface depends on the surface temperature, T_S, and on the vapor pressure, P_V, and it can be described by the Hertz-Knudsen equation [24]:

$$\frac{d(Nl)}{dt} = \frac{P_V(T_S)}{\sqrt{2\pi M k_B T_S}} \tag{1.7}$$

where M is the mass of the target atoms. The vapor pressure is commonly expressed in the form of the Clausius-Clapeyron equation:

$$P_V(T_S) = P_0 \, exp\left[\frac{L_V}{k_B}\left(\frac{1}{T_0} - \frac{1}{T_S}\right)\right] \tag{1.8}$$

where P_0 is the equilibrium vapor pressure at temperature T_0, which is usually taken as the boiling temperature.

The absorption of the laser in the vapor reduces the laser irradiance reaching the target; as a result, the ablation rate is reduced. It also causes heating and ionisation in the vapor to form plasma. Assuming the plasma to be in local thermodynamic equilibrium, the degree of ionization can be estimated with the following Saha equation [26]:

$$\frac{n_e n_{z+1}}{n_z} = 2\left(\frac{2\pi m_e k_B T}{h^2}\right)^{3/2} exp\left(-\frac{E_z}{k_B T}\right) \tag{1.9}$$

where n_e is the electron number density, n_z and n_{z+1} refers to the number densities in the *zth* and *(z+1)th* ion stages, respectively, h is the Planck constant and E_z is the ionisation energy of the *zth* ionisation stage.

In the ionized vapor a significant number of free electrons will be present, thus inverse Bremsstrahlung (IB) will be one of the absorption mechanisms active in the plasma. IB involves the absorption of photons by free electrons, through collisions with neutral and ionized atoms. Passing through the electric field of an atom or ion, an electron can absorb a photon and gain kinetic energy. This will further promote ionization and excitation through electron collisions with excited- and ground-state atoms and ions. Due to the difference in field strength for the ions compared to neutral atoms, IB absorption due to ions dominates over that from neutral species [29]. The electron-ion IB absorption cross section is:

$$\sigma_{IB,ion} = 1.27 \times 10^{-46}\frac{Z^2\lambda^3 n_i}{\sqrt{T}}\left[1 - exp\left(-\frac{h\nu}{T}\right)\right]\ cm^2 \tag{1.10}$$

where λ is the laser wavelength in *nm*, $h\nu$ is the laser photon energy in *eV*, T is the electron and ion temperature in *eV*, Z is the ionic charge and n_i is the ion number density in cm^{-3}. For $T = 3\ eV$, $n_i = 5 \times 10^{18}\ cm^{-3}$, $Z = 2$ [24], which are typical values for the plasma layer existing during the laser pulse, and for $\lambda = 248\ nm$, $\sigma_{IB,ion}$ is estimated to be about $1.8 \times 10^{-20}\ cm^2$. The absorption coefficient is then $\alpha_{IB,ion} = n_e\sigma_{IB,ion} = 0.18\ cm^{-1}$. Lunney et al. [24] pointed out that the absorption due to IB is too small to account for the plasma formation, hence other absorption mechanisms should be considered.

Another absorption mechanism in the plasma is photoionization (PI). When a bound electron absorbs a photon with energy higher than the ionization energy, the electron is freed and any excess of energy is converted to the electron kinetic energy. In this case to accurately calculate the total absorption, information on energy levels and relative populations of each plasma species need to be known, resulting in a complicated problem. Lunney et al. [24] gave an approximate estimate of the ionization cross section by using a hydrogen-like photoionization cross section and by assigning a single absorption cross section to both atoms and ions. With these approximations the cross section for photoionization is given by [24, 29]:

$$\sigma_{PI} = 7.9 \times 10^{-18} \left(\frac{E_I}{h\nu}\right)^3 \sqrt{\left(\frac{I_H}{E_I}\right)} \ cm^2 \tag{1.11}$$

where I_H is the ionization potential of hydrogen, E_I is the ionization energy of the excited states that can be photoionised. Taking E_I to be equal to the photon energy of a 248 nm excimer laser ($= 5\ eV$), σ_{PI} is about $1.3 \times 10^{-17}\ cm^2$ ($\alpha_{PI} \approx 130\ cm^{-1}$), which is three orders of magnitude bigger than $\sigma_{IB,ion}$. We will return on this point in Section 1.3.4, where a more accurate calculation of the absorption coefficients will be presented.

The absorbed energy determines density and temperature of the plasma. Density and temperature gradients will in turn determine the expansion dynamics of the plasma; they drive the rapid expansion of the plasma away from the target surface, tending to lower the density and the temperature.

1.1.2 Plasma expansion

The expansion dynamics of the ablation plume is very important in PLD because they have a direct effect on the characteristics of the thin film produced. For expansion in vacuum, several models can be found in literature, the most widely used are the models developed by Anisimov et al. [30, 31] and the one by Singh et al. [32]. The Anisimov model considers the expansion of the plume to be isentropic, while Singh consider an isothermal expansion. Lunney et al. [33] have shown that both models can be used to describe the plasma expansion and that the isentropic model is the more appropriate when the plume temperature is less than 12 eV. Since the typical plasma temperature measured during laser ablation is of the order of 1-3 eV, the Anisimov model is the more appropriate one in our experimental condition and is discussed herein.

This model describes the three-dimensional adiabatic expansion of a plasma in a vacuum after the termination of the laser pulse (which is taken as time zero). The model is based on three main assumptions: that the plasma can be considered a perfect gas, that its expansion is isentropic and self-similar. The first assumption justifies the use of the gas dynamics equations to describe the expansion of the overall plasma. Although the model was developed for the expansion of a neutral gas cloud, it has proven to accurately describe the expansion of ionized plasma produced by nanosecond laser ablation in a vacuum [34, 35]. In particular, Hansen et al. [34] compared experimental studies of the laser ablation plume dynamics with the theoretical solution of the Anisimov model. The authors found a good correspondence between the experiment and the model for the measured angular and temporal distribution of the ion flux and the electron temperature. The second assumption means that the thermal diffusion is slow compared with the expansion rate and so the heat exchanged during the plasma expansion can be neglected. Finally, the self-similar assumption means that the characteristics of the expanding plasma remain constant on ellipsoidal surfaces. The shape of the plasma distribution is determined by the dimensions and energy of the laser spot incident on the target. At the end of the laser pulse, as there is no further addition of energy or mass to the plasma, its expansion can be considered adiabatic; so after an initial acceleration, the plasma velocity remains fairly constant and the motion is said to be self-similar.

The gas dynamic equations which govern the expansion are given by:

$$\frac{\partial \rho}{\partial t} + \nabla \cdot (\rho\, \mathbf{v}) = 0 \tag{1.12}$$

$$\frac{\partial \mathbf{v}}{\partial t} + (\mathbf{v} \cdot \nabla)\mathbf{v} + \frac{1}{\rho}\nabla p = 0 \tag{1.13}$$

$$\frac{\partial S}{\partial t} + (\mathbf{v} \cdot \nabla)S = 0 \tag{1.14}$$

where ρ is the plume density, $\mathbf{v}$ the velocity, p the pressure and S the entropy.

At time zero, which is at the end of the laser pulse, the initial plume is considered to be semi-ellipsoidal in shape with principal radii X_0, Y_0 and Z_0. X_0 and Y_0 are the dimensions in the plane of the target and are taken as that of the major and minor radii of the ablation spot, respectively. Z_0 is the thickness of the ablated material and is approximated as $Z_0 \approx c_s \tau_L$, where c_s is the sound velocity and τ_L is the laser pulse duration. As the expansion proceeds the radii of the ellipsoidal plume front in the x, y and z directions are *X(t)*, *Y(t)* and *Z(t)*.

The isentropic solution of the gas dynamic equations (1.12)-(1.14) gives the following expressions for density, pressure and entropy profiles:

$$\rho(x,y,z,t) = \frac{M}{I_1(\gamma)XYZ}\left[1-\left(\frac{x}{X}\right)^2-\left(\frac{y}{Y}\right)^2-\left(\frac{z}{Z}\right)^2\right]^{\frac{1}{(\gamma-1)}} \tag{1.15}$$

$$p(x,y,z,t) = \frac{E}{I_2(\gamma)XYZ}\left[\frac{X_0Y_0Z_0}{XYZ}\right]^{(\gamma-1)} \times \left[1-\left(\frac{x}{X}\right)^2-\left(\frac{y}{Y}\right)^2-\left(\frac{z}{Z}\right)^2\right]^{\frac{\gamma}{(\gamma-1)}} \tag{1.16}$$

$$\begin{aligned} S(x,y,z,t) = \frac{1}{\gamma-1} ln \Bigg\{ & \frac{E}{I_2(\gamma)X_0Y_0Z_0}\left[\frac{I_1(\gamma)X_0Y_0Z_0}{M}\right]^{\gamma} \\ & \times \left[1-\left(\frac{x}{X}\right)^2-\left(\frac{y}{Y}\right)^2-\left(\frac{z}{Z}\right)^2\right]^{\frac{\gamma-2}{\gamma-1}} (\gamma-1) \Bigg\} + const. \end{aligned} \tag{1.17}$$

where M is the mass and E is the initial energy of the plasma, $I_{1/2}$ are functions of γ [30, 31] and γ is the ratio of specific heats at constant pressure, C_p and constant volume C_v. Since the plasma is considered an ideal gas, γ is assumed constant. Using the above expressions (1.15)-(1.17), the gas dynamic equations (1.12)-(1.14) can be reduced to the following ordinary differential equations:

$$X\frac{\partial^2 X}{\partial t^2} = Y\frac{\partial^2 Y}{\partial t^2} = Z\frac{\partial^2 Z}{\partial t^2} = (5\gamma-3)\frac{E}{M}\left[\frac{X_0Y_0Z_0}{XYZ}\right]^{(\gamma-1)} \tag{1.18}$$

The initial conditions are set as:

$$X(0) = X_0; \quad Y(0) = Y_0; \quad Z(0) = Z_0; \quad \frac{\partial X}{\partial t} = \frac{\partial Y}{\partial t} = \frac{\partial Z}{\partial t} = 0 \tag{1.19}$$

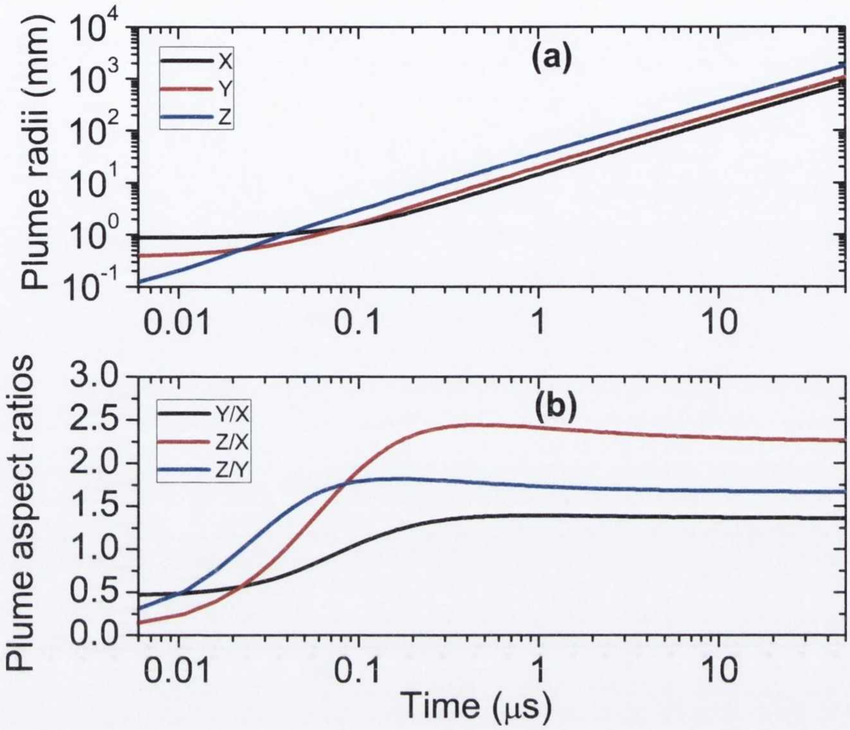

Figure 1.1: Evolution of the (a) plume radii and (b) plume aspect ratios as a function of time.

Numerical solution of the equations (1.18) yields the temporal variation of the radii of the plume front, and therefore the plume shape. The plume elongation can be described by the aspect ratio k, i.e. $k_{zx} = Z/X$, $k_{zy} = Z/Y$ and $k_{yx} = Y/X$. The values of k_{zx} and k_{zy} determine the angular spread of the particle flux. The angular distribution, $F(\theta)$, the current density distribution, j, in the y-z plane and the temperature, T, of the plume calculated from the solution of the gas dynamic equations are respectively:

$$F(\theta) = F(0)(1 + k_{zy}^2 tan^2\theta)^{-3/2} \tag{1.20}$$

$$j(y, z, t) = \frac{N}{I_1}(XYZ)^{-1}\left[1 - \left(\frac{y}{Y}\right)^2 - \left(\frac{z}{Z}\right)^2\right]^{\frac{1}{(\gamma-1)}} \times (v_y^2 + v_z^2)^{1/2} \tag{1.21}$$

$$k_B T = E\frac{m}{M}(\gamma - 1)(2\gamma)^{-1}\left(\frac{X_0 Y_0 Z_0}{XYZ}\right)^{\gamma-1} \times \left[1 - \left(\frac{y}{Y}\right)^2 - \left(\frac{z}{Z}\right)^2\right] \tag{1.22}$$

where N is the total number of particles in the plume, k_B is the Boltzmann constant and m is the atomic weight.

Fig. 1.1(a) shows the evolution of the radii of the plasma plume and (b) shows the plume aspect ratios, k_{zx}, k_{zy} and k_{yx}, as a function of time. This graphs have been calculated for a copper plasma by choosing the following starting parameters: $X_0 = 870\ \mu m$, $Y_0 = 400\ \mu m$, $Z_0 = 67\ \mu m$, $\gamma = 1.25$ and $E_p = 52\ eV$, where E_p is the average energy per plasma particle.As mentioned above, after the laser pulse, the plasma expands and accelerates in all the directions due to pressure gradients. When the gradients go to zero the plume expansion becomes inertial. Fig. 1.1(a) shows that the acceleration phase lasts until 100 ns. The figure also shows that, as expected, the expansion velocity is greatest in the z direction. This can be explained by considering the lateral dimensions, X_0 and Y_0, of the plume at the beginning of the expansion. At this time, X_0 and Y_0 are much larger than the thickness, Z_0, implying that the pressure gradient in the z direction is higher than those in the x and y directions. As a result, the plasma will expand mainly in the forward direction assuming the typical semi-ellipsoidal shape.

The so called "flip-over" effect can also be explained in terms of the initial pressure gradients. The flip-over effect occurs when the laser spot has radii Y_0 smaller than X_0. In this case the pressure gradient is stronger in the y direction, causing the plasma to expand faster in this direction. Therefore the aspect ratio k_{yx} is initially less than 1, but changes to a value greater than 1 at late time in the inertial phase. In the example of Fig. 1.1(b) the flip-over is observed at about 90 ns.

1.2 Fluid theory

The dynamic properties of a laser produced plasma change significantly when the expansion occurs in a magnetic and/or electric field. The self-similar expansion assumption is no longer valid and other factors must be considered. As schematically represented in Fig. 1.2, when a plasma expands in the presence of a magnetic field the charged particles in the plasma will feel the Lorentz force. In particular, the plasma electrons will follow the magnetic field lines gyrating around them in helical trajectories. As will be shown below (see Fig. 1.4), the electron Larmor

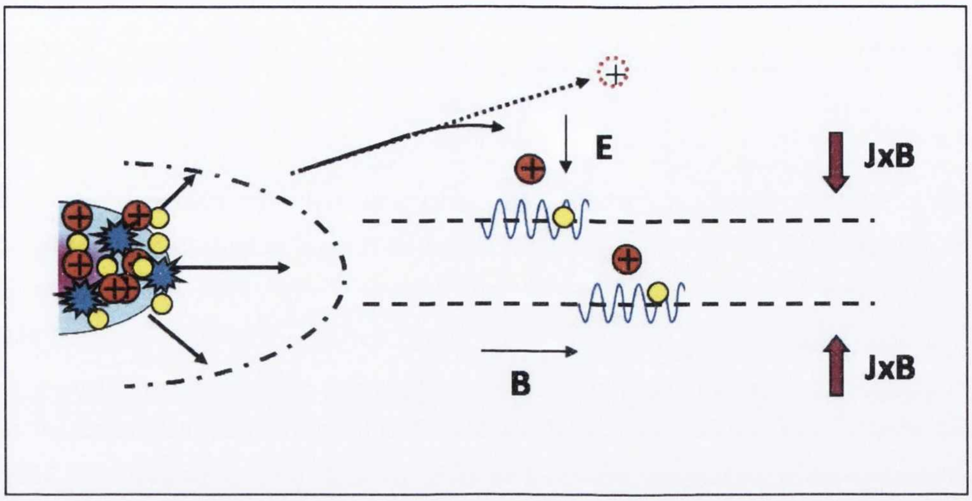

Figure 1.2: Schematic representing some of the effects of an external magnetic field, **B**, on the plasma expansion. The yellow and red circles represent the electrons and the positive ions in the plasma, respectively. The semi-ellipse represents the semi-ellipsoidal profile of the plume expanding in the region without magnetic field. **E** is the space charge electric field.

radius, r_{Le}, is small compared to the plasma dimension and the electrons are said to be "magnetized". The plasma ions also gyrate around the magnetic field lines, but with much bigger Larmor radius with respect to the electrons, because of the much bigger mass. Eventually the electrostatic force, due to the charge separation between the electrons and ions, intervenes to balance the inertia force and the pressure gradient force. As it will be shown belove (Fig. 1.4), the Debye length, $\lambda_{D,e}$, is found to be very small of the order of 10^{-5} cm. The small value of $\lambda_{D,e}$ implies that the electrostatic force binds the ions to the electrons, preventing them from moving in a straight direction driven by their inertia. Hence the plasma polarization acts on the plasma ions so that they also tend to follow the magnetic field lines. At this point the self-consistent electric field, **E**, causes the **E**x**B** drift motion which causes the plasma to rotate and it also gives rise to a diamagnetic current, **J**. This current interacts with the external magnetic field through the **J**x**B** force. This force acts to decelerate the motion of the plume across the magnetic field. Fig. 1.2 schematically represents these effects in the case of a plasma expanding along a magnetic field, but similar considerations can be applied for others relative orientations of the magnetic field and the plasma flow.

To build a model that describes the interaction of magnetic and electric fields with the plasma flow is not an easy task. A plasma is a system containing a very large number of mobile charged particles. Each charged particle creates its own microscopic electric and magnetic fields and reacts to the microscopic fields of all other particles. The actual electric and magnetic fields are the sum of all the microscopic contributions of the particles. Hence a plasma model must be able to describe both the dynamics of the plasma in the electromagnetic fields and the generation of those fields by the plasma. The most detailed and complete description of the plasma behavior is provided by the Kinetic theory [36]. This theory describes the evolution of the plasma through a density distribution function in phase space. It contains information about both the microscopic orbits of individual charged particles and the macroscopic behavior of the plasma as a whole. However, the extreme complexity of this model has led to the development of simpler mathematical models with a narrower range of applicability, using a fluid approach. In these models only the motion of a fluid element is taken into account and hence the information related to the distribution of velocities of the particles within a fluid element is lost. The models describe macroscopic quantities like temperature, pressure and density and how they change in space and time. Some of the fluid models that have been developed include the multi-fluid model, two-fluid model, ideal and resistive single-fluid models. The two-fluid and the resistive single-fluid models will be considered herein.

The multi-fluid theory considers the plasma as being composed of different particle species and assumes that each species behaves as a separate fluid. It captures the differences in the fluid behaviour of the light electrons and the heavy ions. The two-fluid theory is a special case of the multi-fluid for a fully ionized plasma consisting of electrons and one type of ions. In this case the complete set of fluid equations is [37]:

$$\frac{\partial n_j}{\partial t} + \nabla \cdot (n_j \mathbf{v}_j) = 0 \tag{1.23}$$

$$m_j n_j \left[\frac{\partial \mathbf{v}_j}{\partial t} + (\mathbf{v}_j \cdot \nabla) \mathbf{v}_j \right] = q_j n_j (\mathbf{E} + \mathbf{v}_j \times \mathbf{B}) - \nabla p_j + \frac{q_j n_j \mathbf{j}}{\sigma} \tag{1.24}$$

$$p_j = C_j n_j^{\gamma_j} \tag{1.25}$$

where the index j is i for ions and e for electrons, $\mathbf{v}$ is the average velocity, n is the number density, q_e and q_i are, respectively, the electric charge of electrons *(q_e=-e)* and ions *(q_i=Ze)*, $\mathbf{j}$ is the current density, σ is the electrical conductivity, p is the pressure, C is a constant and γ is the adiabatic constant, $\gamma = C_p/C_v$. The above equations are, respectively, the conservation of mass, the conservation of momentum and the equation of state, which assumes an adiabatic plasma expansion. To close the system of equations, Maxwell's equations are required:

$$\nabla \times \mathbf{E} = -\frac{\partial \mathbf{B}}{\partial t} \tag{1.26}$$

$$\nabla \times \mathbf{B} = \epsilon_0 \mu_0 \frac{\partial \mathbf{E}}{\partial t} + \mu_0 \mathbf{j} \tag{1.27}$$

where the current density is given by:

$$\mathbf{j} = n_i q_i \mathbf{v}_i + n_e q_e \mathbf{v}_e \tag{1.28}$$

The equation for conservation of momentum relates the fluid velocity to electromagnetic force and pressure gradient. The electromagnetic force couples the equation of conservation of momentum to the Maxwell equations. It should also be noted that the electromagnetic force acts on plasma fluid elements and not on individual particles - it couples all the charged plasma components together. The reason for this is that the electric and magnetic fields in the electromagnetic force act on all charged components and, at the same time, all charged components contribute to the electric and magnetic fields.

In the single fluid theory, also called Magnetohydrodynamic (MHD) theory, the various individual species are not specified. In this case macroscopic variables are defined for the plasma as a whole by adding the contributions of the various species in the plasma. In this way, information about high frequency and small scale dynamics are lost and only the low frequency and large scale fluid dynamics are described. MHD theory can be applied to plasma situations where the spatial and temporal scales of the variations of the fluids and fields are substantially longer than the corresponding scales of the heaviest component of the plasma, i.e.

the ions. The equations of resistive MHD are written below [38]:

$$\frac{d\rho}{dt} + \rho\nabla \cdot \mathbf{v} = 0 \tag{1.29}$$

$$\rho\frac{d\mathbf{v}}{dt} = \mathbf{j} \times \mathbf{B} - \nabla p \tag{1.30}$$

$$\frac{dp}{dt} = -\gamma p\nabla \cdot \mathbf{v} + (\gamma - 1)\frac{\mathbf{j}^2}{\sigma} \tag{1.31}$$

$$\frac{\partial \mathbf{B}}{\partial t} = \frac{\nabla^2 \mathbf{B}}{\sigma\mu_0} + \nabla \times (\mathbf{v} \times \mathbf{B}) \tag{1.32}$$

$$T = \frac{p}{R_0\rho} \tag{1.33}$$

$$\mathbf{j} = \frac{\nabla \times \mathbf{B}}{\mu_0} \tag{1.34}$$

where ρ is the mass density of the fluid, R_0 is the gas constant and the electric field is given by the modified Ohm's law:

$$\mathbf{E} = \frac{\nabla \times \mathbf{B}}{\sigma\mu_0} - \mathbf{v} \times \mathbf{B} \tag{1.35}$$

The modified Ohm's law links **E** and **B** to **v** and it contains the change of momentum due to collisions. To go from a multi-fluid to a single fluid model of plasma more rigid approximations are introduced, limiting the applicability of the MHD model. The main approximations made in the derivation of the equations (1.29)-(1.35) are the following:

(i) Frequent collisions: $\tau_i << \left(\frac{m_e}{m_i}\right)^{1/2} \tau_H$

(ii) Frequent collisions: $\lambda_c << L_H$

(iii) Quasi-neutrality: $Zn_e \approx n_i$

(iv) Non relativistic: $v << c$

(v) Scalar conductivity: $\omega_e << \nu_c$

(vi) Small Larmor radius: $r_{L_i} << L_H$

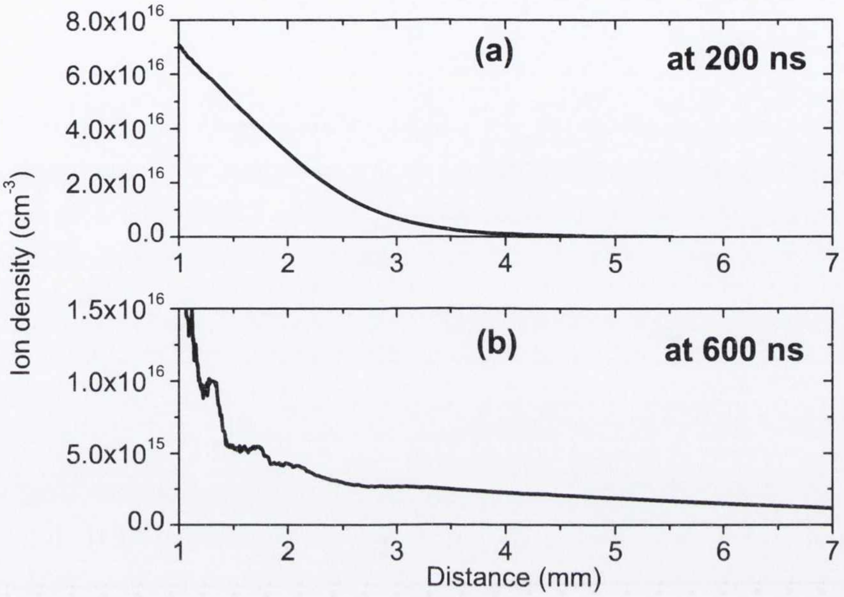

Figure 1.3: Density profile of copper plasma (a) 200 *ns* and (b) 600 *ns* after the laser pulse.

where τ_H and L_H are, respectively, the minimum hydrodynamic time and length scales of interest, τ_i is the ion collision time, λ_c is the mean free paths of ions, ω_e is the electron Larmor frequency and ν_c is the electron collision frequency. Hence to use the single fluid model described above, the valdity of the assumptions (i) - (v) must first be justified. In the situations where the assumptions are not valid, the two-fluid model should be used instead. To understand if and when the MHD model can be applied to our experimental plasma, several plasma parameters were calculated. They are discussed in the following paragraph.

1.2.1 Validity of MHD

In order to justify the use of the MHD model, a number of plasma parameters have been calculated. These include the Larmor radii and frequencies and the mean free paths - among others. All calculations have been done considering a copper plasma with a typical temperature, T, of about 1 eV and charge state

$Z = 1$.

First of all the hydrodynamic length, L_H, and time, τ_H, scales of interest must be defined for our experimental conditions. Here L_H and τ_H are taken as the distance and the time interval for which the plasma density changes by a factor of 2. It should also be noted that the rate of changes of the plasma parameters will be different at different points in time and space. As an example, Fig. 1.3 shows the density profile of a copper plasma 200 ns and 600 ns after the laser pulse. It can be seen that the distance over which the density changes by a factor of 2 is about 0.6 mm at 200 ns and about 2.5 mm at 600 ns. Similarly, the time over which the density changes by a factor of 2 is about 100 ns at 2 mm from the target and about 400 ns at 10 mm from the target. To justify the use of the MHD model we consider the worst case scenario - that is - the smallest values for τ_H and L_H.

An important assumption in magnetohydrodynamics is that the fluid passes through a series of quasi-static equilibrium states. To establish quasi-static equilibrium, changes in the macroscopic variables must take place on a time scale that is long when compared with the relaxation time for the attainment of local equilibrium. This requires frequent collisions. Moreover the one-fluid model assumes one temperature, $T_i = T_e$. Hence the time, τ_{eq}, required for initially different temperatures to become equal must be smaller than τ_H. This imposes the strong collisionality condition (i) to obtain a local equilibrium state. An estimate of τ_{eq} is given by [39]:

$$\tau_{eq} \approx \left(\frac{m_i}{m_e}\right)^{1/2} \tau_{i,i} = 2 \times 10^5 Z^{-4} \left(\frac{m_i}{m_e}\right) \frac{T^{3/2}}{n\ ln\Lambda} \quad s \tag{1.36}$$

where τ_{ii} is the ion-ion collision time in s, n is the number density in cm^{-3}, T is the temperature in eV and $ln\Lambda$ is the Coulomb logarithm:

$$ln\Lambda = ln\left(12\pi n \lambda_{D,e}^3\right) \tag{1.37}$$

with the Debye length, $\lambda_{D,e}$, given by:

$$\lambda_{D,e} \approx \left(\frac{\epsilon_0 k_B T}{e^2 n}\right)^{1/2} \tag{1.38}$$

Fig. 1.4(a) shows τ_{eq} as function of the density n calculated using equation (1.36). It can be seen that the condition (i) is satisfied for densities $> 5 \times 10^{16} cm^{-3}$. For lower plasma densities τ_{eq} is comparable with the hydrodynamic time scale.

Fig. 1.4(b), shows the Debye length as function of the density. It can be seen that the Debye length is found to be much smaller than L_H. Hence the quasi-neutrality condition is well satisfied.

In terms of scale lengths the MHD theory requires that the mean free paths of ions and electrons is small compared with L_H, which is condition (ii). Because the mean free path, λ_c, is the product of the thermal velocity and the collision time, it has the same order of magnitude for ions and electrons. An estimate of λ_c can be then calculated from the following equation for the electron-ion mean free path [39] and its plot as a function of density is shown in Fig. 1.4(c):

$$\lambda_{ei} \approx 3.4 \times 10^{13} \frac{T^2}{n \, ln\Lambda} \; cm \tag{1.39}$$

with n in cm^{-3} and T in eV. From Fig. 1.4(c), it can be seen that λ_{ei} is very small for the range of density of interest, so the (ii) is satisfied.

Condition (iv) expresses the assumption of MHD that claims that the fields change on the same scales as the plasma flow. The flow is dominated by the ion inertia and so the plasma flow is non-relativistic. On the basis of this assumption the electrostatic force, $q\mathbf{E}$, and the displacement current, $\epsilon_0 \partial \mathbf{E}/\partial t$ could be neglected in the MHD equations. This is an important difference between MHD and the two-fluid model where wave and electron speeds may be relativistic and so the electrostatic force and the displacement current could not be neglected.

To verify the condition (v), the electron Larmor frequency, ω_e, should be small compared with the electron-ion collision frequency, ν_{ei}. An estimate of those parameters can be calculated using the following equations [39]:

$$\nu_{ei} = 2 \times 10^{-6} \, \frac{Z \, n \, ln\Lambda}{T^{3/2}} \; s^{-1} \tag{1.40}$$

$$\omega_e = \frac{e \, B}{m_e} \tag{1.41}$$

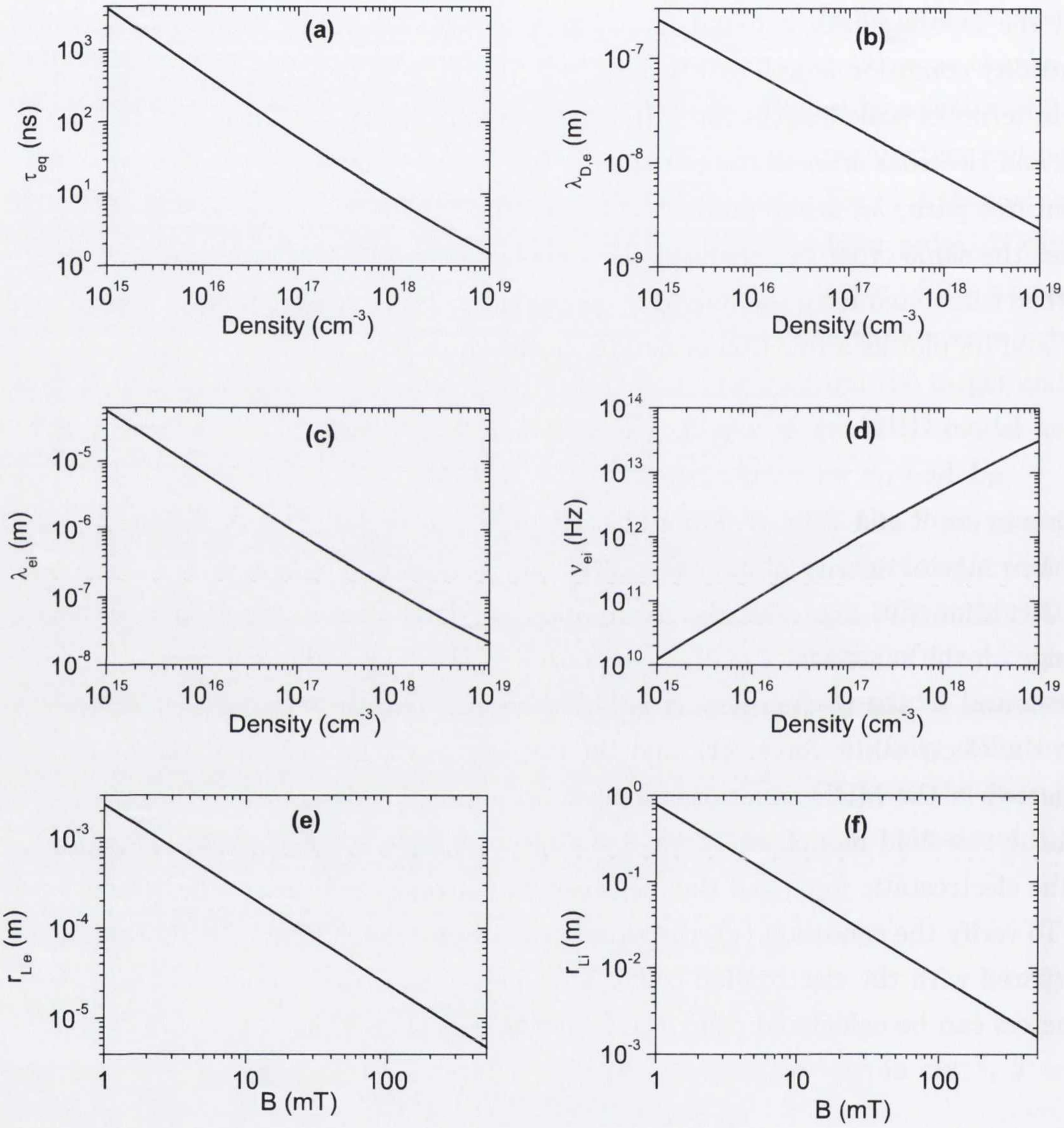

Figure 1.4: (a) τ_{eq} as a function of the density n calculated using equation (1.36); (b) Debye length as a function of the density calculated from equation (1.38); (c) λ_{ei} as a function of the density calculated using equation (1.39); (d) electron-ion collision frequency calculated from equation (1.40); (e) electron, r_{Le}, and (f) ion, r_{Li}, Larmor radius as a function of the magnetic field strength. These plasma parameters have been calculated considering a copper plasma with a typical temperature, T, of about 1 eV and ion charge state $Z = 1$.

The approximation (v) of scalar conductivity has been used to derive equation (1.35). This equation does not have a rigorous derivation, but is an approximation of the Generalized Ohm's law, given by:

$$\mathbf{j} + \frac{\omega_e}{\nu_c}(\mathbf{j} \times \mathbf{b}) = \sigma \left(\mathbf{E} + \mathbf{v} \times \mathbf{B} + \frac{m_i}{Ze\rho} \nabla p_e \right) = \sigma \tilde{\mathbf{E}} \tag{1.42}$$

where $\mathbf{b}$ is a unit vector parallel to $\mathbf{B}$ and the $\mathbf{j} \times \mathbf{B}$ term is called the Hall current. The derivation of (1.42) requires the two-fluid approach. This is because a current exists only if the ions and electrons have distinct flow velocities and this means that in the plasma there are two fluids rather than one. The presence of the Hall current in equation (1.42) implies that there must be a component of $\tilde{\mathbf{E}}$ that is perpendicular to both $\mathbf{j}$ and $\mathbf{B}$ to balance the $\mathbf{j} \times \mathbf{B}$ term; hence there is no scalar relationship between $\mathbf{j}$ and $\tilde{\mathbf{E}}$ unless condition (v) is valid. Figure 1.4(d) shows the electron-ion collision frequency as a function of density. Comparing ν_{ei} with the values of ω_e reported in Table 1.1, it can be seen that, for field strength of 320 mT, the condition (v) is satisfied for densities $\geq 2 \times 10^{16}\ cm^{-3}$.

Furthermore, to obtain equation (1.35) also the pressure gradient term in equation (1.42) was neglected. This can be done if the ions are "magnetized" - condition (vi). The MHD model, in fact, requires that the particles in the plasma are magnetized, i.e. that their Larmor radii are much smaller than the length scale, L_H, of the system. The Larmor radii for electrons, r_{Le}, and ions, r_{Li}, are given by:

$$r_{Le/i} = \frac{\sqrt{m_{e/i} k_B T}}{eB} \tag{1.43}$$

The light electrons are always more closely tied to the magnetic field lines than the heavy ions. In Fig. 1.4(e) and (f), the electron and ion Larmor radii are shown as a function of the magnetic field strength. It can be seen that moderate magnetic fields (in the order of 10 mT), are sufficient to magnetize the plasma electrons. However, because of their bigger mass, magnetization of the ions requires a much stronger magnetic field than that needed for the magnetization of the electrons. For the same range of magnetic field strengths the ion Larmor radius is about three orders of magnitude bigger than r_{Le}. As an example, in Table 1.1 the values of r_{Le} and r_{Li} corresponding to two different magnetic field strengths are shown.

B (mT)	r_{Le} (m)	r_{Li} (m)	ω_e (Hz)
20	1.2×10^{-4}	4×10^{-2}	3.5×10^{9}
320	7.5×10^{-6}	2.5×10^{-3}	5.6×10^{10}

Table 1.1: Plasma parameters

n (cm^{-3})	τ_{eq} (s)	λ_{ei} (m)	ν_{ei} (Hz)
10^{17}	59×10^{-9}	8.7×10^{-7}	7.7×10^{11}
6×10^{15}	7.3×10^{-7}	1.07×10^{-5}	6.3×10^{10}

Table 1.2: Plasma parameters

In this work magnetic field strengths of about 320 mT have been used. Hence in our experimental conditions, the ions are not magnetized, because the ion Larmor radius is $\geq L_H$ and so condition (vi) is not fulfilled.

In conclusion, from the discussion above, it follows that for a fully ionized copper plasma with a temperature of about 1 eV, conditions (i) - (v), with the exception of (vi), are simultaneously satisfied for magnetic field $\geq$ 300 mT and density $> 5 \times 10^{16}$ cm^{-3}. The ion Larmor radius is found to be of the same order of magnitude of L_H. It seems that the conditions of our experimental plasma fall along the edge of the applicability of the MHD model. Hence, although condition (vi) requires the $r_{L_i} << L_H$, in this work an attempt will be made to use the MHD model for a qualitative description of the plasma dynamics in the presence of a magnetic field.

1.2.2 Pressure balance

Within an MHD description of the plasma behavior, an important parameter for the characterization of the flow of a laser produced plasma through an applied magnetic field is the plasma beta, β. β is defined as the ratio of the plasma pressure, P_p, to the magnetic pressure P_m:

$$\beta = \frac{P_p}{P_m} = \frac{(nm_i v_i^2) + (nk_B T)}{(B_{ext}^2/2\mu_0)} \tag{1.44}$$

where B_{ext} is an external magnetic field. The meaning of this parameter can be clarified by considering the radial equilibrium of a cylindrical plasma. Assuming cylindrical symmetry and $B = B\hat{z}$, the equations (1.30) and (1.34) give:

$$\frac{d}{dr}\left[P_p + \frac{B_z^2}{2\mu_0}\right] = 0 \tag{1.45}$$

$$\mu_0 \mathbf{j} = -\frac{dB_z}{dr}\,\hat{\phi} \tag{1.46}$$

Integrating the above equations:

$$P_p + \frac{B^2}{2\mu_0} = \frac{B_{ext}^2}{2\mu_0} \tag{1.47}$$

where $\hat{\phi}$ is the azimuthal coordinate and B is the induced magnetic field in the plasma column. Thus β is:

$$\beta = \frac{P_p}{B_{ext}^2/2\mu_0} = 1 - \left(\frac{B}{B_{ext}}\right)^2 \tag{1.48}$$

and its value will be in the range $0 < \beta < 1$. The equation (1.47) shows that the plasma behaves like a diamagnetic medium. When plasma expands in a magnetic field, a diamagnetic current arises to exclude the field from its interior. This current interacts with the external magnetic field through the $\mathbf{j} \times \mathbf{B}$ force. This force pushes the plasma towards the axis stopping the plasma expansion across the magnetic field. Hence β is a measure of the degree to which the magnetic field is holding the plasma in equilibrium.

In plasmas with $\beta \leq 1$ the magnetic field dominates plume dynamics. In this case the plasma should decelerate rapidly as it expands across the magnetic field. Ripin et al. [40] gave an estimate of the plume deceleration, g, based upon a spherical expansion of a plasma in a magnetic field in terms of the mass of the

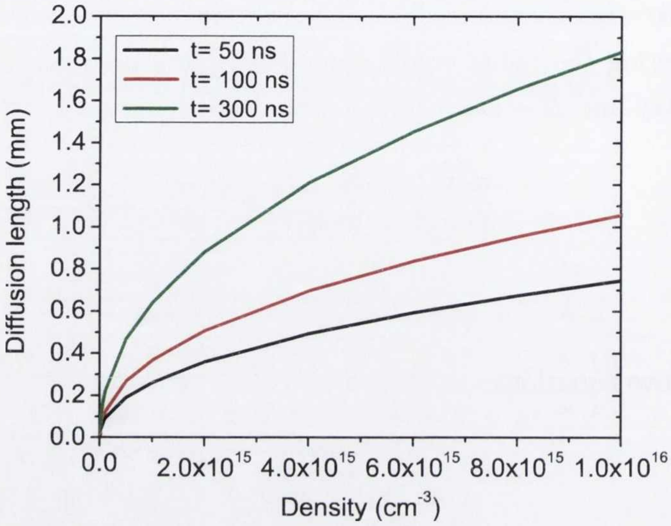

Figure 1.5: Diffusion length calculated for a copper plasma at 1 *eV* expanding in a 320 *mT* magnetic field.

plasma, M_0, the magnetic field, B, and the plume position, r:

$$g = \frac{\pi B^2}{\mu_0 M_0} r^2 \tag{1.49}$$

Thus the deceleration is proportional to B^2.

If $\beta > 1$ the plasma expansion is mainly driven by its kinetic and thermal energies. As a result, the charged particles diffuse through the region occupied by the magnetic field. The diffusion coefficient of the charged particles perpendicular to a field is related to the field strength. Magnetic fields do not affect motion in the parallel direction. Charged particles will move freely along the B-field and only collisions with other particles will retard the diffusion. By comparison, in the perpendicular direction, the B-field reduces the rate of diffusion, while collisions enhance it. This can be explained as follows. For a steady state plasma, the equations (1.30) and (1.35) can be solved for the perpendicular component of the plasma fluid velocity to give [39]:

$$\mathbf{v}_{\perp} = \frac{\mathbf{E} \times \mathbf{B}}{B^2} - \frac{\eta_{\perp}}{B^2}\nabla p \tag{1.50}$$

where $\eta_{\perp}$ is the perpendicular resistivity. The first term is the $\mathbf{E} \times \mathbf{B}$ drift of both ions and electrons together. The second term is the diffusion velocity in the direction of $-\nabla p$. The flux associated with diffusion is:

$$\Gamma_{\perp} = nv_{\perp} = -\frac{\eta_{\perp} n 2k_B T}{B^2}\nabla n \tag{1.51}$$

This has the form of the Fick law $\Gamma_{\perp} = D_{\perp}\nabla n$, with the diffusion coefficient $D_{\perp}$:

$$D_{\perp} = \frac{\eta_{\perp} n 2k_B T}{B^2} \tag{1.52}$$

This is the classical diffusion coefficient for fully ionized gas. It is proportional to $1/B^2$, hence the higher the magnetic field strength the lower the diffusion across the magnetic field. Furthermore, since $\eta \propto \nu_{ei}$, $D_{\perp}$ is also proportional to the collision frequency, ν_{ei}. Hence, as anticipated above, collisions contribute to the diffusion across the field lines. In the absence of collisions, the particles will continue to gyrate around the same magnetic field line. It also should be noted that $D_{\perp}$ defines a diffusion coefficient of the fluid. This means that both ions and electrons diffuse at the same rate and the diffusion is said to be ambipolar.

Fig. 1.5 shows the diffusion length, $L_{D_{\perp}}$ ($L_{D_{\perp}} = \sqrt{D_{\perp}t}$), as a function of the density calculated for a copper plasma at 1 eV expanding in a 320 mT magnetic field for three different times, t. The diffusion length is comparable with the typical size of the plasma at the specific time delays. Hence the exclusion of the magnetic field from the plasma interior is not complete, indicating that resistive MHD is the most appropriate approach.

A better expression for $D_{\perp}$ is given by the semi-empirical formula given by Bohm [39]:

$$D_{B\perp} = \frac{1}{16}\frac{k_B T_e}{eB} \tag{1.53}$$

1.2.3 Plasma focusing

In this section the two fluid model is considered to describe a situation where a combination of external electric and magnetic fields are used to control the plasma expansion. The main problem associated with the production and the maintaining of an electric field within a plasma is the high mobility of the electrons. To determine the conditions under which an electric field can exist in the plasma it is necessary to examine the dynamics of the plasma electrons. For this purpose, it is useful to re-write the equation of motion (1.24) for the electrons:

$$m_e n_e \left[\frac{\partial \mathbf{v}_e}{\partial t} + (\mathbf{v}_e \cdot \nabla)\, \mathbf{v}_e \right] = -en_e (\mathbf{E} + \mathbf{v}_e \times \mathbf{B}) - \nabla p_e - \frac{en_e}{\sigma} \mathbf{j}$$

It can be seen that there are four factors that can produce an electric field in the plasma: the electron inertia, the electron pressure gradient, the Lorentz force and the friction between electrons and ions. The electron inertia and the ohmic term are usually small [41] compared to the Lorentz force and can then be neglected. In the simpler case of cold plasma ($T = 0\ eV$) where the pressure gradient can be neglected, the equation above becomes:

$$\mathbf{E} = -\mathbf{v}_e \times \mathbf{B} \tag{1.54}$$

This equation shows that an electric field can exist in the plasma if a magnetic field, $\boldsymbol{B}$, and an electron motion across the field, $\mathbf{v}_e$, exist. The electric field will then be orthogonal to both $\boldsymbol{B}$ and $\mathbf{v}_e$. The equation (1.54) also expresses an important property of the magnetic field in the plasma - that the magnetic field lines are equipotentials with respect to the electric field. This property is the basis of the plasma lens for focusing neutralized ion beams.

To justify neglecting the electron inertia, the ohmic and pressure gradient terms, an order of magnitude estimate of those terms follow. In the experiment described in Chapter 6, a plasma lens was used to focus the plasma. The plasma lens was placed $\sim 4\ cm$ from the target. To estimate the terms in equation (1.24), the conditions of the plasma at the lens entrance are considered. Fig. 1.6(a) shows the ion current density at 4 cm from the target. The maximum ion flux occurs at about 2.6 μs, which corresponds to a velocity of about $1.5 \times 10^6\ cm\ s^{-1}$. Fig.

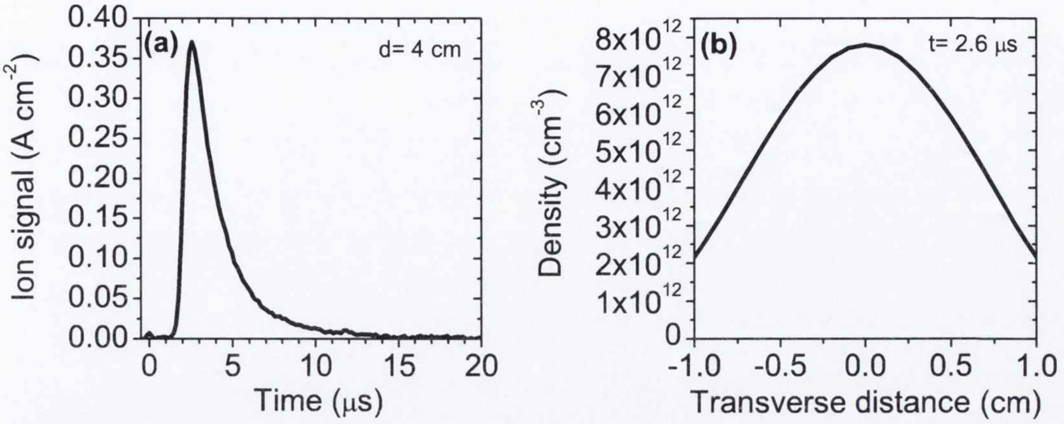

Figure 1.6: (a) Ion current density at 4 *cm* from the target and (b) corresponding transverse ion density profile calculated at the time of maximum ion flux, $t = 2.6\ \mu s$.

1.6(b) shows the density profile in the transverse direction at the time of maximum ion flux and at 4 *cm* from the target calculated using equation (1.15).

- **Estimate of $(\mathbf{v}_e \times \mathbf{B})$ term**

  v_e can be considered equal to the ion velocity $1.5 \times 10^6\ cm\ s^{-1}$, hence for a magnetic field of 320 *mT* the above term is

  $$\mathbf{v}_e \times \mathbf{B} \approx 5 \times 10^3\ V\ m^{-1}$$

- **Estimate of $(\nabla P_e / en_e)$ term**

  Considering a uniform temperature, the pressure gradient can be expressed in terms of density gradient: $\nabla p_e \approx k_B T \nabla n_e$. In Fig. 1.6(b) it can be seen that the density changes of a factor of 2 over a distance of about 5 *mm*. Hence the density gradient is approximately $\nabla n_e \approx (2 \times 10^{18} / 5 \times 10^{-3})\ m^{-4} = 4 \times 10^{20}\ m^{-4}$. Thus for a temperature of 1 *eV* and density of $8 \times 10^{18}\ m^{-3}$ the pressure gradient term is:

  $$\frac{\nabla P_e}{en_e} \approx \frac{k_B T \nabla n_e}{en_e} \approx 50\ V\ m^{-1}$$

- **Estimate of $(\mathbf{j}/\sigma)$ term**

The conductivity is given by $\sigma = n_e e^2 / m_e \nu_{ei} = 1.6 \times 10^3 \ \Omega^{-1} m^{-1}$. j can be approximated with the peak of the ion current density in Fig. 1.6(a), thus obtaining:

$$\frac{j}{\sigma} \approx 2 \ V \ m^{-1}$$

- **Estimate of $(m_e/e)(d\mathbf{v}_e/dt)$ term**

  For a scale length of 5 *mm* for the inhomogeneities and electron velocity of $1.5 \times 10^6 \ cm \ s^{-1}$, the inertial term is:

  $$\frac{m_e}{e} \frac{d\mathbf{v}_e}{dt} \approx 0.3 \ V \ m^{-1}$$

1.2.3.1 Plasma lens

The idea of the plasma lens was first introduced by Gabor [42]. Gabor proposed to use the electrostatic field of magnetized electrons for focusing ion beams. This lens works with non-neutral plasma. In order to focus an ion beam with a given charge sign a non neutral plasma with the opposite charge sign as the beam is required. Later Morozov [43] described the basic concept of plasma-optics for creation of electromagnetic fields in quasi-neutral plasmas. Based on this principle several experimental investigations followed to optimize this type of lens for ion beam manipulation.

Electrostatic plasma lenses have been successfully used to focus high current - of the order of 10 – 1000 *mA* - ion beams of energy up to several tens *keV* [44, 45, 46]. The main applications of these lenses are in ion implantation for materials surface modification and particle accelerator injection for nuclear physics research. The ion beam is extracted from a plasma, which is typically produced by vacuum arc discharge. The energetic ion beam is then transported to the plasma lens, where it is focused. A schematic of a plasma lens is shown in Fig. 1.7. This lens consists of a set of cylindrical ring electrodes located within an external magnetic field with field lines connecting ring electrode pairs symmetrically about the lens midplane. Typically these lenses have diameters of about 7 – 10 *cm* and length of about 15 *cm*; the number of electrodes used varies typically from 5 to 13, with the outermost electrodes grounded.

Electrostatic plasma lenses have been developed for focusing high current ion

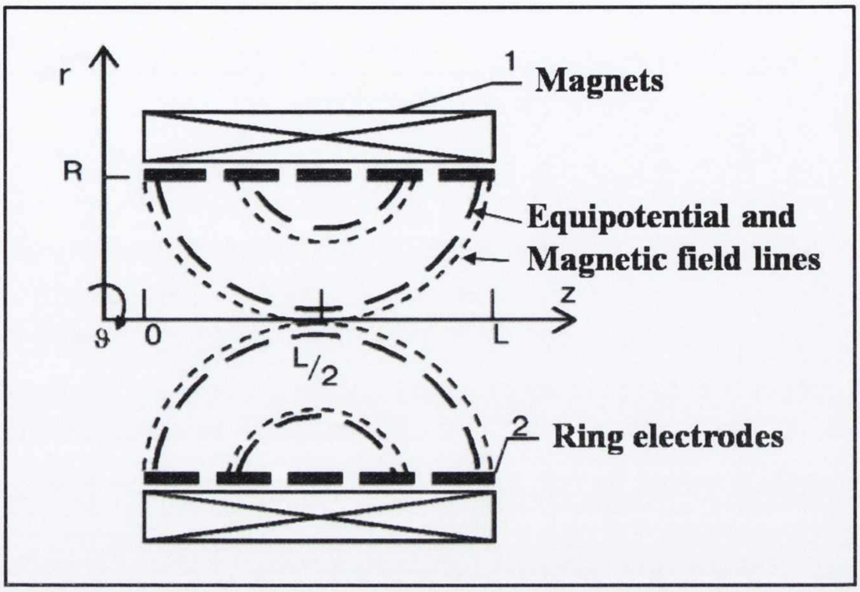

Figure 1.7: Simplified schematic of the plasma lens [44]. (1) magnetic field coil, (2) cylindrical electrodes, (dashed lines) equipotentials lines, (dotted lines) magnetic field lines, (R) lens radius, (L) lens length.

beams. High current ion beams are subject to strong electrostatic space charge forces. If the space field is not compensated it can causes the beam to blow up. Therefore, to ensure focusing of the beam it is very important to preserve the quasi-neutrality. The neutralizing electrons within the lens volume are mainly produced by secondary emission due to collisions of the ions with the lens electrodes. Hence this type of ion beam can be viewed as quasi-neutral plasma. However the presence of electrons in the beam makes the use of vacuum electrostatic lenses, as used for focusing lower current beams, impossible. As mentioned above, this is because of the high mobility of the electrons which results in the loss of space-charge neutralization and which in turn compromise the focusing properties of the lens. Therefore the plasma lens is based on the space charge neutralization while maintaining the magnetic field lines as equipotentials. It has been already shown above that the electrons in an expanding LPP can be easily magnetized. Hence, inside the lens volume the electrons will move along the field lines while gyrating around them. As a consequence they tie the potential of the electrode to which the field line is attached, maintaining the magnetic field lines at equipotentials.

This creates the electric field in the plasma that will focus the ion beam.

The focusing properties of a plasma lens depends on several parameters including the value of the beam current, the potential distribution at the electrodes, the size and number of the electrodes and the magnetic field. In particular, the magnetic and electric field configuration should eliminate spherical aberrations and transfer the ground potential of the outermost lens electrodes to the beam axis at the midplane. It was theoretically predicted [43] that a lens without spherical aberrations can be obtained by creation of the optimum magnetic field configuration, by selection of the optimum distribution of externally applied ring-electrode potentials and by optimization of the number and dimensions of ring electrodes. When spherical aberrations are removed the focal length of the electrostatic plasma lens is given by [47, 48]:

$$F = \frac{\theta \varphi_b R}{2\varphi_L} \tag{1.55}$$

where φ_b is the ion beam accelerating potential, φ_L is the electric potential on the ring electrodes and θ is a geometric parameter that depends on the ratio of lens radius, R, to lens length, L, and the magnetic field configuration and is given by:

$$\theta = \frac{\pi R}{L} I_1(\frac{r}{R}) \tag{1.56}$$

where I_1 is the modified Bessel function of first order. Goncharov et al. [48] found that for the optimal configuration $\theta \approx 1$. The axial component of the optimal magnetic field is then given by:

$$B_z = B_0 I_0(\frac{r}{R}) sin(\frac{\pi z}{L}) \tag{1.57}$$

where I_0 is the modified Bessel function of order zero. In order to eliminate spherical aberrations, the optimum electric field created within the lens volume should have linear variation along the radius of the plasma lens [47, 49, 50]. Theoretically [43], such an electric field can be created by setting the potentials on the lens electrodes directly proportional to the value of the magnetic field strength near the axis of the lens. This potential distribution is referred to as the optimal distribution. However, Goncharov et al. in [50] showed experimentally that for a given lens potential distribution, the creation of $E \propto r$ does not occur for all ion beam currents. Hence the potential distribution needs to be adjusted depending on the particular experimental condition. By creation of the optimum magnetic field configuration and by selection of the appropriate externally applied potential distribution of the lens electrodes and ion beam current, spherical aberrations were removed [46, 49, 50]. Goncharov et al. [46, 51] recorded an ion beam compression up to a factor of 30 and an increase in the total transported ion beam current by up to 30% when the lens was used. Moreover, they have also shown that aberrations may play a beneficial role, because they can be used to control the radial beam profile at the lens output. In particular, they can be used to create a uniform beam profile [50].

Although these plasma lenses work with neutralized ion beams with different characteristics to plasma produced by laser ablation, it seems an interesting perspective to explore the possibility of using a plasma lens to control laser produced plasmas (LPPs). In particular, it is of interest in PLD, to explore the possibility of focusing LPPs to increase the deposition rate and also to investigate the effect of spherical aberration to produce a uniform deposition profile.

1.3 Optical emission spectroscopy

Key parameters of laser produced plasmas are temperature and density. The presence of excited species within the plasma plume allows the use of optical emission spectroscopy as a diagnostic technique to analyse the plasma. Photons are emitted and absorbed by the atoms in the plasma during electronic transitions. The electronic transitions can be divided in three groups: bound-bound, bound-free and free-free. The bound-bound transitions occur between two electronic bound levels. The absorption or emission of a photon results in excitation or de-exciation of the atom. Because of the discreteness of the energy levels of the bound electronic states, these transitions result in a discrete spectra producing line radiation of a specific photon energy. The bound-free transitions occur when the absorbed photon has energy exceeding the binding energy of the electron resulting in photoionization of the parent atom. The excess of the photon energy over the binding energy is transformed into kinetic energy of the free electron. The reverse transition is photorecombination, that is the capture of a free electron by an ion and results in the emission of a photon. Since the free electron can assume any positive value of energy, the bound-free transitions have a continuum spectra. Finally, the free-free transitions are the Bremsstrahlung and inverse Bremsstrahlung and also have continuum spectra.

When analyzing emission from laser produced plasmas, a strong continuum is observed within the first few nanoseconds after the laser pulse. This emission is due to the dense plasma layer in the vicinity of the target surface, in which many collisions lead to severe Stark-broadening. As time elapses, discrete spectral lines will begin to form producing a spectrum characteristic of the particular material being ablated. The discrete spectra of the bound-bound transitions not only give information on the particular radiating species as the plasma plume expands, but also on temperature and density. Therefore in this work the bound-bound transitions spectra have been analysed. In order to detect this emission, a spectrometer coupled with an intensified charge coupled device (ICCD) was used. With this system spectra resolved in time and space were obtained. The details of the experimental system are discussed in the next chapter.

The most widely used methods to extract the plasma parameters by plasma spectroscopy are based on the assumptions that the plasma is in local thermodynamic equilibrium (LTE) and optically thin. These two assumptions will be discussed herein.

1.3.1 Local thermodynamic equilibrium

The most frequently used methods for the determination of the temperature of a plasma by optical emission spectroscopy are based on the application of two equilibrium relations. The first one is the Boltzmann equation, which describes the population densities of excited energy levels as a function of temperature T and is given by:

$$\frac{n_2}{n_1} = \frac{g_2}{g_1}\, exp\Big(-\frac{E_2 - E_1}{k_B T}\Big) \tag{1.58}$$

where $n_{1/2}$ and $g_{1/2}$ are the number densities and the degeneracies of the lower and upper energy states E_1 and E_2, respectively. Secondly, the Saha equation (1.9) relates the densities of subsequent ionization species for a temperature T. The applicability of these equations relies on the validity of thermodynamic equilibrium

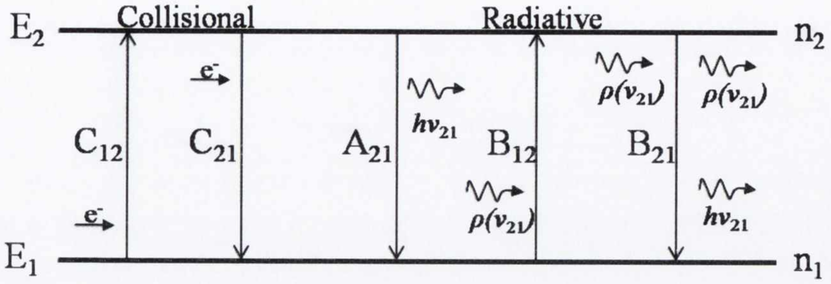

Figure 1.8: Schematic of collisional and radiative processes for a two-level atom.

or local thermodynamic equilibrium. LTE is a state in which the temperature T of the Boltzmann and Saha equations is equal to that of the Maxwell–Boltzmann velocity distribution of free electrons, but T may vary from point to point in the plasma. A plasma with line emission spectra is obviously not in global thermodynamic equilibrium, but it can be in LTE. In a plasma the processes of excitation and ionisation and recombination can be the result of either collisional or radiative effects. Examples of these mechanisms are: excitation and de-excitation; collisional ionisation and three body recombination; autoionization and dielectronic recombination; photoionization and radiative recombination. All these rates depend on the electron temperature and density in the plasma. For LTE to hold in a plasma, the collisions with electrons have to dominate over the radiative processes. This condition requires a sufficiently large electron density. A criterion proposed by McWhirter is based on the existence of a critical electron density for which collisional rates are at least ten times the radiative rates [52].

In order to find a criterion for LTE a simple two level system can be considered. Fig. 1.8 shows a schematic of a two-level system with a lower energy level E_1 and upper level E_2, having respective populations n_1 and n_2. There are three possible radiative processes between the two levels. First, an atom in the excited level 2 can spontaneously decay to level 1 with emission of a photon of energy $E_2 - E_1 = h\nu_{12}$. The process is described by the Einstein coefficient A_{21} which is the probability per unit time of this transition to occur. The number of such transitions per second is $A_{21}n_2$. Secondly, in the presence of radiation of density ρ an atom in level 1 can absorb a photon of energy $h\nu_{12}$ and move to level 2 with probability $B_{12}\rho$. The process is described by the Einstein coefficient B_{12} and the number of these transitions per second is $B_{12}\rho\, n_1$. Finally, in the presence of radiation, the probability of a stimulated emission from level 2 to level 1 with emission of energy $h\nu_{12}$ is $B_{21}\rho$ and the number of transitions per second is $B_{12}\rho\, n_2$. C_{12} and C_{21} are the collisional excitation and de-excitation transition rates, respectively. The number of transitions per second is $n_e n_1 C_{12}$ and $n_e n_1 C_{12}$, where n_e is the electron numebr density. If the two level atom in Fig. 1.8 is in equilibrium, the level populations n_1 and n_2 do not change with time and hence the upward and downward transitions are equal:

$$n_1 \rho B_{12} + n_1 n_e C_{12} = n_2 \rho B_{21} + n_2 A_{21} + n_2 n_e C_{21} \tag{1.59}$$

For small values of ρ the above equation reduces to:

$$\frac{n_2}{n_1} \approx \frac{C_{12}}{C_{21}} \left(1 + \frac{A_{21}}{n_e C_{21}}\right)^{-1} \tag{1.60}$$

For the principle of detailed balance, in thermodynamic equilibrium the collisional rates must balance, i. e.:

$$n_1 C_{12} = n_2 C_{21} \tag{1.61}$$

and this relation must hold separately for each type of collision. As can be seen from the last two equations, the collisional equilibrium in which $n_1 C_{12} = n_2 C_{21}$, is perturbed by the spontaneous radiation, represented by A_{21}. Therefore, based on the above criteria, the following inequality must hold for LTE:

$$n_e >> \frac{A_{21}}{C_{21}} \tag{1.62}$$

The above leads to the McWhirter condition [53] given by:

$$n_e \geq 1.6 \times 10^{12} \sqrt{T_e}\, (\Delta E)^3\ cm^{-3} \tag{1.63}$$

where T_e is the electron temperature in K and ΔE is the energy level difference of the considered transition and is in eV.

From equation (1.59) it is possible to derive the relationships between the Einstein coefficients in the case of thermal equilibrium. The Einstein coefficients A_{21}, B_{12} and B_{21} are fixed probabilities associated with each atom and do not depend on the state of the system of which the atoms are a part. Therefore, the relationships derived at thermal equilibrium are valid universally. Using the Boltzmann equation (1.58) and the blackbody distribution, the relations between the Einstein coefficients are give by:

$$g_1 B_{12} = g_2 B_{21} \tag{1.64}$$

$$A_{21} = \frac{8\pi h \nu_{12}^3}{c^3} B_{21} \tag{1.65}$$

1.3.2 Optically thin plasma

For a system in thermodynamic equilibrium the radiative emission and absorption are balanced and the radiation density, ρ, is given by the Planck blackbody distribution. This system is not accessible to optical emission spectroscopy because it is optically thick. The detection of an emission line depends on the probability of a photon escaping without being absorbed. This probability depends on the number of absorbers in the medium and on the probability of absorption at a particular transition, which is described by B_{12}. If α_λ is the absorption coefficient and I_λ is the incident irradiance at wavelength λ, the change in the irradiance, δI_λ, due to the absorption in a layer of thickness δx is:

$$-\delta I_\lambda = I_\lambda \alpha_\lambda \delta x \tag{1.66}$$

Integrating the above equation for a layer of thickness l, one obtains Beer's law:

$$I_\lambda(l) = I_\lambda^0 e^{-\tau_\lambda(l)} \tag{1.67}$$

where I_λ^0 is the incident irradiance and τ_λ is the optical depth and is given by:

$$\tau_\lambda = \int_0^l \alpha_\lambda dx \tag{1.68}$$

For a homogeneous layer: $\tau_\lambda = \alpha_\lambda l$. When $\tau_\lambda << 1$ the plasma is said to be optically thin; conversely if the optical depth is greater than unity it is said optically thick. The integrated absorption coefficient is related to the Einstein coefficient

B_{12} by the relation:

$$\int_{line} \alpha(\lambda) d\lambda = n_1 B_{12} \frac{h}{\lambda_0} \tag{1.69}$$

where λ_0 is the central wavelength of the line. The absorption coefficient can be expressed in terms of a particular transition as [53]:

$$\alpha(\lambda) = \frac{e^2 n_1 f_{12}}{4\epsilon_0 m_e c} L(\lambda) \tag{1.70}$$

where e is the charge of the electron, ϵ_0 is the permittivity of vacuum, f_{12} is the oscillator strength between the lower and upper level involved in the transition and $L(\lambda)$ is the line shape function. The oscillator strength determines the emitted signal strength and is related to the transition probability, A_{21}, between levels by the relation:

$$f_{12} = \frac{g_2}{g_1} \frac{\epsilon_0 m_e c \lambda^2}{2\pi e^2} A_{21} \tag{1.71}$$

1.3.3 Spectroscopic measurement of temperature

As discussed above, when the conditions of a plasma are such that LTE applies, the populations of the bound states follow the Boltzmann distribution. In this case the temperature can be found by measuring relative intensities of the emission lines of known transition probability. The irradiance of a spectral line is related to A_{21} and to the population of the upper state n_2 by the relation:

$$I_{21} = \int j(\lambda) l d\lambda = l \frac{n_2 A_{21} hc}{4\pi \lambda_{12}} \quad [W\ m^{-2}\ sr^{-1}] \tag{1.72}$$

where l is the plasma thickness and $j(\lambda)$ is the emissivity, defined as the power emitted per unit solid angle per wavelength by unit volume and is measured in $[W\ m^{-3}\ sr^{-1}\ nm^{-1}]$. Hence substituting n_2 with the expression given by the Boltzmann equation (1.58), the irradiance is:

$$I_{21} = const. \frac{g_2 A_{21}}{\lambda_{21}} e^{-E_2/k_B T} \tag{1.73}$$

The constant in the above equation includes terms common to all the lines. The ratio of the irradiance of two lines in the same ionisation stage with upper energy levels i and j is:

$$\frac{I_i}{I_j} = \frac{g_i A_i \lambda_j}{g_j A_j \lambda_i} e^{-(E_i - E_j)/k_B T} \tag{1.74}$$

When more that two lines of the same ionisation species are present in the spectra, the excitation temperature can be extracted using the Boltzmann plot method. From equation (1.73), a plot of $ln(I\lambda/gA)$ against the upper level energy E_2, for several spectral lines, should therefore be a straight line of slope $1/k_B T$. Hence from the slope, T can be estimated. The linearity of the Boltzmann plot reflects the agreement between the Boltzmann distribution and the experimentally measured line irradiance. Hence the Boltzmann plot method is also useful to check the existence of LTE.

It is also possible to determine the temperature from two lines of different ionisation stages. Combining the Saha (1.9) and Boltzmann distributions (1.58) the so-called Saha-Boltzmann equation is obtained:

$$\frac{n_e n_{(z+1),k}}{n_{z,j}} = \frac{2(2\pi m_e k_B T)^{3/2}}{h^3} \frac{g_{(z+1),k}}{g_{z,j}} exp\left(-\frac{E_z + E_k - E_j}{k_B T}\right) \tag{1.75}$$

where $n_{z,j}$ and $n_{(z+1),k}$ are the number densities of the ions in two different ionisation stages z and *(z+1)* with respective upper states j and k and E_z is the ionisation energy of the *zth* ionisation stage. The Saha-Boltzmann equation can be expressed in terms of relative line intensities instead of number densities by substituting equation (1.72) into (1.75). Thus the relative irradiance of lines from subsequent ionization stages of the same element are given by:

$$\frac{I_{(z+1),k}}{I_{z,j}} = \frac{A_{(z+1),k}}{A_{z,j}} \frac{\lambda_{z,j}}{\lambda_{(z+1),k}} \frac{2(2\pi m_e k_B T)^{3/2}}{h^3 n_e} \frac{g_{(z+1),k}}{g_{z,j}} exp\left(-\frac{E_z + E_k - E_j}{k_B T}\right) \tag{1.76}$$

Similarly to the Boltzmann equation, also the above Saha-Boltzmann equation can be linearised by taking the logarithm:

$$ln\left(\frac{I_{(z+1),k}\, A_{z,j}\, g_{z,j}\, \lambda_{(z+1),k}}{I_{z,j}\, A_{(z+1),k}\, g_{(z+1),k}\, \lambda_{z,j}}\right) = ln\left[\frac{2(2\pi m_e k_B T)^{3/2}}{h^3 n_e}\right] - \frac{E_z + E_k - E_j}{k_B T} \tag{1.77}$$

Note that the intercept may be useful to determine the plasma electron density.

1.3.4 PrismSPECT simulations

A widely used method for electron density determination uses the broadening of emission lines due to the Stark effect [54, 55]. The Stark effect in plasmas is due to collisions of the emitting atoms with electrons and ions, resulting in a broadening of the line and a shift of the peak wavelength. An estimation of the full width of the broadened line for neutral atoms is given by [56]:

$$\Delta\lambda = 2w\frac{n_e}{10^{16}} + 3.5A\left(\frac{n_e}{10^{16}}\right)^{5/4}\left(1 - \frac{3}{4}N_D^{-1/3}\right)w \tag{1.78}$$

where $\Delta\lambda$ is in $\mathring{A}$, the electron density n_e is in cm^{-3}, N_D is the number of particles in the Debye sphere, A and w are in $\mathring{A}$ and are, respectively, the ion broadening parameter and the electron impact width parameter. The first term in equation (1.78) is the broadening contributions due to electrons, while the second term is due to the ions. Generally the electron contribution dominates the Stark-broadened profile and the ionic term can be neglected. However, the width of the measured spectral lines is limited by the resolution of the spectrometer, which in our case was 0.75 nm. As an example, using equation (1.78), the broadening of the neutral copper line at 515 nm can be estimated. For a typical density of $\sim 10^{16}$ cm^{-3} and a temperature of 1 eV, the electron Stark width, $\Delta\lambda$, is 0.38 nm, where the Stark width parameter, w, is 0.19 nm [57]. Hence, in our experimental set-up the spectral resolution of our instrument was not sufficient to use Stark broadening for the measurement of electron density. However, in this thesis a spectral synthesis computer code, PrismSPECT [58], was used to infer plasma conditions, including density, from spectroscopic measurements.

PrismSPECT is a commercially available software package made by Prism Computational Science Inc. [58]. For a set of input plasma parameters, like temperature, density and dimensions of the plasma, the software calculates the collisional-radiative ionization and excitation equilibrium as well as the emitted spectrum for a plasma with uniform temperature and density. A wide range of elements can be simulated, including multi-element plasmas with given relative compositions. The PrismSPECT software can be run in both LTE and non-LTE modes. When LTE is specified, the atomic level populations are calculated using

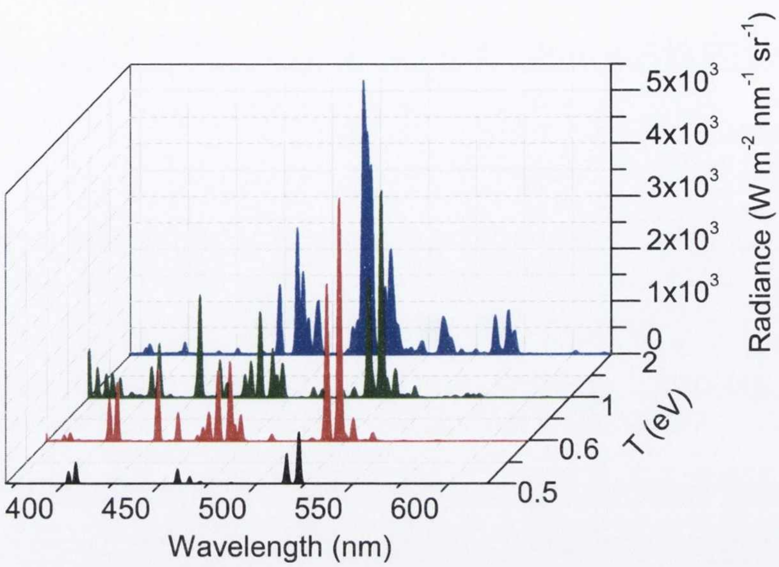

Figure 1.9: PrismSPECT spectra calculated in non-LTE mode at increasing temperatures for a slab of copper plasma of constant thickness (= 10 mm) and ion density (= 1×10^{16} cm^{-3}).

Saha's equation and Boltzmann's statistics. If non-LTE is assumed, the calculations are made by solving a coupled set of atomic rate equations. These equations account for several atomic processes, including collisional ionization and recombination, photoionization and stimulated recombination, radiative recombination and autoionization, dielectronic recombination and electron capture, collisional excitation and de-excitation, photoexcitation and stimulated emission and spontaneous emission.

Since our experimental spectra are absolutely calibrated, by fitting the measured spectra to that calculated, it was possible to derive plasma parameters such as temperature, density, ionization fraction and atomic level populations. As an example, Fig. 1.9 shows a sequence of spectra obtained with PrismSPECT in non-LTE mode at increasing electron temperature for a slab of copper plasma of 10 mm thickness and density of 1×10^{16} cm^{-3}. For the spectroscopy measurements the plasma is viewed at right angle to the target normal. Thus the spectrometer records emission from a plasma thickness equal the transverse dimension of the plume at the relevant distance from the target surface. Typically we record the

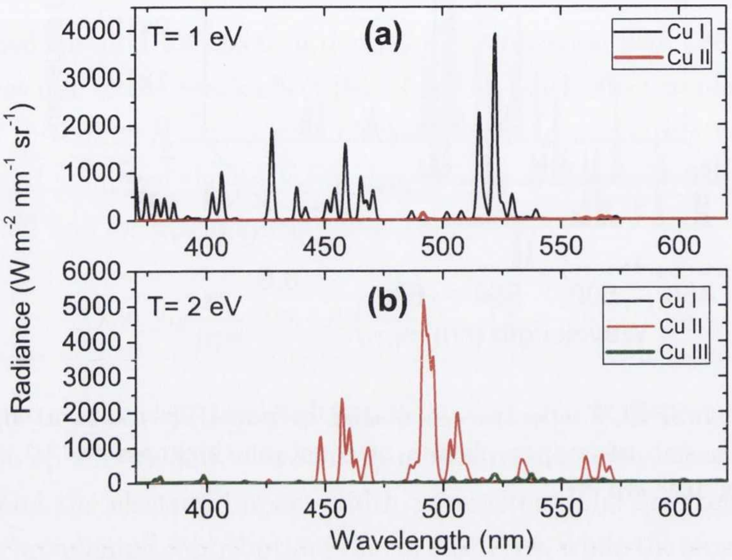

Figure 1.10: Spectral components of the spectra showed in Fig. 1.9 relative to (a) 1 *eV* and (b) 2 *eV*.

spectra when the transverse plume dimension is $5 - 10\ mm$, then a plasma thickness of $10\ mm$ was chosen for illustrative PrismSPECT calculations. From the sequence in Fig. 1.9 we can see how the relative intensities of the spectral lines and the plasma ionization change with temperature. With increasing temperature the ionization of the plasma increases and therefore the ionic lines increase. The software also allows us to plot separately the contribution of the several ionic species to the total spectra. Fig. 1.10 shows the ionic contribution to the spectra of Fig. 1.9 relative to 1 and 2 *eV*. It can be seen that at 1 *eV* the emission is mainly due to neutral copper, Cu I. From 1 *eV* to 2 *eV* the neutral lines decrease; at 2 *eV* the neutral lines become irrelevant and the prominent lines in the spectra are Cu II lines.

The populations of energy levels is another feature of the software and can be plotted as a function of temperature or density. An example for varying density is shown in Fig. 1.11. This figure shows the calculated population of the level $3d^{10}4d\ ^2D_{5/2}$ relative to the level $3d^{10}4p\ ^2P_{3/2}$ of neutral copper. Fig. 1.12 shows

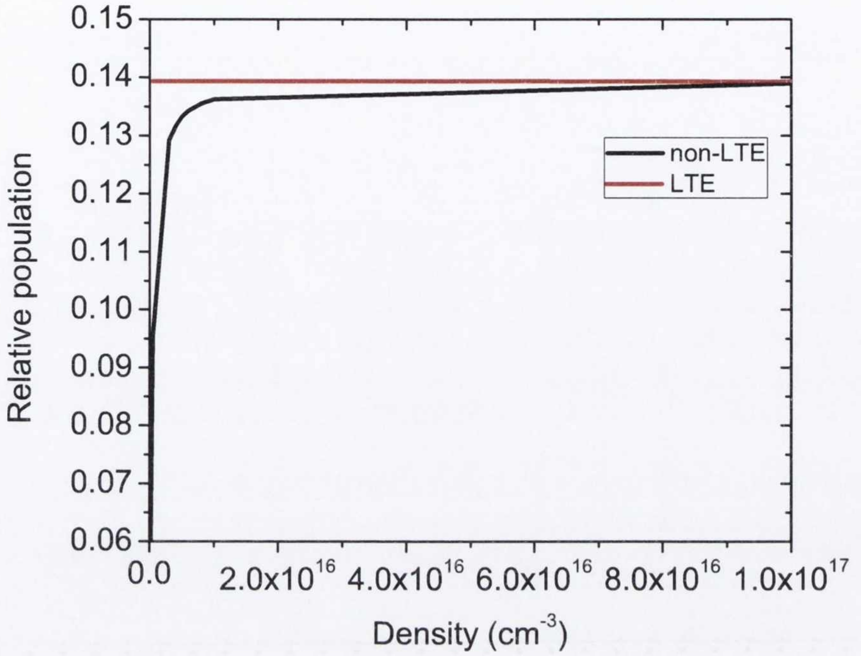

Figure 1.11: Comparison between LTE and non-LTE calculations of the Cu I population of the level $3d^{10}4d\ ^2D_{5/2}$ relative to the level $3d^{10}4p\ ^2P_{3/2}$ as function of the electron density. The calculations were done for a plasma of 1 eV and 10 mm thick.

an abbreviated Grotrian diagram for neutral Cu, including the transitions considered here. The calculation was done in both LTE and non-LTE cases for a copper plasma at 1 eV and 10 mm thick. From these calculations it can be seen that the relative populations of the levels considered are within 10% of the LTE values for an electron density $\geq 2 \times 10^{15}\ cm^{-3}$. This result can be compared with McWhirter's criterion (1.63). From Fig. 1.12, ΔE between $3d^{10}4d\ ^2D_{5/2}$ and $3d^{10}4p\ ^2P_{3/2}$ levels is 2.4 eV, thus, according to McWhirter's criterion, for a temperature of about 1 eV, the electron density required to mantain LTE between the considered levels should be $\geq 2.4 \times 10^{15}\ cm^{-3}$. This agrees with the PrismSPECT calculations. Fig. 1.13 shows the spectra calculated with PrismSPECT for two different values of density: $1 \times 10^{15}\ cm^{-3}$ and $6 \times 10^{15}\ cm^{-3}$, respectively, smaller and greater than the critical value of $2.4 \times 10^{15}\ cm^{-3}$. Furthermore, for each density, the spectra were calculated in both LTE and non-LTE conditions and compared in Fig. 1.13. As can be seen, for density $< 2.4 \times 10^{15}\ cm^{-3}$ the spectrum calculated assuming

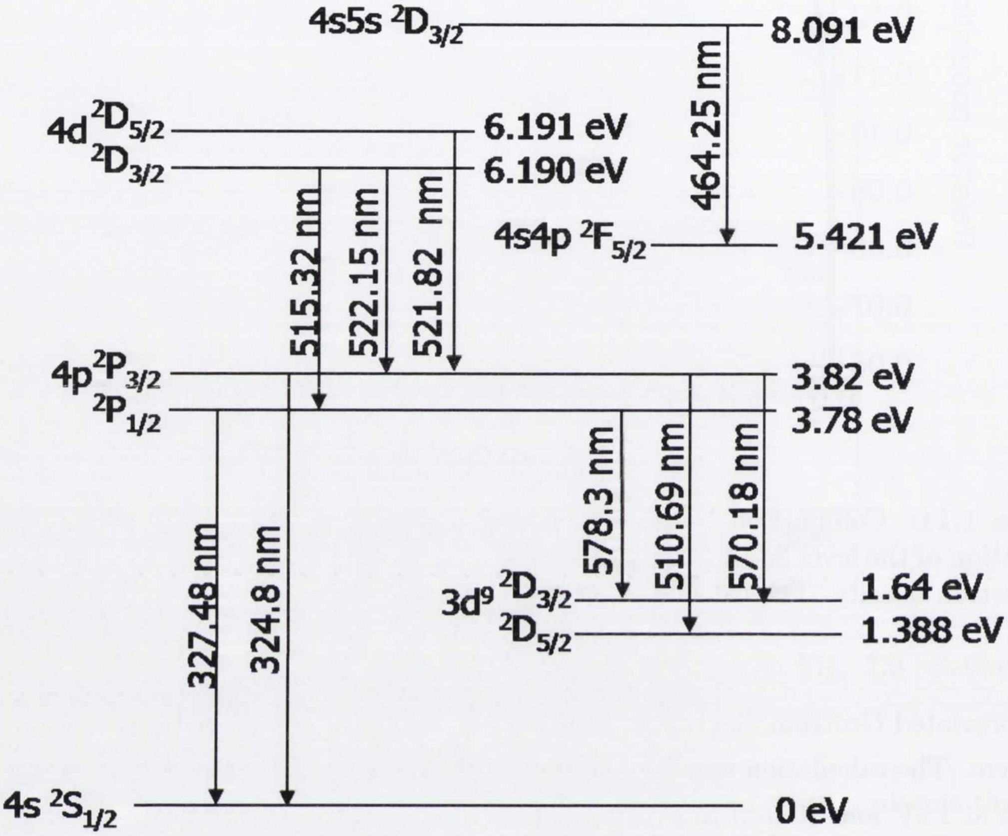

Figure 1.12: Abbreviated Grotrian diagram of neutral copper. The ionization energy is about 7.7 eV.

non-LTE condition is very different from the corresponding LTE spectrum. When the density is $> 2.4 \times 10^{15}\ cm^{-3}$ no relevant differences are observed between the spectra obtained from LTE and non-LTE calculations.

As discussed above, the plasma can emit and absorb photons through three different types of interaction with electrons, which are bound-bound, bound-free and free-free absorption. The PrismSPECT code also calculates the absorption due to each of these mechanisms. In Fig. 1.14 the contribution of the three absorption processes to the total optical depth is calculated as a function of wavelength for 360 μm thick Cu plasma of density $5 \times 10^{18}\ cm^{-3}$ and temperature 3 eV. These

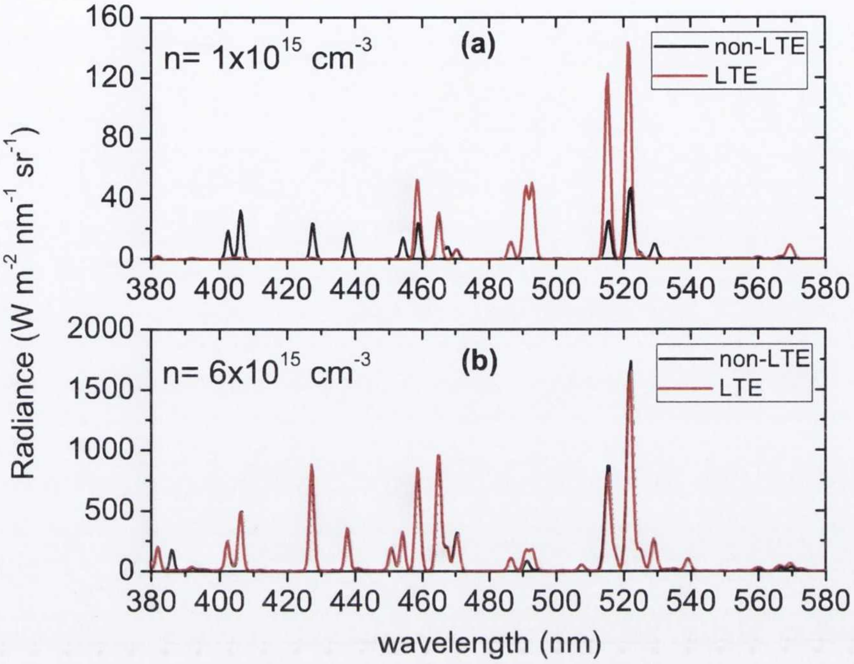

Figure 1.13: Comparison between the spectra calculated with PrismSPECT in LTE and non-LTE mode for a copper plasma at 1 eV, 10 mm thick and ion density of: (a) 1×10^{15} cm^{-3} and (b) 6×10^{15} cm^{-3}.

are typical conditions of a plasma existing on the target surface at the end of the laser pulse. From the optical depths, the absorption coefficients can be calculated and as an example, the values obtained at two different wavelengths are reported in Table 1.3. The values of the free-free absorption coefficient are found to be in a good agreement with the values obtained from equation (1.10). However, at the plasma conditions here considered, the absorption due to the bound-free transitions is found to be $\leq$ of the free-free absorption. In fact, these calculations show that the main mechanism is the absorption due to the bound-bound transitions. The plasma is optically thin and the absorption spectrum is a quasi-continuum due to significant broadening and merging of bound-bound transitions. Hence, this shows that future modelling of the optical properties of laser produced plasma will need to include a detailed treatment of broadened bound-bound transitions.

It is worth noting that the software has a limitation in this analysis. Specifically, in the case of copper, the triplet of neutral lines at 510 nm, 570 nm and

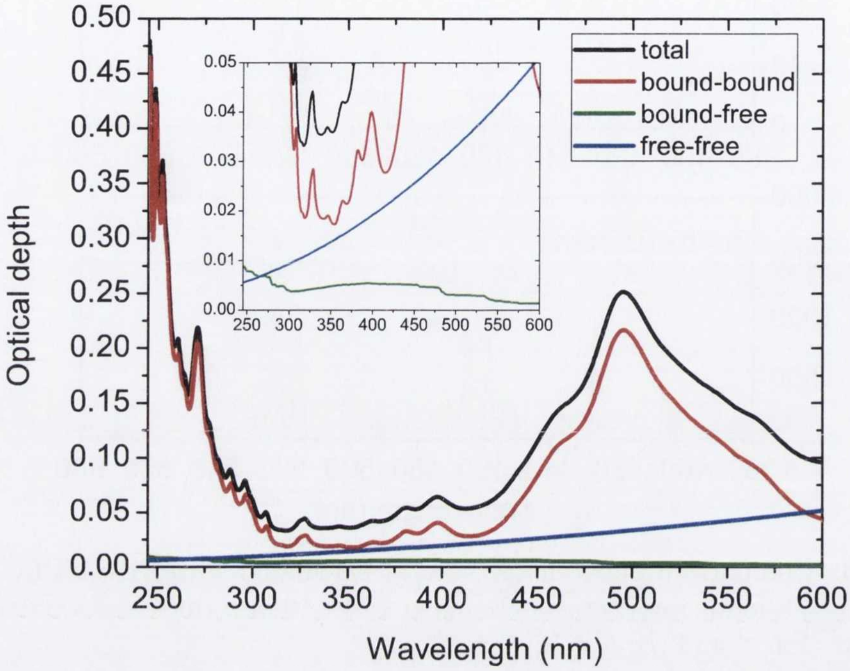

Figure 1.14: Wavelength dependent optical depth calculated for Cu plasma of density 5×10^{18} cm^{-3} and temperature 3 eV. The total optical depth and the contribution from bound-bound, bound-free and free-free transitions are shown. The inset shows part of the optical depth plot with an expanded scale.

λ (nm)	α_{IB} (cm^{-1})	α_{PI} (cm^{-1})	α_{BB} (cm^{-1})
248	0.17	0.22	11
500	0.92	0.08	5.8

Table 1.3: Absorption coefficients of the free-free, α_{IB}, bound-free, α_{PI}, and bound-bound, α_{BB}, transitions at 248 and 500 nm calculated with PrismSPECT.

579 nm are not present. This can be seen in Fig. 1.15 where a comparison between measured and calculated spectra shows the missing neutral lines. The upper and lower levels of the missing transitions are included in the code, but they are not coupled. However, it should be noted that the $4p\ ^2P_{3/2-1/2}$ levels are connected with the ground level through the transitions at 324 and 327 nm, with transition probabilities of about 1.4×10^8 s^{-1}. The transition probabilities of the 510, 570

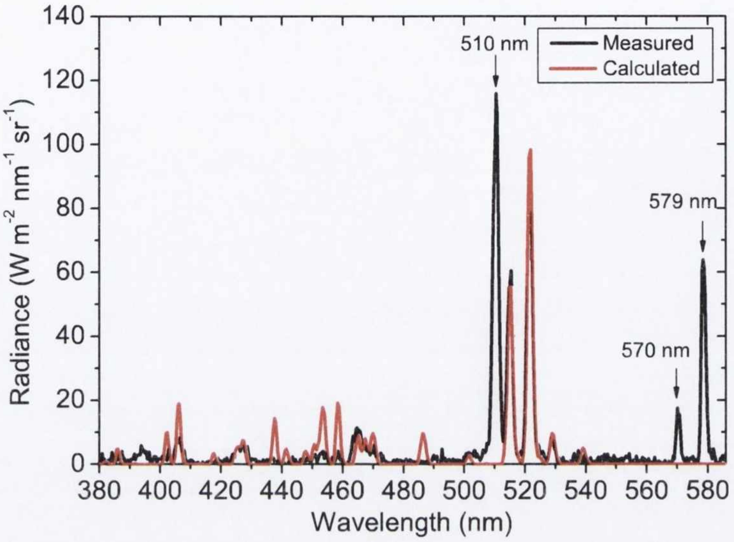

Figure 1.15: Fit of a copper spectra calculated using PrismSPECT and a measured spectra. The calculation was done using non-LTE mode, a temperature of 0.7 eV, an ion density of 7×10^{14} cm^{-3} and a thickness of 10 mm. The arrows indicate the triplet of lines missing in the software.

and 578 nm are much smaller and are, respectively, 2×10^{6} s^{-1}, 2.4×10^{5} s^{-1} and 1.65×10^{6} s^{-1}. Hence, the $4p$ $^2P_{3/2-1/2}$ levels will be depopulated mainly due to the transitions to the ground state. As consequence, the error on the calculations of the populations can be neglected.

Chapter 2

Experimental methods

In this chapter, the experimental and computational techniques deployed during this work are described. The specific magnetic and electric field configurations used to control the expansion of the laser produced plasma are described in subsequent chapters. Here the general set up used to perform laser ablation of solid targets will be discussed along with the diagnostic techniques used to characterize the ablated material - namely, a Langmuir probe, time and space resolved optical emission spectroscopy, fast photography and thin film deposition.

2.1 Experimental setup

A general scheme of the experimental setup is shown in Fig. 2.1. The laboratory where the experiments were conducted contained two laser sources: a Nd:YAG laser with 6 *ns* pulse width and a wavelength of 1064 *nm* and an excimer laser with 20 *ns* pulse width and a wavelength of 248 *nm*. Experiments were conducted using whatever laser was available at the time of the experiment. However, only one laser type was used for any single experiment. The laser light was guided to the vacuum chamber and focused onto a solid target at an angle of 45° with respect to the target surface normal. The target was rotated to reduce drilling. The chamber was pumped down using a roughing and turbo-molecular pump combination (Pfeifer TMH 071), working at a nominal pressure of $10^{-4} - 10^{-5}$ *mbar*.

Measurements of the plasma charge density and its temporal dynamics were

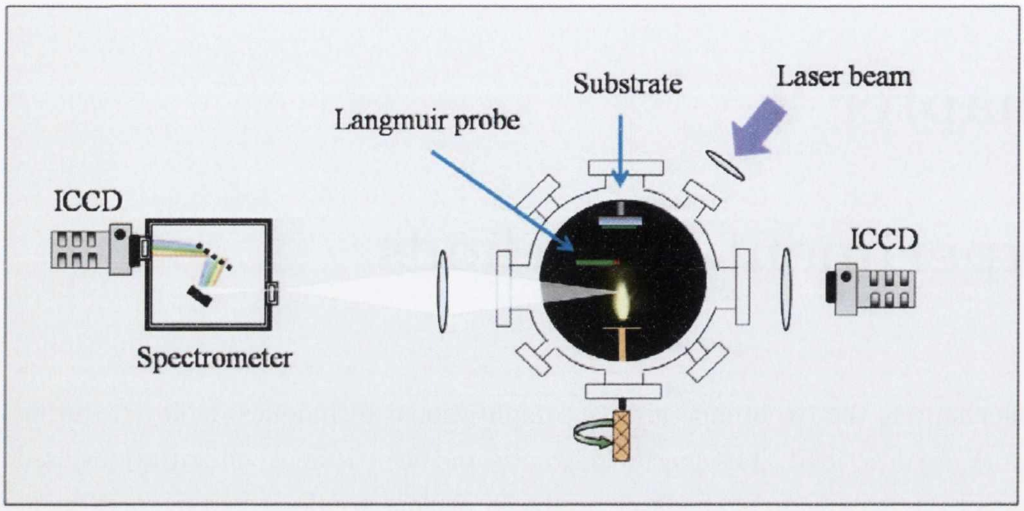

Figure 2.1: Schematic of the experimental setup.

performed using a Langmuir probe placed in the vacuum chamber in front of the expanding plume. The probe was connected to the oscilloscope via a biased (Koopman) circuit. The probe could be charged positively or negatively to measure an electron or ion current, respectively.

The light emitted by the excited ablated species at right angles with respect to the target surface normal was studied by means of two techniques: time resolved optical imaging (or fast photography) and time- and space-resolved optical emission spectrometry. The fast photography was done with an intensified charge coupled device (ICCD) with a minimum gate time of 2 ns. The ICCD provides two-dimensional snapshots of the plume expansion, allowing us to study the spatial and temporal expansion dynamics of the plume emission as a whole. For the emission spectrometry, the plume was imaged on the entrance slit of an Oriel MS260i imaging spectrometer coupled with an ICCD detector with a minimum gate time of 5 ns. In this way it was possible to simultaneously obtain information on both the spectral and spatial characteristics of the emitting species. A periscope was used to orient the plume image so that the direction corresponding to the target normal lay along the spectrometer slit. The entrance slit to the spectrometer was 3 $mm \times 50\ \mu m$ in dimension. A single converging lens was used to form a $\times 0.154$ demagnified image of the plume on the slit. Fig. 2.2 shows a schematic diagram of

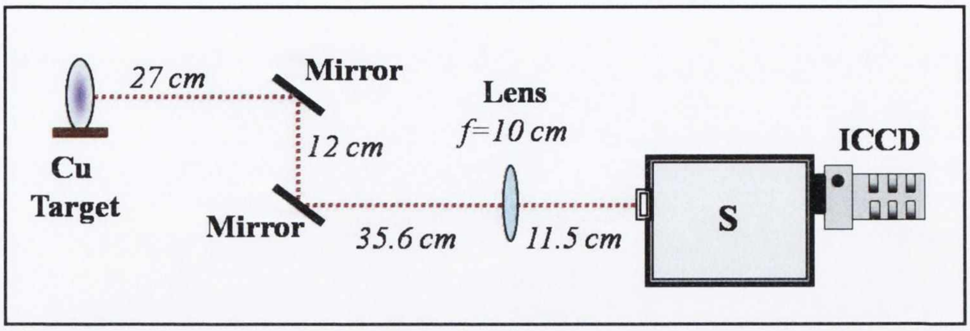

Figure 2.2: Schematic diagram of the optical system used to image the plume on the spectrometer slit. "S" indicates the spectrometer.

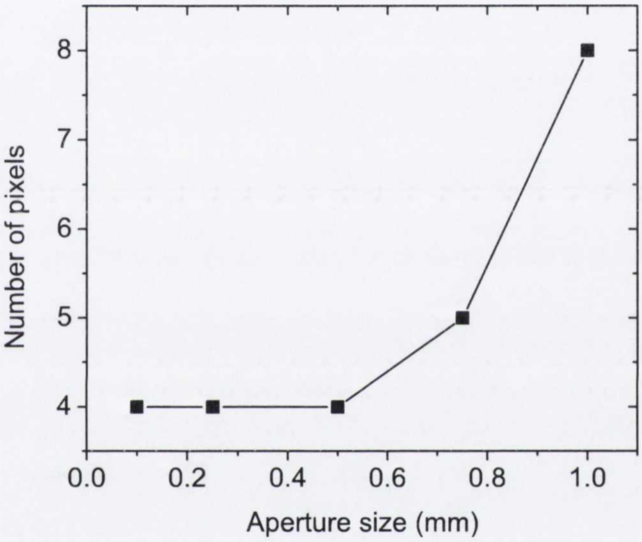

Figure 2.3: Number of pixels forming the aperture image on the ICCD sensor as function of the aperture size.

the optical system used to image the plume on the spectrometer slit. The imaging system in the spectrometer has a magnification of 1.6, giving a total magnification of 0.246.

The spatial resolution of the optical system was measured by imaging an aperture of known dimensions on to the spectrometer-ICCD system. The aperture was placed at the position of the plume axis and a quartz halogen lamp was used as back light. The dimension of the aperture was decreased from 1 *mm* to 0.1 *mm*. Fig. 2.3 shows the plot of the number of pixels forming the aperture image on to

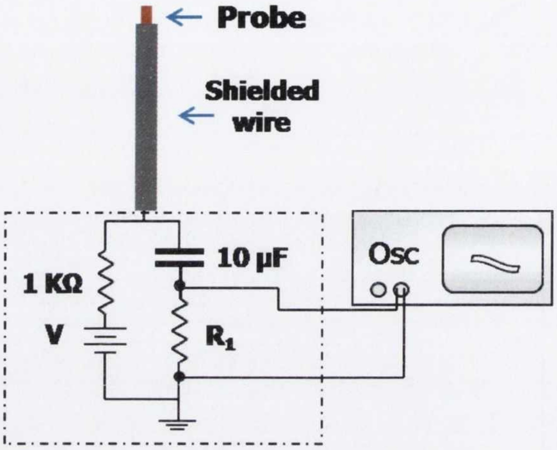

Figure 2.4: Schematic of the Langmuir probe biasing circuit.

the ICCD sensor as function of the aperture size. As it can be seen, the smallest feature the spectrometer can measure spatially is $\sim 0.5\ mm$.

The spectrometer was equipped with a 300 $lines/mm$ grating which gives a spectral resolution of 0.75 nm. The spectral range was $360 - 590\ nm$. Both the ICCDs used in this work were triggered to record the emission at various time delays after the laser pulse. At each time delay the background was acquired and subtracted from the corresponding emission signal.

Depositions were also recorded on glass substrates placed normal to the plasma expansion to investigate how the magnetic field influences the amount and spatial distribution of ablated material.

Finally, the mass ablated per pulse was measured. Keeping the target stationary, a small crater was formed in the target by firing multiple laser shots. The craters were scanned using a surface profiler and the ablation mass per pulse estimated.

2.2 Langmuir probe

The Langmuir probe is a diagnostic device used to study plume dynamics and plume expansion in a vacuum. The Langmuir probe technique is particularly well

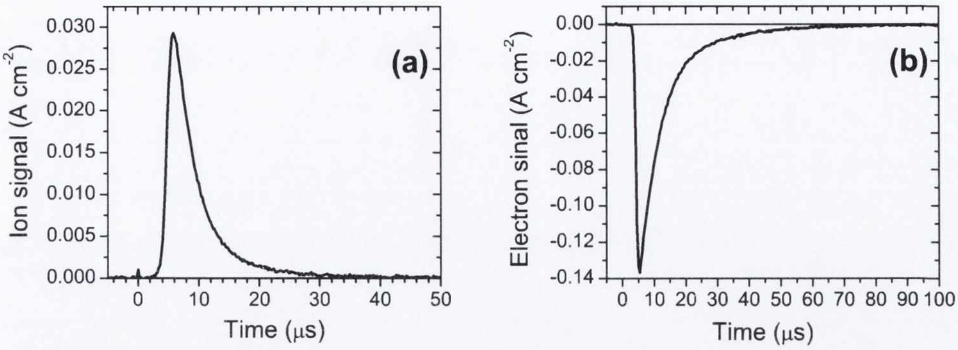

Figure 2.5: (a) Ion and (b) corresponding electron saturation current per unit area at 8 *cm* from the target for a 248 *nm* laser produced copper plasma expanding in vacuum.

suited to the measurement of a variety of plasma parameters including ion and electron density, electron temperature and ion kinetic energy. In spite of the relative simplicity of the experimental scheme, ion probes require a rather complicated theory to fully explain their current to voltage behaviour. The Langmuir probe theory has been described in detail by several authors [34, 59, 60, 61]. In the following section, some general properties of the Langmuir probe will be discussed.

The probe consists of a small metallic biased electrode inserted into the path of the plasma and connected externally to a power supply and an oscilloscope. In our experiment a planar probe of 2×2 mm^2 was used. The probe can be biased positively or negatively in order to record an electron or an ion signal respectively. The probe biasing circuit used is shown in Fig. 2.4. A 10 μF capacitor was chosen to ensure the correct working conditions for the probe, i.e. to ensure that the total charge collected by the probe is small compared to the charge on the capacitor. This prevents the capacitor discharging during the plasma transit.

Fig. 2.5(a) and (b) show, respectively, an ion and an electron current density acquired with the probe at 8 *cm* from the target for a 248 *nm* laser produced copper plasma expanding in vacuum. If the bias of the probe is increased from negative to positive voltages, by plotting the value of the measured current versus the applied voltage at a specific time, the current-voltage, I-V, characteristic is obtained. Fig. 2.6 shows the typical current-voltage curve obtained at a particular time in the expansion of the ablation plume. The I-V curve can be divided

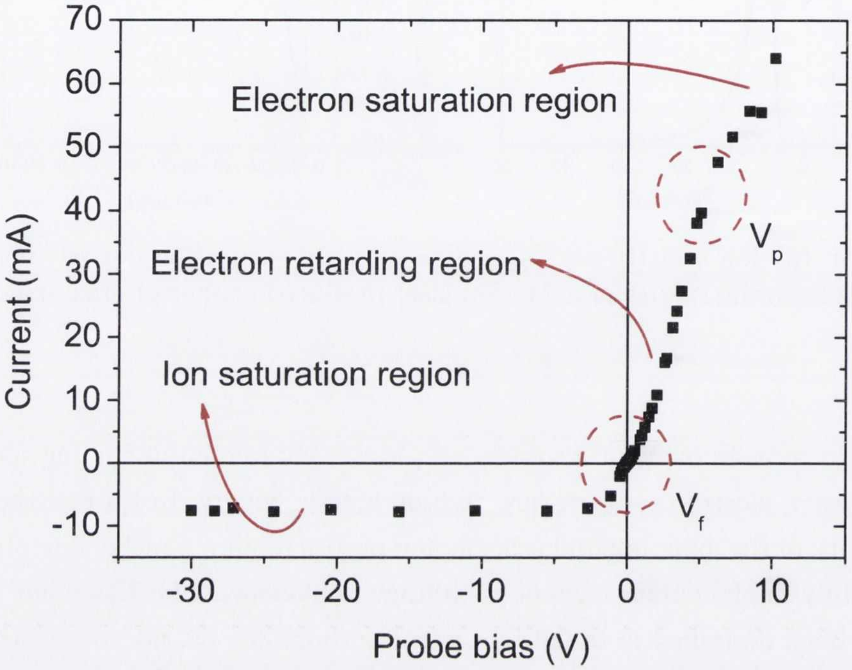

Figure 2.6: Typical I-V characteristic of the Langmuir probe [60].

in three regions. The first region is the ion saturation current region and all the measurements presented in this thesis were performed in this condition. For a planar probe facing the plasma flow, if the voltage is negative enough to prevent the electrons with the highest thermal energy from reaching the probe, the detected ionic current saturates. This current, $I_{i,sat}$, is related to the ion number density, n_i, by the relation:

$$I_{i,sat} = eA_p v_i \sum_j n_{i,j} Z_j \tag{2.1}$$

where $I_{i,sat}$ is the ion current collected from the probe, e is the electron charge, A_p is the probe area, v_i is the ion velocity and Z is the ionization state. If $Z = 1$ then:

$$I_{i,sat} = eA_p v_i n_i$$

An example of the ion saturation current per unit area is shown in Fig. 2.5(a). Increasing the bias of the probe from negative to positive the current due to electrons increases. When ion and electron current are equal the measured current is zero. The corresponding bias is the floating potential, V_f.

Further increase in the bias brings to the second region, called the electron retarding region. In this region the probe acts as an energy selector because it collects only the electrons that have enough kinetic energy to overcome the potential barrier. In this region the current is related to the electron energy distribution. For a Maxwellian distribution the electron current is given by:

$$I_e = I_{e,sat} exp\left(\frac{V - V_p}{kT_e}\right) \tag{2.2}$$

where T_e is the electron temperature, $I_{e,sat}$ is the saturation electron current and V_p is the plasma potential.

With further increase of the probe bias above V_p, the slope of the I-V curve changes and the saturation electron current region is reached. This is the region where the electron signals are normally measured. The measured current is given by:

$$I_{e,sat} = \frac{1}{4} e A_p v_e n_e \tag{2.3}$$

where n_e is the electron number density and v_e is the electron thermal velocity, which for a Maxwellian distribution is given by $\sqrt{(8kT_e/\pi m_e)}$. A typical electron signal is shown in Fig. 2.5(b). As can be seen, the electron current is much higher than the corresponding ion current. This can be seen by comparing equations (2.1) and (2.3): the ratio of the electron over the ion current is $I_e/I_i = v_e/4v_i$. From Fig. 2.5, v_i is about 1.4×10^6 $cm\ s^{-1}$, while, for a typical temperature of about 1 eV, $v_e \approx 6 \times 10^7$ $cm\ s^{-1}$. Hence the ratio I_e/I_i is of the order of 10.

2.2.1 Plasma parameters

The ion signal, detailed in Fig. 2.5(a), is characterized by a rapid rise in current indicating the arrival of the plasma front on the probe. It reaches a maximum, corresponding to the time of maximum ion flux and then decreases as the plasma continues to expand beyond the probe. From the ion signals, and using the equations (2.1) - (2.3) above, several plasma parameters can be extracted.

One of the easiest quantities to extract is the ion velocity. The Anisimov model [30] has shown that a laser produced plasma expanding in vacuum is initially ac-

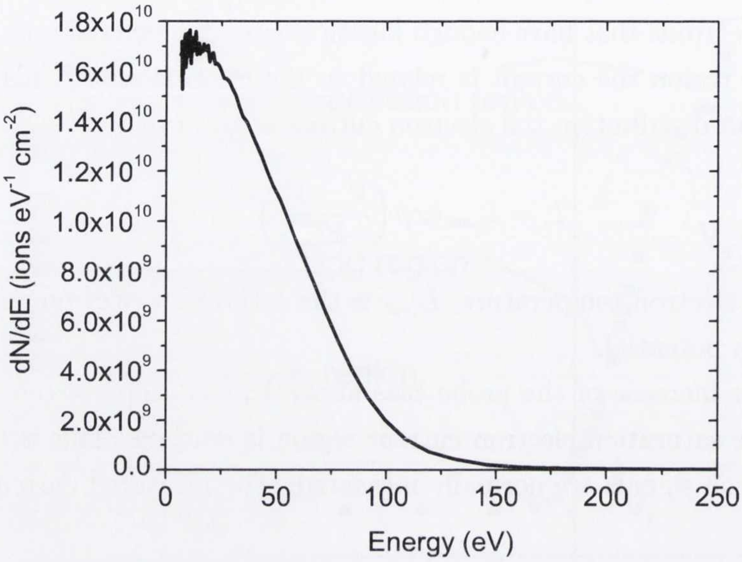

Figure 2.7: Ion energy distribution per unit area.

celerated and after about 100 ns (see Fig. 1.1) the expansion becomes inertial, the motion then is self-similar. Since the initial acceleration time is much shorter than the time of flight, the ion velocity can be considered constant in time and approximated by the target-probe distance, d_p, divided by the time of flight, t, found from the ion signal. For example, in Fig. 2.5(a), d_p was 8 cm and the time of maximum ion flux is 5.8 μs, which corresponds to an ion velocity of $1.4 \times 10^6\ cm\ s^{-1}$.

Also, the velocity and energy distributions can be inferred by using the following equations:

$$\frac{dN}{dv} = \frac{I_{i,sat}t^2}{eA_pd_p} \tag{2.4}$$

$$\frac{dN}{dE} = \frac{I_{i,sat}t^3}{em_iA_pd_p^2} \tag{2.5}$$

where dN/dv and dN/dE are the number of ions per velocity and energy interval, respectively, per unit area and m_i is the ion mass. As an example, the energy distribution corresponding to the ion signal in Fig. 2.5(a) is shown in Fig. 2.7.

An estimate of the ion yield, i.e. the total number of ions per unit area collected by the probe, can be obtained by integrating the probe signal in Fig. 2.5(a) and dividing by the electron charge. In the example of Fig. 2.5(a) the ion yield is

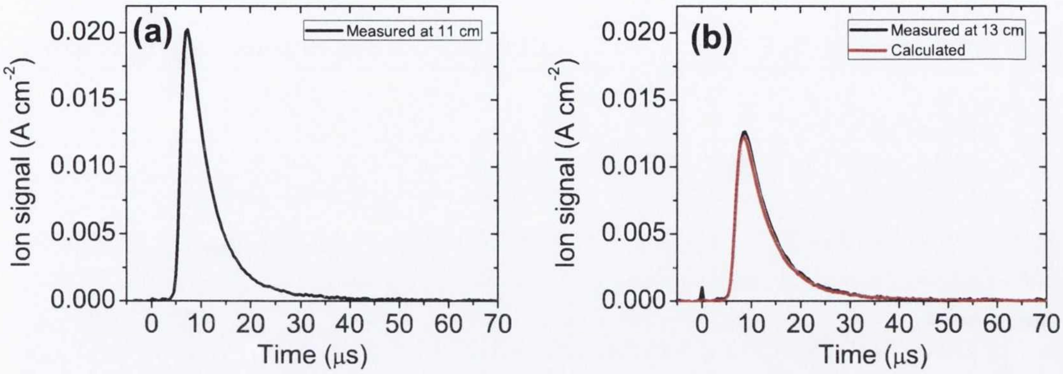

Figure 2.8: Ion saturation currents per unit area for a 248 *nm* laser produced copper plasma expanding in vacuum acquired with the Langmuir probe at (a) 11 *cm* and (b) 13 *cm* from the target. (b) Also shows the ion signal at 13 *cm* calculated from the ion signal in (a) using equation (2.6).

1.1×10^{12} *ions cm*$^{-2}$.

As a consequence of the self-similar expansion, it is possible to calculate the ion current at any distance from the target as a function of time or, for a given time, to extract the current as function of distance. The ion current decreases with the cube of the distance, d, through which the plasma has expanded. Hence if the ion signal $I_{i,1}$ was acquired placing the probe at a distance d_1 from the target, the ion signal $I_{i,2}$ at a different distance d_2 is given by:

$$I_{i,2} = I_{i,1} \left(\frac{d_1}{d_2} \right)^3 \tag{2.6}$$

and, because the plasma is assumed to expand at constant velocity, the time should be scaled as:

$$t_2 = t_1 \frac{d_2}{d_1} \tag{2.7}$$

As an example, Fig. 2.8(a) and (b) show the ion signals acquired with a Langmuir probe at 11 *cm* and 13 *cm* from the target, respectively. The ion signal measured at 13 *cm* is compared with the one calculated from the signal in Fig. 2.8(a) using the above relations. As can be seen both the shape and the intensity of the probe signal is in a good agreement with the calculations. To derive instead the dependence of the ion current on the distance, time can be transformed into

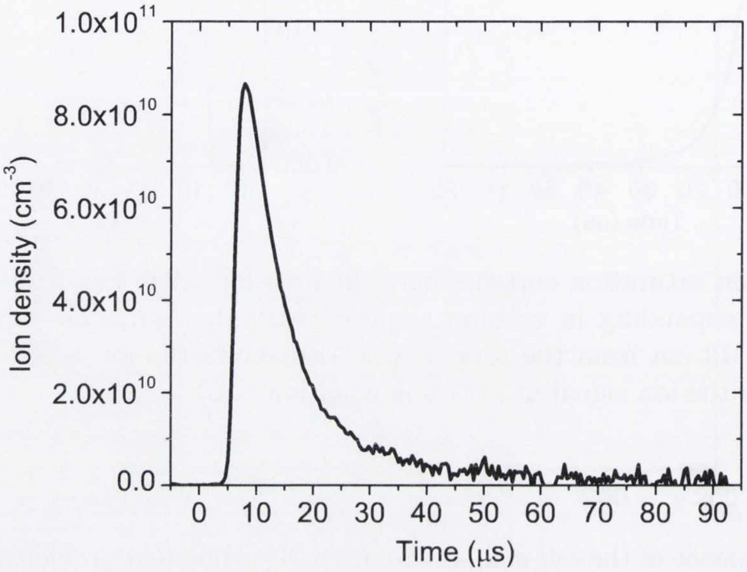

Figure 2.9: Ion density calculated from the Langmuir probe signal in Fig. 2.8(a)

distance with the following relation:

$$d' = d_1 \frac{t'}{t_1} \tag{2.8}$$

where d_1 and t_1 are the distance and the time at the probe and *t'* is an arbitrary time associated with the distance *d'*. Hence the current *I'* as a function of the distance from the target *d'* at a given time *t'* is expressed by:

$$I' = I_1 \left(\frac{t_1}{t'} \right)^3 \tag{2.9}$$

Using equation 2.1, the ion density can also be estimated from the ion signal. For *Z=1*, the ion density at the probe position is:

$$n_i(t) = \frac{I_i(t)}{eA_p v}$$

Fig. 2.9 shows the density calculated from the ion signal in Fig. 2.8(a). Furthermore, given the above relation between *I* and *n*, from 2.6 - 2.9, the corresponding den-

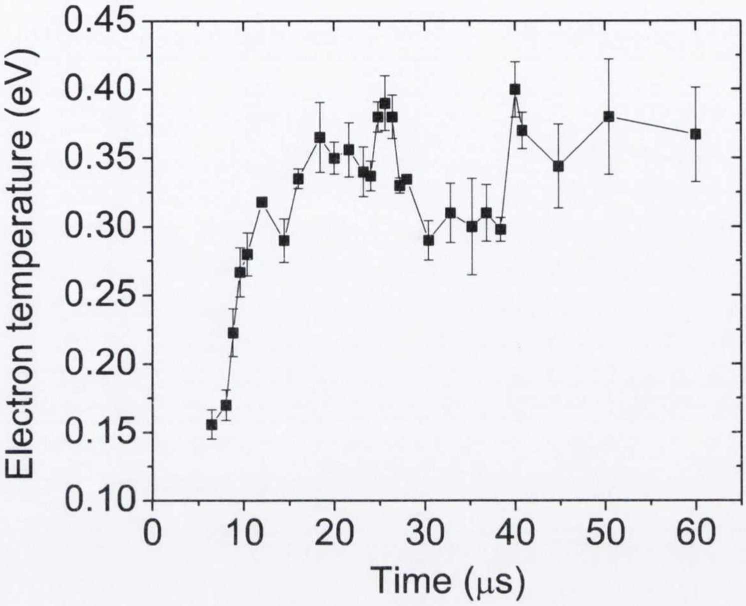

Figure 2.10: Electron temperature at 10 *cm* from the target.

sities n_2 and n' can be inferred.

Finally, from measurements of the electron current at different probe bias, the electron temperature, T_e, can be estimated. Using equation (2.2), T_e can be derived by evaluating the slope of the I-V characteristic in the electron retarding region. At this point, it is worth noticing that in this region, the probe has a positive bias of $1 - 3$ V - see Fig. 2.6. However, typically the ions have energy of $10 - 200$ eV, as shown in Fig. 2.7. Ions in this range of energy can still reach the probe even when $1 - 3$ V are applied making the correct interpretation of the electron signals difficult. Doggett et al. [60] have studied the effect of the probe orientation with respect to the plasma flow. They have shown that with a probe oriented parallel to the flow, the ion current due to the plasma flow is eliminated, giving a more reliable measurement of T_e. As an example, Fig. 2.10 shows the temporal variation of T_e measured at 10 *cm* from the target (this data will be discussed in more detail in Chapter 6). The initial rise in temperature is consistent with the assumption in the Anisimov model that the expansion is adiabatic and isentropic [31].

2.3 Spectrometer calibration

Wavelength and sensitivity calibrations of the spectrometer were performed in order to ensure a correct analysis of the data acquired. The wavelength calibration assures a correct identification of the emitting species. It was performed using an Hg spectral lamp and the calibration was corroborated using a helium-neon laser.

Each element in the light collection system has wavelength dependent characteristics and this needs to be taken into account in finding the emission spectrum of the plasma. The light emitted by the plasma is imaged by a system of mirrors and lenses on the entrance slit of the spectrometer. Here it is diffracted by the grating and delivered on the ICCD sensor area. Each pixel on the ICCD produces as response a certain number of counts. The counts are a measurement of the number of photons emitted by the source that reach the active area of the ICCD sensor. Indeed, the number of counts read from a single pixel depends on the gain, the gate time and the number of accumulations used to acquire the spectra. The sensitivity calibration allows us to measure the absolute spectral energy distribution of the emission. In particular it allows us to define a function, $F(\lambda)$, that accounts for all the losses or changes in the spectral energy distribution that occurred due to the light collection system. An Oriel 6333 100 W quartz halogen lamp was used, for the sensitivity calibration. This lamp produces a uniform flux density over an area of 2.5 *cm* × 2.5 *cm* at a plane 50 *cm* from the lamp. For this reason the lamp was positioned at 50 *cm* from the plasma plane. The calibration function $F(\lambda)$ was found from the lamp counts, C_L, measured from the ICCD:

$$C_L(\lambda) = F(\lambda) \cdot I_L(\lambda) \cdot n_{L1} \cdot n_{L2} \cdot t_L \tag{2.10}$$

where n_{L1} and n_{L2} are, respectively, the number of acquisitions and the number of pixels binned for each measurement of the lamp emission, t_L is the gate time used for the measurement and $I_L(\lambda)$ is the spectral irradiance of the lamp. It should be noted here that all the light emitted from the plane at 50 *cm* from the lamp is collected into the spectrometer (this will be shown below). For this reason in the above relation, C_L can be expressed in terms of the irradiance and not as radiance times the solid angle. The spectral irradiance of the lamp at the plane at 50 *cm*

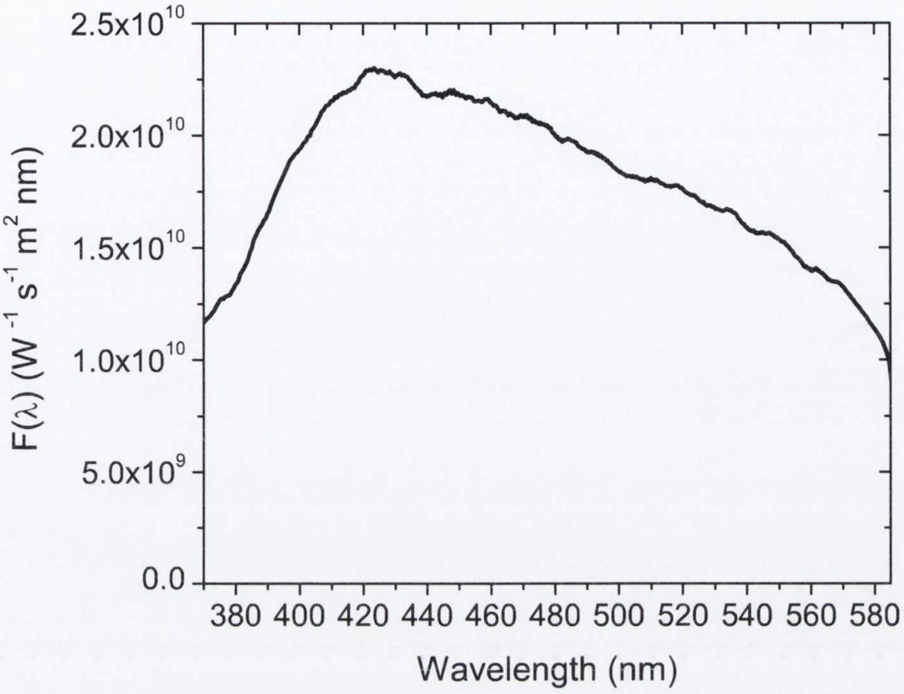

Figure 2.11: Calibration function, $F(\lambda)$, obtained using equation (2.12).

can be expressed by the black body irradiance equation:

$$I_L(\lambda) = A_{fit}10^{-9}\frac{2\pi hc^2}{\lambda^5}\left[\left(exp\frac{hc}{\lambda kT} - 1\right)\right]^{-1} [Wm^{-2}nm^{-1}] \tag{2.11}$$

where A_{fit} is a fitting constant and λ is the wavelength in meters. The temperature T and A_{fit} were found from the fit of equation (2.11) with the spectral irradiance tabulated from the Oriel lamp manufacturer. The values found are: $A_{fit} = (7.64 \pm 1.118) \times 10^{-6}$ and $T = (3226.74 \pm 64)\ K$. Rearranging relation (2.10), it is possible to obtain the calibration function, $F(\lambda)$:

$$F(\lambda) = \frac{C_L}{I_L \cdot n_{L1} \cdot n_{L2} \cdot t_L} \tag{2.12}$$

$F(\lambda)$ is shown in Fig. 2.11. Relation (2.10) can be written for the plasma counts measured, C_p:

$$C_p = F(\lambda) \cdot R_p(\lambda) \cdot \Omega \cdot n_{p1} \cdot n_{p2} \cdot t_p \tag{2.13}$$

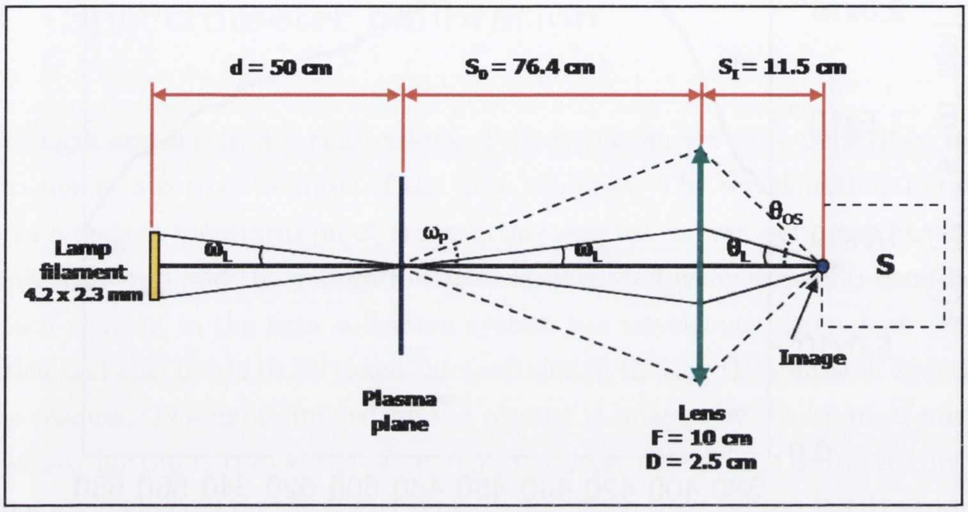

Figure 2.12: Schematic of the optical system used to image the plasma plume on to the entrance slit of the spectrometer. $\omega_L = 0.24°$; $\theta_L = 1.6°$; $\omega_p = 0.96°$ and $\theta_{OS} = 6.22°$. D and F indicates the lens diameter and the focal length, respectively.

where $R_p(\lambda)$ is the spectral radiance of the plasma and Ω is the solid angle subtended by the optical system. Rearranging expression (2.13) to calculate the plasma spectral radiance $R_p(\lambda)$ and accounting for (2.12), we obtain the relation:

$$R_p(\lambda) = \frac{C_p(\lambda)}{F(\lambda) \cdot n_{p1} \cdot n_{p2} \cdot t_p \cdot \Omega} = \frac{C_p(\lambda) \cdot I_L(\lambda) \cdot n_{L1} \cdot n_{L2} \cdot t_L}{C_L \cdot n_{p1} \cdot n_{p2} \cdot t_p \cdot \Omega} [Wm^{-2}nm^{-1}sr^{-1}] \tag{2.14}$$

To ensure that all the light collected by the delivery lens is sent in to the spectrometer, the solid angle, Ω, subtended by the optical system should be $\leq$ the acceptance angle of the spectrometer. Fig. 2.12 shows a schematic of the equivalent optical system used here; because the lens and the mirrors have the same diameter ($D = 2.5\ cm$), the mirrors do not limit the light collected by the lens so they have not been shown in the figure. The spectrometer has an acceptance cone with half angle of 7.4°. In this work, the half-angle impinging on the spectrometer slit after the light collection system, θ_{OS}, was 6.22° which is smaller than the acceptance angle of the spectrometer. The solid angle Ω in equation (2.13) is then $8.82 \times 10^{-4}\ sr$. Moreover, as shown in Fig. 2.12, the angle

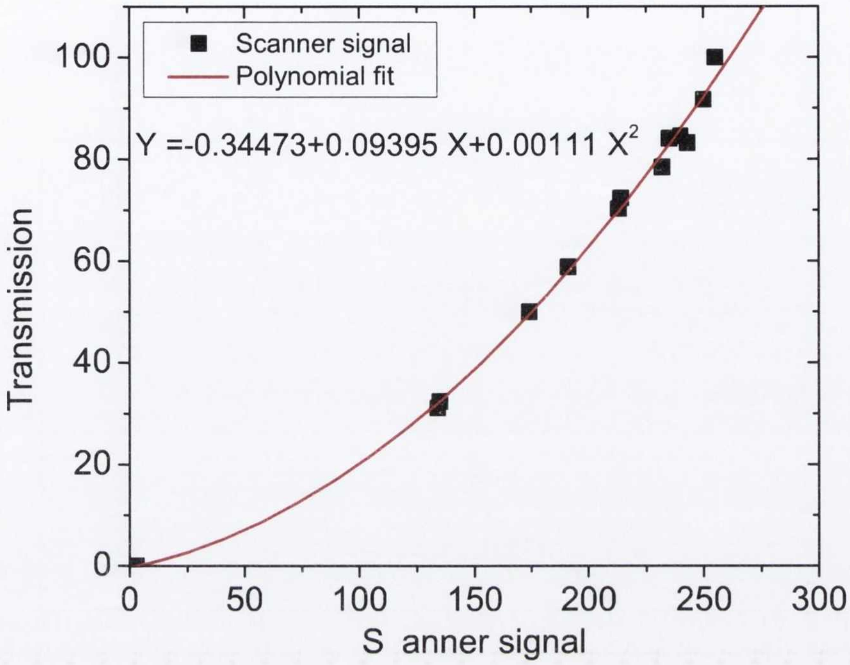

Figure 2.13: Calibration curve for the optical transmission scanner to convert scanner signal to film transmission. The squares correspond to the scanner signals acquired with the different neutral density filters. A second order polynomial fit is shown in red and the equation is given in the plot.

subtended by the lamp, is $\theta_L = 1.6°$, which is smaller than the acceptance angle of the spectrometer. As already mentioned above this means that all the light emitted by the lamp leaving the plasma plane is collected into the spectrometer.

2.4 Thin film depositions

As mentioned above, depositions were made on glass substrates placed at a fixed position normal to the plasma expansion. The thickness profile of the deposited material was found by measuring the optical transmission, around 515 *nm*, of the film with a calibrated flatbed scanner, Epson Perfection V700 PHOTO, 6400 dpi. The scanner was calibrated for transmission using a set of neutral density filters. In this way it was possible to associate an equivalent transmission to the scanner signal. The calibration curve is shown in Fig. 2.13. Fig. 2.14 schematically shows

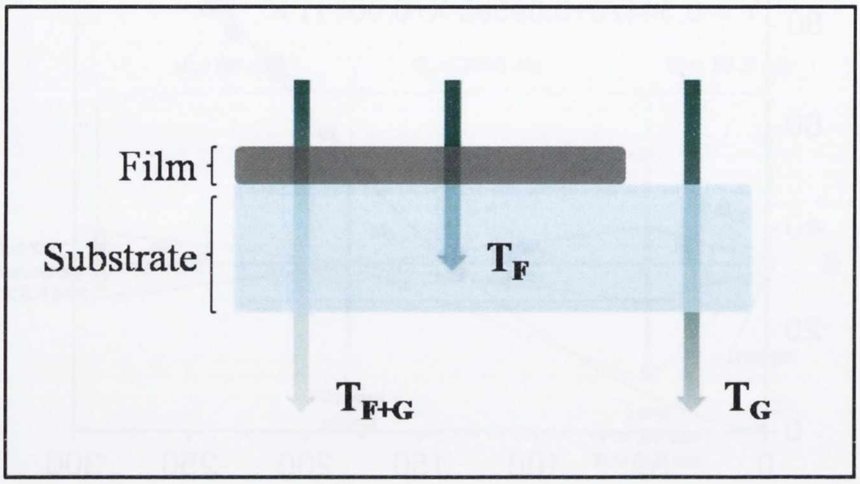

Figure 2.14: Schematic of a coated substrate. In this figure the formalism used for the analysis of the depositions is indicated.

the formalism used in the analysis of the depositions. The scanner was used to measure the transmission of the coated substrate, T_{F+G}, and the transmission of a bare substrate, T_G. The ratio $T = T_{F+G}/T_G$ was then found. Since the glass substrate is transparent, $T_G = T_B^2$, where T_B is the transmission across each bare glass interface. Thus

$$T = \frac{T_{F+G}}{T_G} = \frac{T_F T_B}{T_B^2} = \frac{T_F}{T_B}$$

where T_F is the transmission through the film into the glass. T_F/T_B is the transmission of the film normalized to the transmission of a bare glass interface.

The film thickness was found by comparing the measured transmission with a calculation from the XOP IMD program [62] and assuming the bulk values for the complex refractive index. Using this software the normalized transmission $\tilde{T} = \tilde{T_F}/\tilde{T_B}$ through the film into the glass was calculated as a function of the film thickness (the tilde indicates the calculated transmissions). Then from the measured transmission, T, the film thickness may be deduced. As an example, Fig. 2.15 shows $\tilde{T}$ as a function of the film thickness calculated for a copper film. The transmission decreases exponentially with the thickness, as:

$$\tilde{T} = \frac{\tilde{T_F}}{\tilde{T_B}} = A \cdot exp(-d/B) + C \tag{2.15}$$

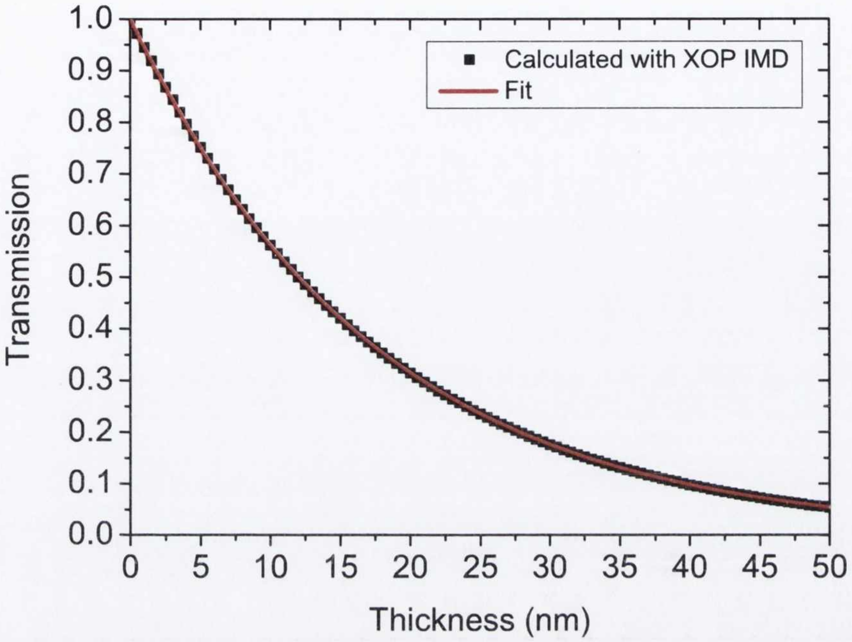

Figure 2.15: Transmission as a function of copper thickness calculated with XOP IMD software.

where d is the thickness of the film, A, B and C are fitting parameters which can be found from the fit of equation (2.15) with the calculated transmission. The values found are: $A = 1.00473 \pm 0.0017$; $B = 17.37037 \pm 0.00926$ and $C = -0.00259 \pm 0.0017$. Hence the thickness profile is give by:

$$d = -17.37037\, ln\left(\frac{T + 0.0259}{1.00473}\right) \tag{2.16}$$

Equation (2.16) can then be used to convert the measured transmission into thickness.

Chapter 3

Plasma expanding across a nearly uniform magnetic field

This chapter examines the expansion of a copper laser produced plasma across a nearly uniform magnetic field. The aim of this experiment was to restrain the forward expansion of the plasma. The main diagnostic technique used for this experiment was time- and space-resolved optical emission spectroscopy. Ion time-of-flight Langmuir probe measurements were used to characterize the plume expansion in the absence of the magnetic field. The experimental setup and the results are discussed below.

3.1 Experimental setup

The magnetic field was generated using two ring-shaped Nd–Fe–B magnets attached to an iron yoke as shown in Fig. 3.1. Each magnet had the following dimensions: external diameter: 45 mm, hole diameter: 15 mm and height: 20 mm. The separation of the magnets was set at 35 mm to produce a relatively uniform field of 320 mT in the region between the magnets and to provide a sufficient expansion space for the laser ablation plume.

The design of the magnetic geometry used here was obtained with the COMSOL MULTIPHYSICS computer code [63]. Fig. 3.2 shows the calculated magnetic field. The field was also measured using a Hall probe. Fig. 3.2(b) and (c) show the

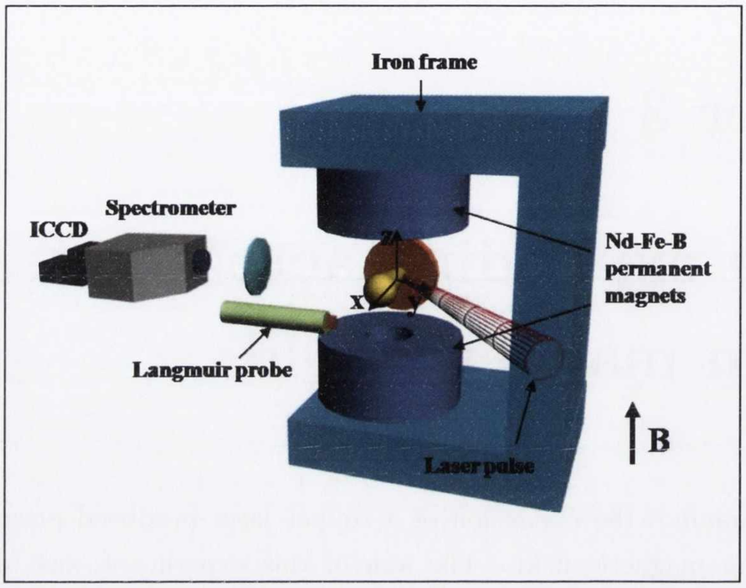

Figure 3.1: Schematic of the experimental setup.

comparison of the magnetic field profile measured and calculated with COMSOL. As can be seen there is a very good agreement between the calculations and the measurements of the field produced.

As shown in Fig. 3.1, the origin of the coordinate system is on the axis of the system and midway between the magnets. The magnetic field is directed along the z axis. The copper (Cu) laser ablation target was placed between the magnets with the surface of the target coincident with the edge of the hole in each of the magnets ($x = -0.75\ mm$). In this way it was ensured that the ablation plume could expand into a region where the transverse field is nearly uniform.

The laser source was a Nd:YAG laser with 6 *ns* pulse width and a wavelength of 1064 *nm*. The Cu target was irradiated by the laser beam in a stainless steel vacuum chamber and it was rotated to reduce drilling. The angle of incidence of the laser was 45° and the laser was focused to a slightly elliptical spot of radii $R_0 = 0.65\ mm$ and $r_0 = 0.49\ mm$, giving an area of 0.009 cm^2. Thus the average laser fluence was 5.2 Jcm^{-2}.

A planar Langmuir ion probe of dimensions $3.28 \times 2.08\ mm^2$ was used to characterize the plasma plume expansion in the absence of the magnetic field. The probe was positioned at 10 *cm* directly in front of the ablation spot and oriented

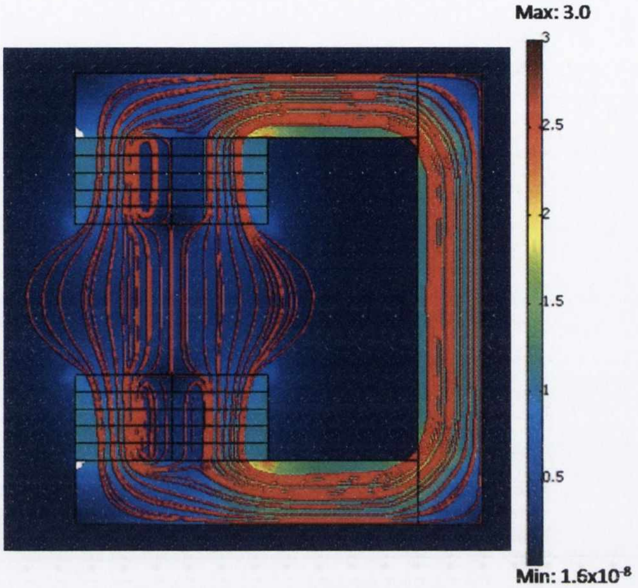

(a)

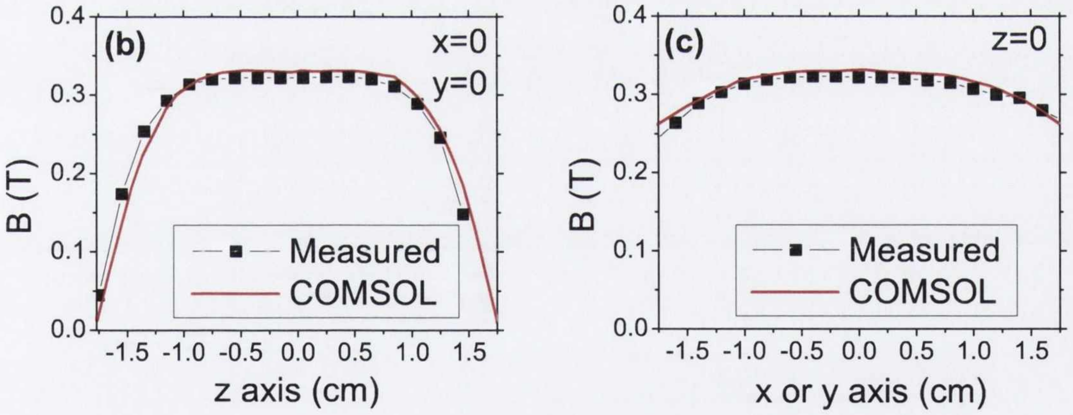

Figure 3.2: (a) Calculated magnetic field lines. The color scale indicates the magnetic field strength in T. (b) and (c) comparison of measured and calculated magnetic field profiles.

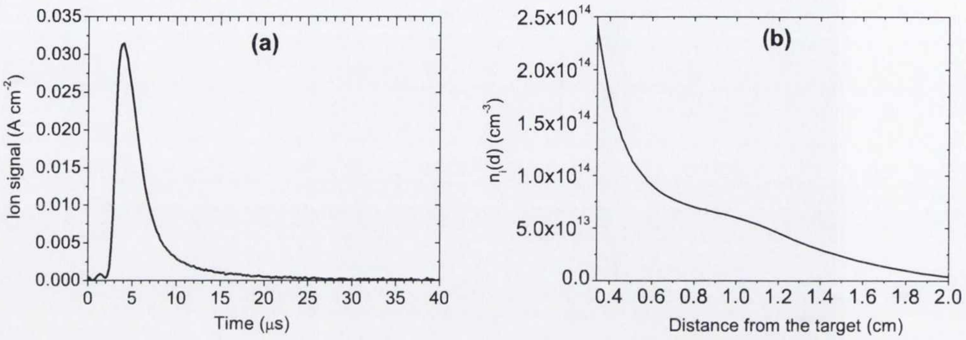

Figure 3.3: (a) Ion TOF signal taken with Langmuir probe at 10 cm from the target, at a laser fluence of 5.2 Jcm^{-2}; (b) corresponding ion density profile at 600 ns as a function of the distance from the target.

to face the plasma flow. The probe was biased at $-30\ V$.

Time- and space-resolved optical emission spectroscopy was carried out to study the effect of the magnetic field on the plasma expansion dynamics. The plasma was viewed from the side (in the y-direction) and imaged directly into the entrance slit of the spectrometer coupled with the ICCD. The optical system used here was described in detail in Chapter 2. Wavelength and sensitivity calibrations of the spectrometer were performed to facilitate quantitative spectroscopic analysis.

The set of measurements presented herein were repeated several times and they were found to be reproducible.

3.2 Langmuir ion probe measurements

Fig. 3.3(a) shows the ion current per unit area recorded on the Langmuir ion probe, without the magnetic field. As discussed in Section 2.2, in a vacuum environment, without magnetic field, the ion flux measured can be understood in terms of the adiabatic, isentropic expansion model developed by Anisimov et al. [30]. At the end of the laser pulse the ablated material exists as a thin layer of plasma on the target surface. The steep density gradients give rise to rapid acceleration. After

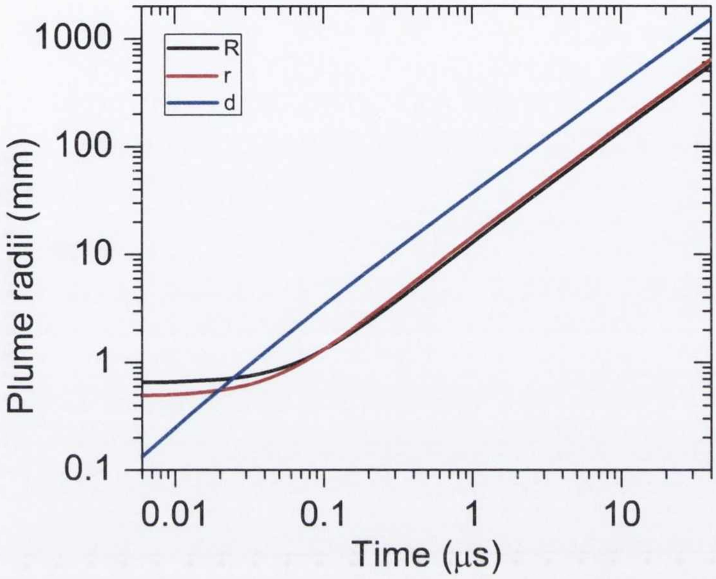

Figure 3.4: Evolution of the plume radii as a function of time calculated using the Anisimov model.

a short distance, *d'*, the plume acceleration is complete and the semi-ellipsoidal plume expands inertially while remaining self-similar. Fig. 3.4 shows the evolution of the plume radii, R, r and d, as a function of time calculated from the Anisimov model discussed in Section 1.1.2. The initial plasma conditions used for the calculations were: $R_0 = 0.65\ mm$, $r_0 = 0.49\ mm$, $d_0 = 20\ \mu m$, $\gamma = 1.25$, $E = 49\ eV$ and M= atomic mass of copper= $10.55 \times 10^{-26} kg$. R_0 and r_0 are the dimensions in the plane of the target and d_0 is the thickness at the end of the laser pulse. It can be seen that the plume expansion becomes inertial after $\sim 100\ ns$, which corresponds to a distance *d'* of $\sim 3.4\ mm$. Since the target-probe distance, $d_p = 10\ cm$, is much larger than *d'*, the plasma flow at the probe position is inertial and the ion flow velocity is to a good approximation given by the probe distance divided by the ion TOF measured from the time of laser irradiation. The TOF at the maximum ion flux is $4\,\mu s$, which corresponds to an ion velocity of $2.5 \times 10^6\ cms^{-1}$ and ion energy of 206 eV. The ion yield is about $8 \times 10^{11}\ ions\ cm^{-2}$.

Since the expansion is self-similar, the ion probe signal in Fig. 3.3(a) can also be used to infer the plasma density profile at any distance from the target as a function of time, otherwise, for a given time, to extract the density as a function of the distance. According to equations (2.1) and (2.6)-(2.8), the ion density at a given time, t_0, as function of the distance, d, is given by:

$$n_i(d, t_0) = n_p(d_p, t_p) \left(\frac{t_p}{t_0}\right)^3 \tag{3.1}$$

and d is:

$$d = d_p \frac{t_0}{t_p} \tag{3.2}$$

where n_p is the ion density measured by placing the probe at a distance d_p from the target and having temporal profile t_p. As an example, Fig. 3.3(b) shows the ion density at $t_0 = 600\ ns$ as a function of the distance calculated from the ion probe signal in Fig. 3.3(a). It can be seen that the density profile at 600 ns has two components: one at a few millimetres ($\leq 3\ mm$) from the target surface and the other at 9 mm. These two components can be associated with the differential expansion of singly and doubly ionized copper, respectively and will be discussed in more detail below.

3.3 Spectroscopic measurements

Fig. 3.5 shows a comparison of space-resolved spectra for free ablation (without a magnetic field) and with a magnetic field for a range of time delays after the laser pulse. For each image acquired, the gate width on the ICCD and the gain setting on the intensifier were kept constant (the gate width was 50 ns). From the images it is possible to follow the expansion of the plume from the target surface (zero position in each of the images) as a function of time and resolved in wavelength. At a few nanoseconds after the laser pulse the emission is a continuum with a maximum at about 440 nm. This continuum emission is mainly due to Stark broadening of the spectral lines, as discussed in Section 1.3.4. At late times as the plasma expands away from the target, spectral lines emerge from the continuum, very broad at first, but getting narrower at later times. After longer time delays

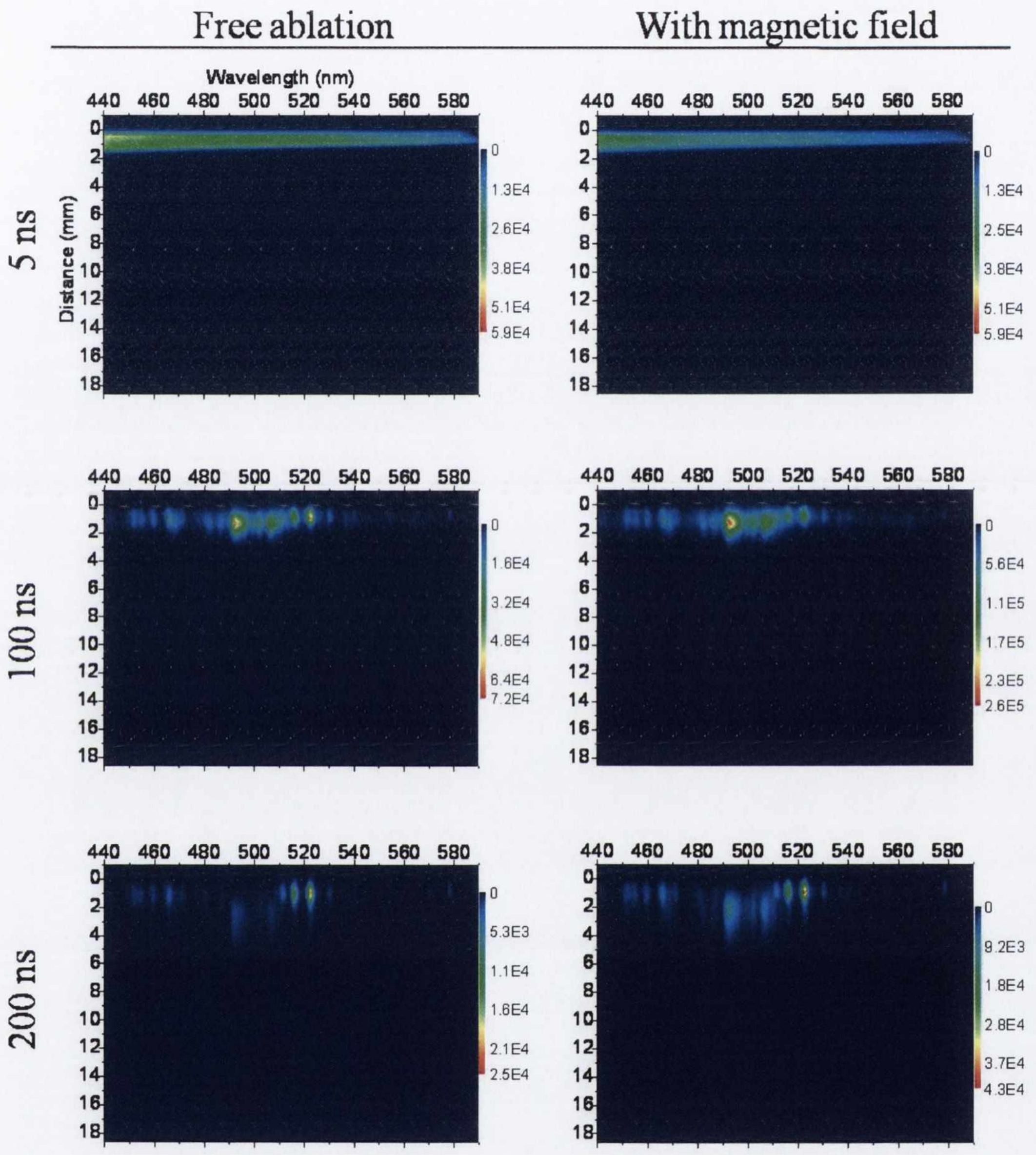
Free ablation
With magnetic field
Wavelength (nm)
440 460 480 500 520 540 560 580
Distance (mm)
0 2 4 6 8 10 12 14 16 18
5 ns
0 1.3E4 2.6E4 3.8E4 5.1E4 5.9E4
0 1.3E4 2.5E4 3.8E4 5.1E4 5.9E4
100 ns
0 1.6E4 3.2E4 4.8E4 6.4E4 7.2E4
0 5.6E4 1.1E5 1.7E5 2.3E5 2.6E5
200 ns
0 5.3E3 1.1E4 1.6E4 2.1E4 2.5E4
0 9.2E3 1.8E4 2.8E4 3.7E4 4.3E4

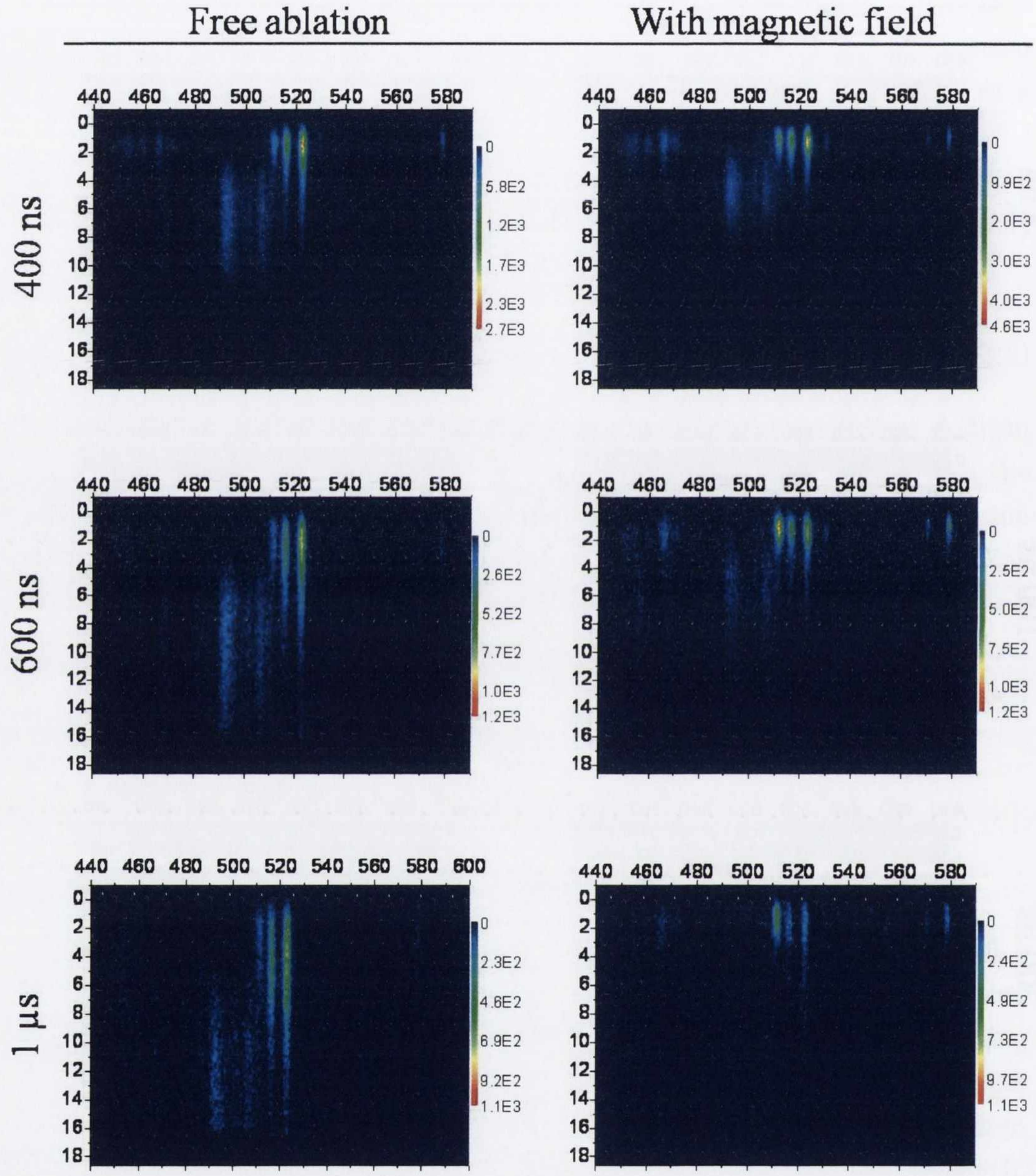

Figure 3.5: Space-resolved spectra of the Cu ablation plume for various time delays without and with magnetic field. All the images were acquired with the same gate width of 50 *ns* and same gain. The images are background corrected. The wavelength and space units are *nm* and *mm*, respectively, for all the images.

λ (nm)	*Lower level*	*Upper level*	E_l (eV)	E_u (eV)	g_l	g_u	A_{ul} (s^{-1})
402.26	$3d^{10}4p\ ^2P_{1/2}$	$3d^{10}5d\ ^2D_{3/2}$	3.78	6.87	2	4	1.90×10^7
406.26	$3d^{10}4p\ ^2P_{3/2}$	$3d^{10}5d\ ^2D_{5/2}$	3.82	6.87	4	6	2.10×10^7
427.51	$3d^9 4s\, 4p\ ^4P_{5/2}$	$3d^9 4s\, 5s\ ^4D_{7/2}$	4.84	7.74	6	8	3.45×10^7
510.55	$3d^9 4s^2\ ^2D_{5/2}$	$3d^{10}4p\ ^2P_{3/2}$	1.39	3.82	6	4	2.00×10^6
515.32	$3d^{10}4p\ ^2P_{1/2}$	$3d^{10}4d\ ^2D_{3/2}$	3.78	6.191	2	4	6.00×10^7
521.82	$3d^{10}4p\ ^2P_{3/2}$	$3d^{10}4d\ ^2D_{5/2}$	3.82	6.192	4	6	7.50×10^7
522.15	$3d^{10}4p\ ^2P_{3/2}$	$3d^{10}4d\ ^2D_{3/2}$	3.82	6.191	4	4	1.50×10^7
529.252	$3d^9 4s\, 4p\ ^4D_{7/2}$	$3d^9 4s\, 5s\ ^4D_{7/2}$	5.39	7.74	8	8	1.09×10^7
570.024	$3d^9 4s^2\ ^2D_{3/2}$	$3d^{10}4p\ ^2P_{3/2}$	1.64	3.82	4	4	2.40×10^5
578.213	$3d^9 4s^2\ ^2D_{3/2}$	$3d^{10}4p\ ^2P_{1/2}$	1.64	3.78	4	2	1.65×10^6

Table 3.1: Main observed Cu I transitions. E_l and E_u, g_l and g_u are energies and degeneracies of the lower and upper levels, respectively, and A_{ul} is the transition probability. These values are taken from [64].

the line intensities decrease, mainly due to the decreasing plasma density.

In the spectral region shown in Fig. 3.5 the spectral lines observed include neutral (Cu I) and singly ionised (Cu II) copper. These lines are identified in Fig. 3.6. There is a spectral feature near 491 *nm* which is due to several $3d^94f - 3d^94d$ Cu II overlapping lines. The other 3 main lines are due to neutral Cu and have been identified as Cu $3d^94s^2\ ^2D_{5/2} - 3d^{10}4p\ ^2P_{3/2}$ (510.69 nm), Cu $3d^{10}4p\ ^2P_{1/2} - 3d^{10}4d\ ^2D_{3/2}$ (515.32 *nm*) and Cu $3d^{10}4p\ ^2P_{3/2} - 3d^{10}4d\ ^2D_{3/2,5/2}$ (522.15 *nm*, 521.81 *nm*). The wavelengths for these lines are taken from [64] and from the the National Institute of Standards and Technology (NIST) tabulation [65]. An abbreviated Grotrian diagram for the main transitions of neutral Cu was already shown in the first chapter (Fig. 1.12) and it is reproduced here for convenience - Fig. 3.7. More details are given in Table 3.1, which lists the main observed Cu I transitions and the corresponding values of lower and upper-level energy, state degeneracy and transition probability [64].

From Fig. 3.5 it can be seen that in both cases, without and with magnetic field, the neutral and singly ionized line emissions are emitted from regions which are nearly spatially distinct, with the ionized emission localized further from the

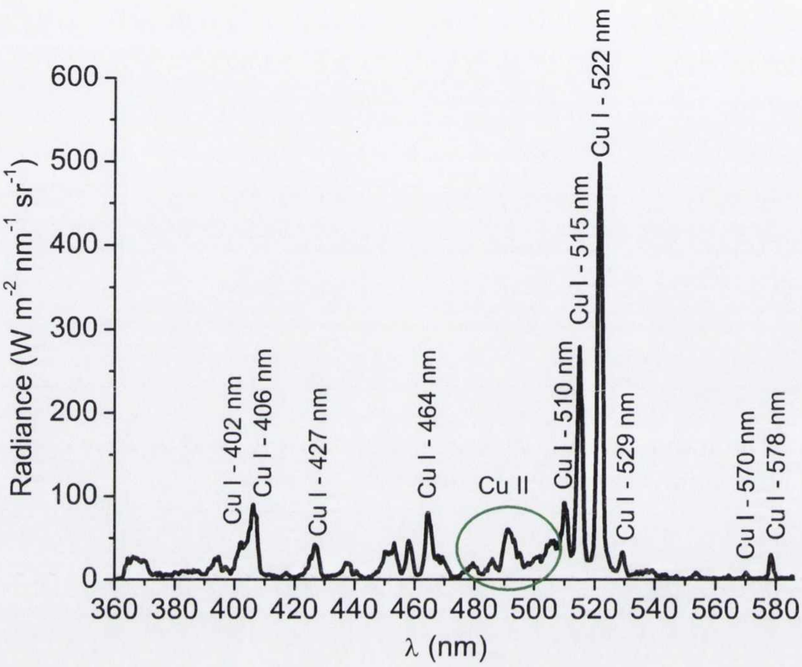

Figure 3.6: Spectral lines identification. Free ablation spectrum at 2 *mm* from the target and at 250 *ns* after the laser pulse.

target. The spectral emission from more ionized species occurring closer to the leading edge of the ablation plume is a widely observed feature of laser ablation and has also been observed for femtosecond laser ablation of Cu [66]. The origin of this is related to mechanisms of plasma formation and in particular to the absorption of the laser energy in the vapor-plasma. As mentioned in Section 1.1.1, the absorbed laser energy determines density, temperature and consequently ionization state of the plasma. The dominance of different ions in different regions of the ablation plume is due to spatial variation of both plasma temperature and density. The plasma front is the part that has the strongest interaction with the laser pulse and hence it is likely to be the most ionized.

Fig. 3.8 and 3.9 show the comparison of lineouts of the spectra with and without B-field at 200 and 600 *ns*, respectively, for three different distances from the target: 1 *mm*, 2 *mm* and 3 *mm*. These spectra were obtained from the images

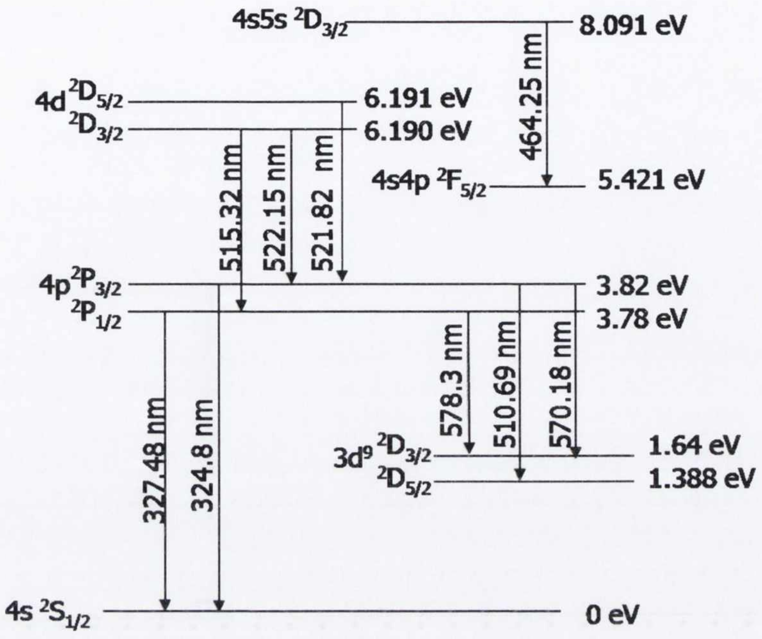

Figure 3.7: Abbreviated Grotrian diagram of neutral copper. The ionization energy is about 7.7 *eV*.

taken at 200 and 600 *ns* and shown in Fig. 3.5. The spectra have been absolutely calibrated following the procedure described in Section 2.3. From the spectral images and the lineouts, it can be clearly seen that at an early time, 0 – 400 *ns*, the main difference between the spectra without and with magnetic field is that the intensity of both neutral and ionic lines with magnetic field is higher than for the free ablation. At 400 – 600 *ns* the spatial profiles of the various lines become strikingly different in the presence of the magnetic field. The neutral and the ionic line emission is confined to a region much closer to the target. There is also a very marked change in the relative intensities of the neutral lines. Specifically, there is a strong increase in the relative intensity of the lines at 510, 570 and 578 *nm*. As an example, in Fig. 3.9(a) it can be seen that in the presence of the magnetic field, the 510 *nm* line is the most intense line of the spectrum.

These features can be seen more clearly in Fig. 3.10. They detail the spatial intensity profiles of the ionic lines (at around 491 *nm*) and the three neutral lines

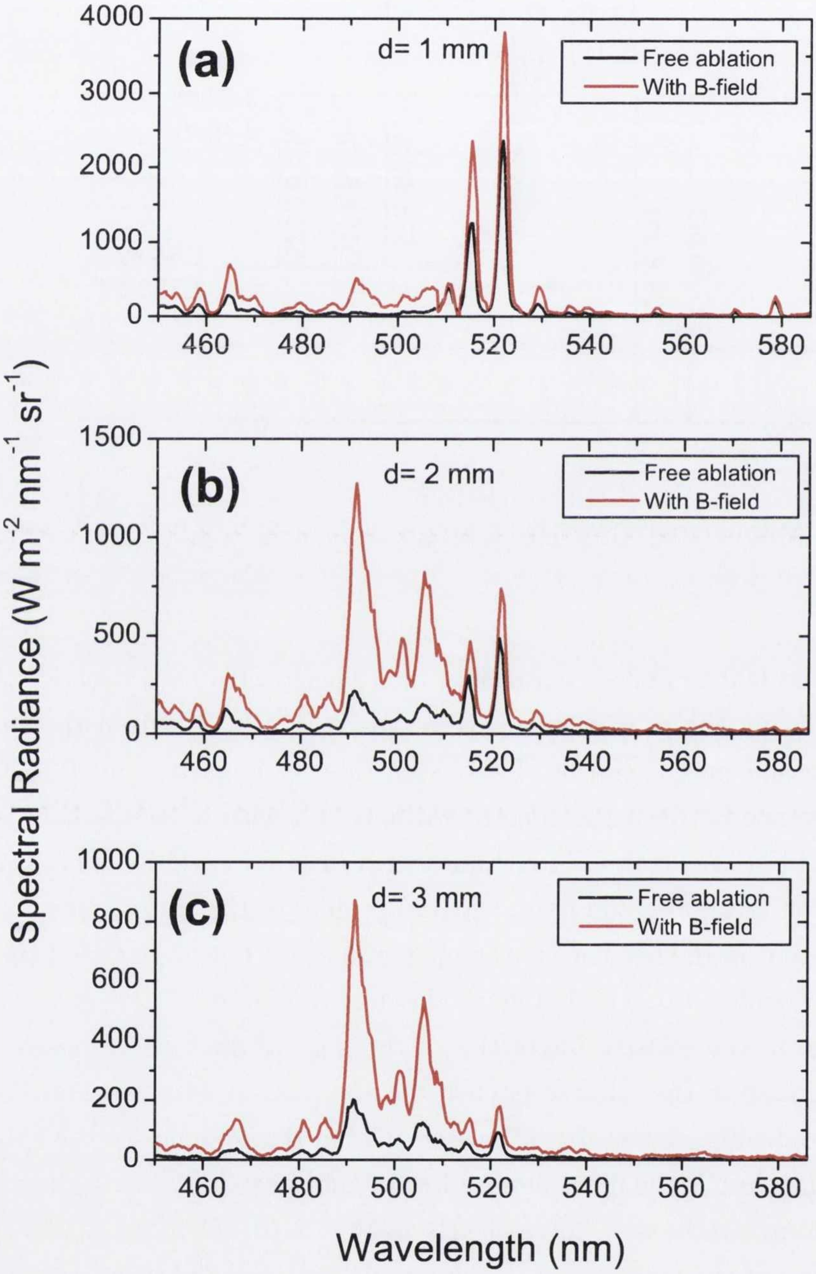

Figure 3.8: Spectra without and with magnetic field at 200 *ns* and at (a) 1 *mm*, (b) 2 *mm* and (c) 3 *mm* from the target surface.

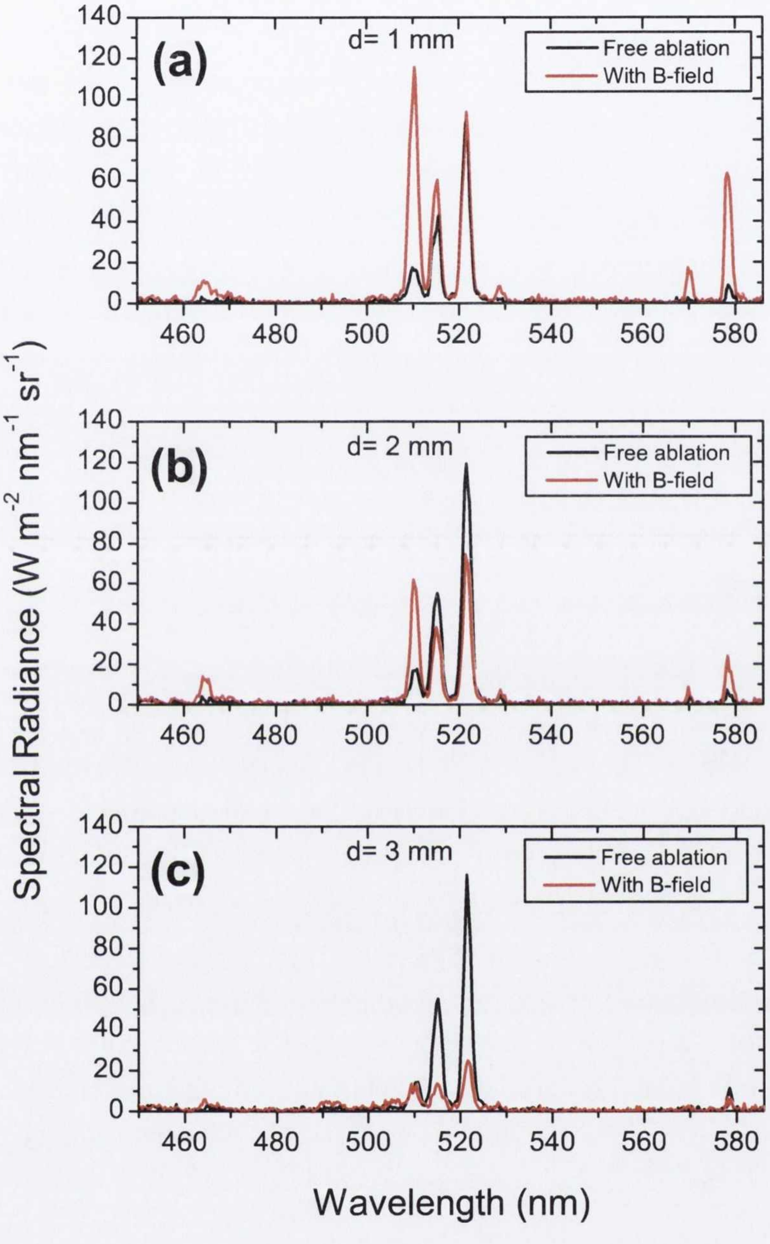

Figure 3.9: Spectra without and with magnetic field at 600 *ns* and at (a) 1 *mm*, (b) 2 *mm* and (c) 3 *mm* from the target surface.

(at 510, 515 and 522 *nm*), in the presence and absence of a magnetic field at two different time delays (200 and 600 *ns*). For free ablation, the position of the maximum intensity of the ionic lines moves from 2 *mm* at 200 *ns* to 7 *mm* at 600 *ns*; while for the neutral lines the maxima are at 0.8 *mm* and 2 *mm*, respectively. In comparison, when the magnetic field is applied, the intensity of the ionic emission is maximized at 2 *mm* at 200 *ns* and at 4.5 *mm* at 600 *ns*; while for the neutral emission the maximum moves by only 0.2 *mm*, i.e. from 0.7 *mm* to 0.9 *mm*. Moreover, without the magnetic field the neutral lines extend out to about 10 *mm*, but with the field the lines are only observable to about 4 *mm*. The spatial extent of the ionic lines also is reduced by the magnetic field.

The influence of the magnetic field can also be presented by calculating the average position, $\bar{z}$, of the emission, *I(z)*, of each line as follow:

$$\bar{z} = \frac{\int_0^\infty zI(z)dz}{\int_0^\infty I(z)dz} \tag{3.3}$$

The temporal variation of $\bar{z}$ for the ionic lines at 491 *nm* and the neutral lines at 510 and 515 *nm* is shown in Fig. 3.11(a) for free ablation and in Fig. 3.11(b) for the magnetic field case. For free ablation the lines emission moves at constant velocity. In particular the 510 *nm* line emission moves with a velocity of about $0.8 \times 10^6\ cm\,s^{-1}$, while the emission from the ionic lines moves at $1.5 \times 10^6\ cm\,s^{-1}$. These values are comparable to the ion velocity at peak flux as measured by the Langmuir probe, though these two measurements represent somewhat different characteristic plume velocities. The higher expansion velocity of the ions with respect to the neutrals can be the result of ambipolar diffusion mechanisms due to charge separation occurring in the first stage of the plasma expansion [66]. In the magnetic field the trajectories of the emissions of both neutral and ionic species, Fig. 3.11(b), are strikingly different from the free ablation case. These trajectories show very clearly that the emission is strongly decelerated in the magnetic field with a deceleration of the order of $\sim -10^{12}\ cm\,s^{-2}$. The average position that the neutral lines reach is about 2 *mm* at $400-500$ *ns* and does not move beyond that point. The average position that the ionic line emission reaches is 5 *mm* at about 500 *ns* and does not move much beyond that point.

The deceleration of the plasma flow and the enhancement in the state of exci-

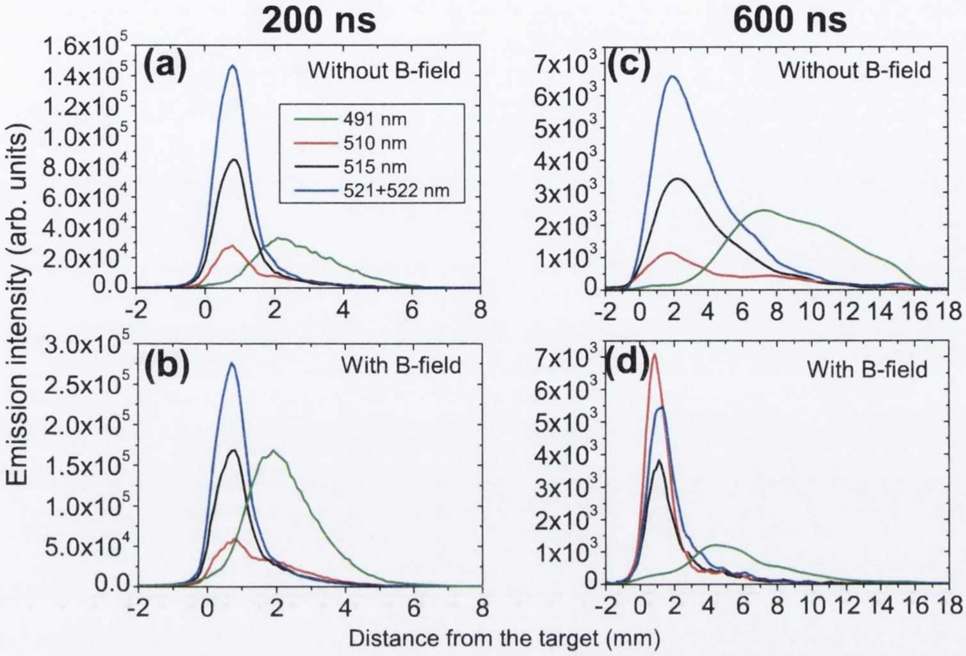

Figure 3.10: Spatial intensity profiles of the ionic lines at about 491 *nm* and of the neutral lines at 510.5, 515.3 and 522 *nm* (a) and (c) without and (b) and (d) with magnetic field at 200 and 600 *ns*.

tation in plasma expanding across magnetic field lines has already been observed by several authors [12, 13]. They attribute these effects to the $\mathbf{J} \times \mathbf{B}$ force and consequent Ohmic heating caused by the induced current, $\mathbf{J}$. As the plume expands across the magnetic field, the $\mathbf{J} \times \mathbf{B}$ term acts to decelerate the flow. This will lead to Joule heating of the electrons so that electrons will have enough energy to continue to excite the expanding plume. Now, because part of the kinetic energy of the plume is transformed into electron heating, the plume slows down. Harilal et al. [12] also observed an increase in temperature when the plasma expands in a magnetic field compared with the free ablation case. The authors attribute this increase to the Ohmic heating. However, our temperature measurements showed no increase in temperature in the presence of the magnetic field - rather, a decrease was detected in the temperature.

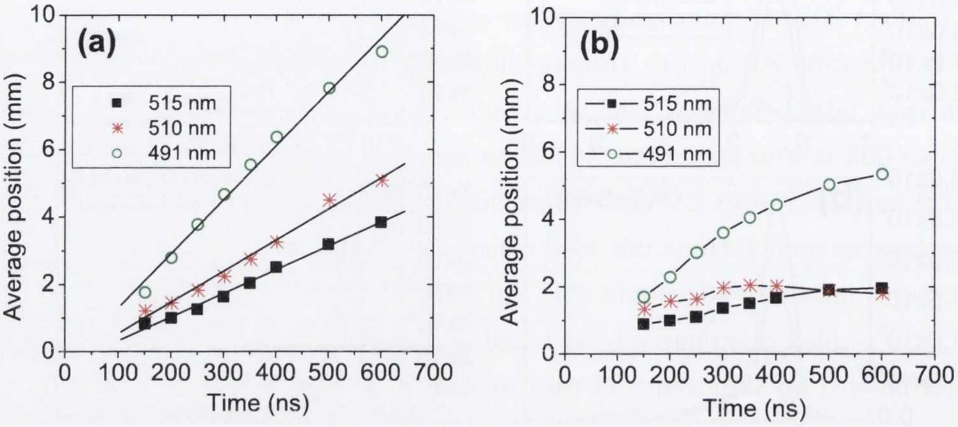

Figure 3.11: Average position of the emission of different lines as a function of time (a) without and (b) with magnetic field. The straight lines in (a) are the linear fit.

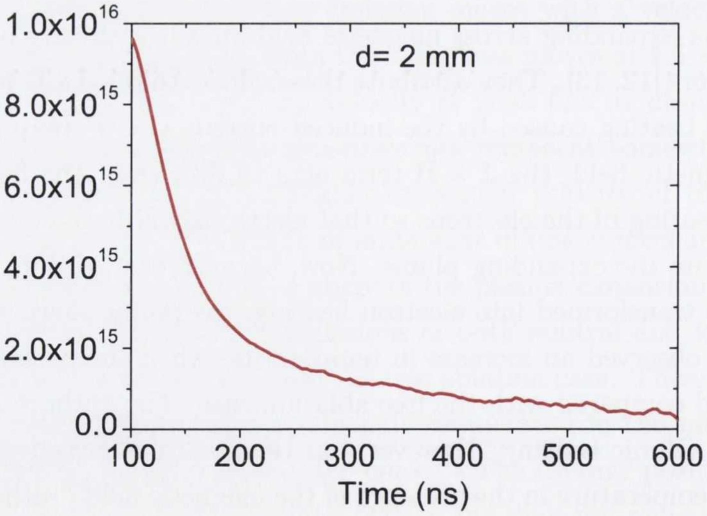

Figure 3.12: Evolution of the ion density at 2 *mm* from the target calculated from the ion signal shown in Fig. 3.3(a).

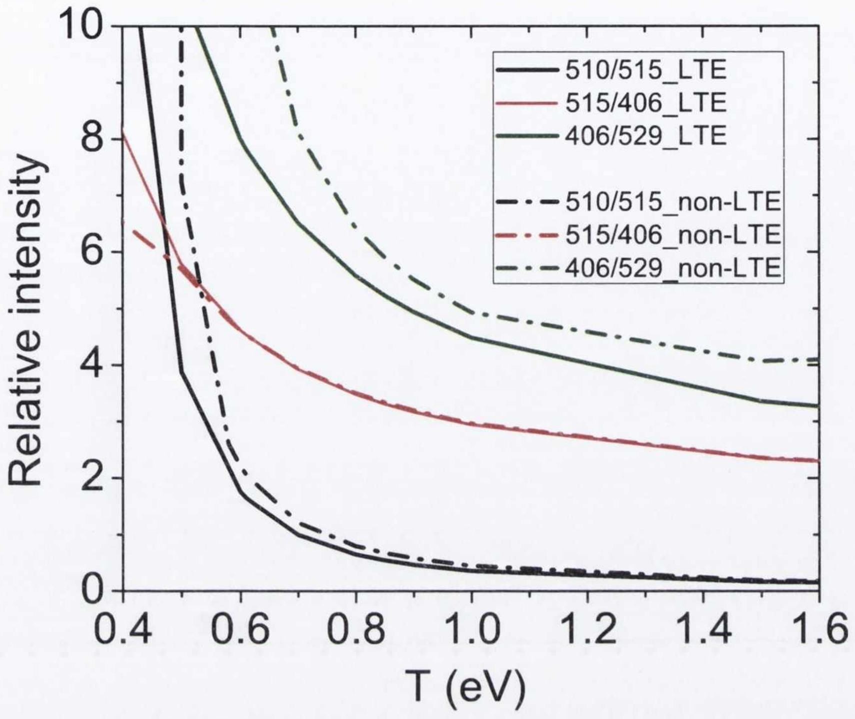

Figure 3.13: Comparison between LTE and non-LTE PrismSPECT calculations of the relative intensities of several Cu I lines. The calculations were done for a plasma with density of 9×10^{14} cm^{-3} and 10 mm thick.

The evolution of the electron temperature was extracted from the emission spectra in Fig. 3.5, using the Boltzmann plot method already discussed in Section 1.3.3. The use of Boltzmann's statistics requires LTE, hence first it should be verified that the condition for LTE is satisfied. According to McWhirter's criterion, equation (1.63), the relative populations of two levels will be in LTE if $n_e \geq 1.6 \times 10^{12}\ \sqrt{T_e}\ (\Delta E)^3\ cm^{-3}$. Thus, assuming a temperature of about 1 eV and a transition energy of 2.5 eV, $n_e \geq 2 \times 10^{15}\ cm^{-3}$ is required to maintain LTE between 4d 2D and 4p 2P multiplets. Fig. 3.12 shows the ion density at 2 mm from the target as a function of the time. It can be seen that at 2 mm from the target, the McWhirter criterion is satisfied for delay times up to about 200 ns, while for later times the plasma density falls below the required value. It should also be said that the density calculated at 2 mm is not an accurate measurement of the density. As shown in Fig. 3.4 the expansion of the plasma starts to be inertial

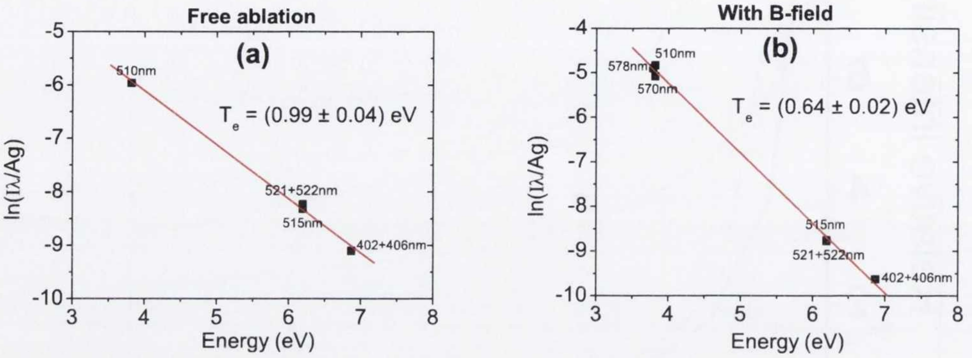

Figure 3.14: Boltzmann plots at 2 *mm* from the target and 600 *ns* (a) for the free ablation case and (b) with the magnetic field.

at about 3.4 *mm* from the target and hence the Anisimov model can be applied for distances ≥ 3.4 *mm*. Therefore the density calculated at 2 *mm* from the target is not an accurate theoretical prediction but an order of magnitude estimate of the density at that point.

In the interpretation of the emission spectra PrismSPECT was also used. Calculations were done in both LTE and non-LTE cases. Fig. 3.13 shows the calculated relative intensities of some Cu I lines. From this plot it was found that the values of temperature obtained by assuming LTE differ from the non-LTE values by less than 0.1 *eV*. Hence we can still use a Boltzmann plot of the relative intensities of the neutral lines to estimate T_e.

Boltzmann plots were analysed for varying time delays and distances from the target to map out the temperature. An example of this is shown in Fig. 3.14. The area under the spectral lines was calculated in order to determine *I*, whilst the values of the upper-level energy, E_u, state degeneracy, g, and transition probability, A_{21} were taken from [64] and are shown in Table 3.1. In Fig. 3.15 it can be seen that at 250 *ns*, T_e is somewhat higher for the magnetic field case; however, at late times (> 400 *ns*) it is lower in the presence of the magnetic field.

The spectral resolution of our spectrometer was not sufficient to use Stark broadening for the measurement of electron density. However through comparison with PrismSPECT, the absolute intensity of the spectral emission may be used

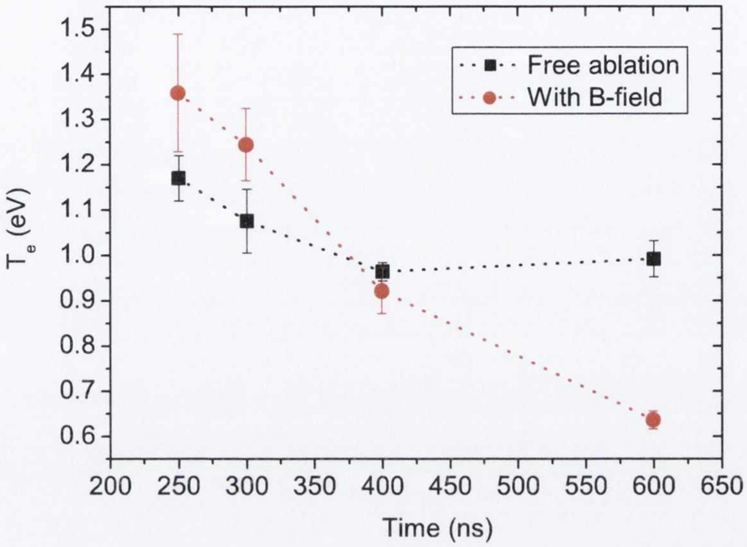

Figure 3.15: Comparison of the temperature T_e with and without magnetic field as a function of time at 2 *mm* from the target surface.

Parameters	Free ablation	With B-field
Thickness (mm)	10	10
Temperature (eV)	0.8	0.6
Density (cm^{-3})	9×10^{14}	5.8×10^{14}

Table 3.2: PrismSPECT parameters used to fit the measured spectra at 600 *ns* and 2 *mm* from the target.

to estimate the plasma density. Fig. 3.16 shows the fit of the calculated with the measured spectra at 600 *ns* and 2 *mm* from the target surface. These PrismSPECT calculations were done in non-LTE mode; the input parameters used in both cases without and with magnetic field, are summarized in Table 3.2. From Fig. 3.4 the transverse plume dimension (in the y-direction) at 600 *ns* is $\sim$ 10 *mm*, then a plasma thickness of 10 *mm* was chosen for these calculations. The plasma density extracted from the fitting of the spectra acquired without a magnetic field was 9×10^{14} cm^{-3}, while with the magnetic field the lower value of 5.8×10^{14} cm^{-3}

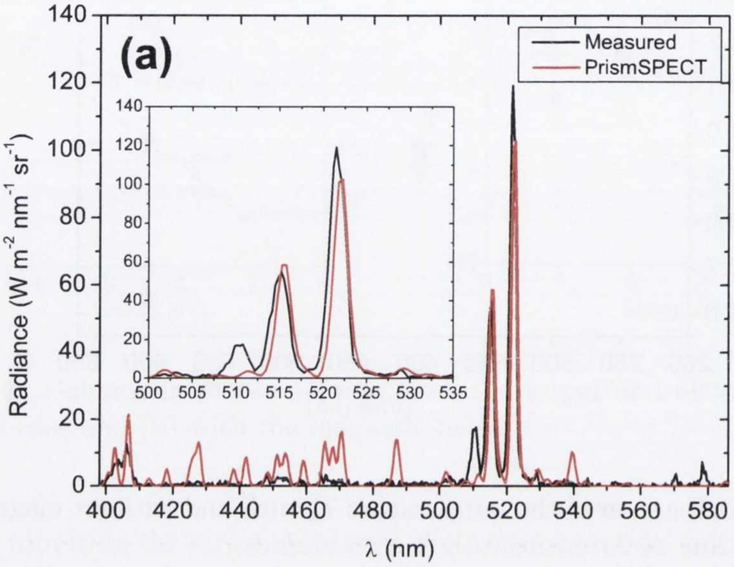

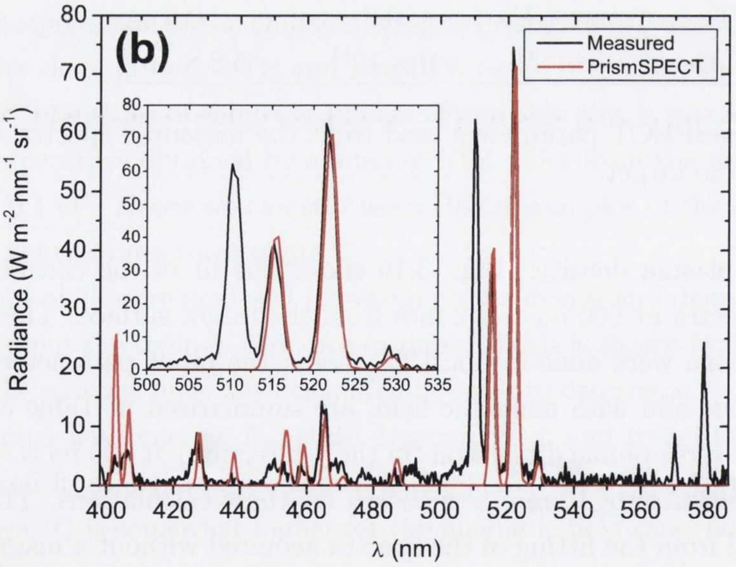

Figure 3.16: Fit of the calculated with measured spectra at 600 *ns* and at 2 *mm* from the target surface (a) without and (b) with magnetic field.

was found. The value of density found from the fit in the free ablation case is in good agreement with the value of density of $7.3 \times 10^{14}\ cm^{-3}$ estimated from the ion probe signal in Fig. 3.3. The lower value of density in the magnetic field case may be due to the lateral expansion of the plasma, i.e. along the magnetic field lines.

3.4 Discussion

As discussed in Section 1.2.2, the plasma can expand freely along the magnetic field lines. Conversely, in the direction orthogonal to the magnetic field, the velocity is in inverse proportion to B as detailed in equation (1.50). Hence the plasma is expected to be decelerated as it expands across the magnetic field. Plasma deceleration and confinement are very evident in the results described above, in particular in Fig. 3.5, Fig. 3.10 and 3.11. The extent of plasma confinement towards the target by the magnetic field can be compared with the one found from the MHD model described in Section 1.2. An estimate of the stopping distance can be determined by considering the position where the plasma pressure is equal to the magnetic pressure. However, it is known that for a LPP expanding freely in vacuum, thermal energy is quickly converted to kinetic energy associated with the plasma flow [34], hence the thermal energy can be neglected.

The ion probe signal can be used to estimate the ram pressure due to the plasma flow. The ram pressure is $P_R = n_i m_i v_i^2$, where n_i is the ion density, m_i is the ion mass and v_i is the ion velocity. At the probe position ($10\ cm$) the ion density at the time of maximum ion flux ($4\ \mu s$) can be calculated using equation (2.1) and is $\sim 8 \times 10^{16}\ m^{-3}$. This corresponds to a ram pressure of $\sim 5\ Nm^{-2}$. For a 3D self-similar expansion this ram pressure will scale as (plasma dimension)$^{1/3}$. The magnetic pressure ($P_B = B^2/2\mu_0$) for $320\ mT$ is $4 \times 10^4\ Nm^{-2}$. Thus the ram pressure will be equal to the magnetic pressure at $5\ mm$. This is in good agreement with the experimental results shown above. The neutral emission shows a stopping distance of $2\ mm$, while for the ion emission the value is $5 - 6\ mm$.

It is also possible to estimate the stopping distance using the hemispherical magnetic model of Ripin et al. [40]. The authors determined the stopping distance from the work done by the plasma to exclude the magnetic field from its volume.

As discussed in Section 1.2.2, since the plasma is a conductive medium, as it expands in the magnetic field an internal diamagnetic current arises to exclude the field from its interior. This diamagnetic current interacts with the magnetic field through the **J** × **B** force. The **J** × **B** term acts to decelerate the forward motion of the plume. At early time the plasma thermal pressure and the ram pressure are both much greater than the magnetic pressure. Thus the expansion is diamagnetic in nature and will continue until the excluded magnetic energy is comparable to the total plasma energy. Ripin et al. assume the exclusion of the field to be complete and the expansion of the plasma to be hemispherical. Thus, from the conservation of energy, the stopping radius R_B is [40]:

$$R_B = \sqrt[3]{\frac{3\mu_0 E_{La}}{2\pi B^2}} \tag{3.4}$$

where E_{La} is the laser energy absorbed in the ablation plume. While we have not measured the fraction of the laser energy absorbed in the plasma, on the basis of previous reports, it is likely to be less than 50% [24, 67]. Taking laser energy absorbed in the plasma to be $\sim 20\ mJ$ (i.e. 50%), then according to equation (3.4), it is expected that in a 320 mT field the plume will be stopped when it reaches a radius of 4.4 mm, in agreement with the value found above.

The deceleration due to the work done by the plasma to exclude the magnetic field from its volume is given by equation (1.49) and it is re-written below for clarity [40]:

$$g = \frac{\pi B^2}{\mu_0 M_0} r^2$$

where M_0 is the mass of the plasma. Typically the number of atoms ablated per shot is $\sim 1 \times 10^{15}$, which, for copper atoms, corresponds to a mass of $1.055 \times 10^{-10}\ kg$. Then, taking r in the above equation to be R_B, g is $\sim 2 \times 10^{12}\ cm\ s^{-2}$. This value agrees well with the deceleration of the plasma observed in Fig. 3.11.

As mentioned above, at 600 ns the plasma density profile derived from the Langmuir probe signal (Fig. 3.3) has two components, one at few millimeters from the target ($\leq 3\ mm$) and the other at 9 mm. These features are well correlated with the positions of the maximum emissions on the ion and neutral lines shown in Fig. 3.10. At first it may seem surprising to find neutral line emission correlated

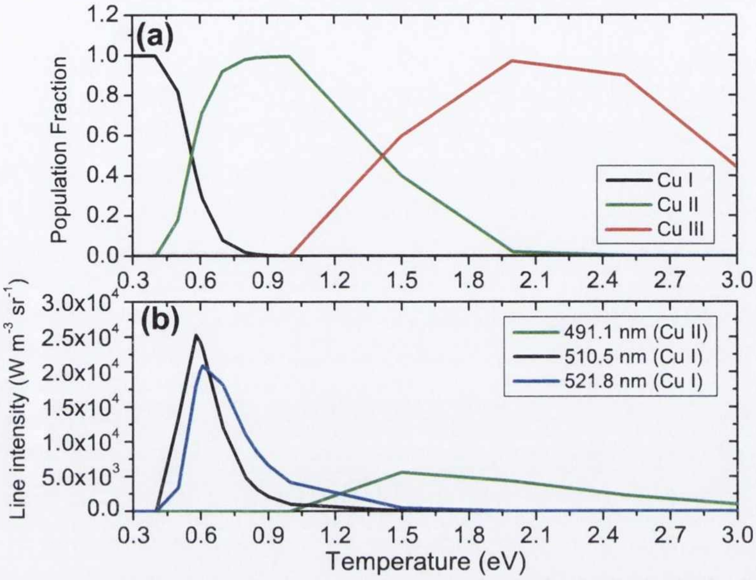

Figure 3.17: (a) Population fraction of Cu I, Cu II and Cu III and (b) intensity of the ionic line at 491 *nm* and the neutral lines at 510 and 521.8 *nm* as a function of the temperature calculated with PrismSPECT for a plasma with an ion-atom density of $9 \times 10^{14}\ cm^{-3}$.

in space with singly ionized species. However, this observation can be explained using PrismSPECT. Fig. 3.17(a) shows the population fractions of Cu I, Cu II and Cu III as a function of the temperature calculated with PrismSPECT in non-LTE mode for a plasma with an ion-atom density of $9 \times 10^{14}\ cm^{-3}$. While Fig. 3.17(b) shows the calculated intensity of the lines at 491, 510.5 and 521.8 *nm* as a function of the temperature. It can be seen that the Cu II ions are predominant for T_e between 0.6 and 1.4 *eV*, while the emission of a Cu I line such as the line at 521.8 *nm* is strong in the same range of temperature. Similarly, the Cu III ions predominate between 1.4 and 2.8 *eV*, while the Cu II line is strong between 1.2 and 2.8 *eV*. This suggests that there is a correlation of the spatial distribution of a particular line emission with the spatial distribution of the species of the next ionization stage. This is due to the fact that, when a particular excited level is in LTE with higher levels and the ground state of the next ion, there will be strong collisional exchange between the excited level and the next ion. This correlation can also explain why the neutral emission is strongly confined by the magnetic field.

As mentioned above, at late times (> 400 *ns*) the value of T_e derived from the spectral line emission is lower with the magnetic field than for free ablation. From 400 to 600 *ns* with the magnetic field, there is a relative enhancement of the lines at 510, 570 and 578 *nm*. Fig. 3.9 and 3.10 clearly show this relative change in the line intensity. As an example, it can be seen that at 600 *ns* and 1 *mm* from the target, the lines at 510, 570 and 578 *nm* are stronger in the magnetic field by a factor of about 7 compared with the free ablation case. These three lines are due to radiative decay of the $3d^{10}4p\ ^2P_{1/2,3/2}$ (see Fig.3.7), which are lower in energy than the other excited levels of interest. As shown by Fig. 3.17(b) the intensity of the line at 510 *nm* becomes higher than the other neutral lines for temperature below 0.65 eV. Comparing this with Fig. 3.15 it is possible to conclude that it is the lower value of T_e with the magnetic field at late time which accounts for the relative enhancement of the lines at 510, 570 and 578 *nm*.

Chapter 4

Plasma expansion along a magnetic field

This chapter describes the results of experiments to investigate the expansion of a copper LPP along a magnetic field. The aim was to confine the lateral expansion of the plasma. Analysis techniques included ICCD imaging, spectroscopy, Langmuir ion probe measurements and thin film depositions.

4.1 Experimental setup

A schematic of the experimental setup is shown in Fig. 4.1. The magnetic field for this experiment was produced by two Nd-Fe-B ring magnets attached to an iron yoke. The magnets used here were the same as those used in the experiment described in the previous chapter (Section 3.1). The distance between the magnets was 35 *mm*. The origin of the coordinate system used to describe the field is taken to be on the axis of the system and midway between the magnets, as shown in Fig. 4.1. The magnetic field configuration was designed using COMSOL [63] and shown in Fig. 4.2. In particular, Fig. 4.2(a) shows the calculated magnetic field lines and the position of the target between the magnets. Fig. 4.2(b) shows the variation of the field along the z direction for $x = y = 0$; Fig. 4.2(c) and (d) show the variation in the x or y direction at $z = 0$ and $z = -9.5$ *mm* (which corresponds to the target position), respectively. The magnetic field was measured with a Hall probe and,

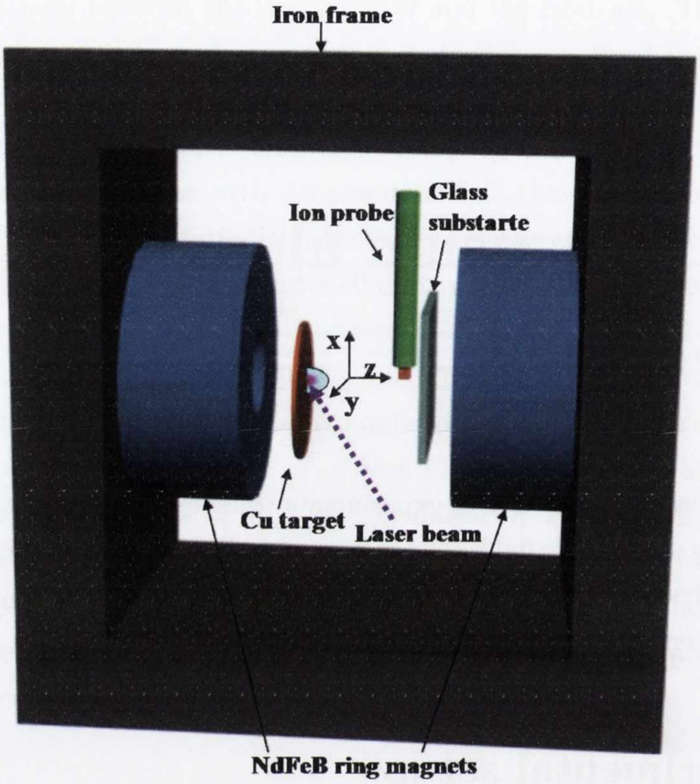

Figure 4.1: Schematic of the experimental setup.

as can be seen in Fig. 4.2(c)-(d) the calculated field profiles agree closely with Hall probe measurements. Along the z direction the field increases rapidly from a value of 11 mT at the magnet surface to 320 mT at 8 mm from the surface and remains constant at this value over a region spanning 20 mm. The copper target was placed at 8 mm from the surface of one of the magnets ($z = -9.5\ mm$) as indicated by the vertical line in Fig. 4.2(b). Thus the plasma is produced in, and expands into, a region of uniform field. The distance of the target with respect to the magnet surface was varied from 1.5 mm ($z = -16\ mm$) to 17.5 mm ($z = 0$). However, since no substantial differences were observed in the plasma dynamics, only the results of the measurements obtained with the target at $z = -9.5\ mm$ are shown herein.

A 248 nm , 20 ns excimer laser was used to irradiate the Cu target in a stainless steel vacuum chamber, at a pressure of about 10^{-4} $mbar$. The laser spot area was

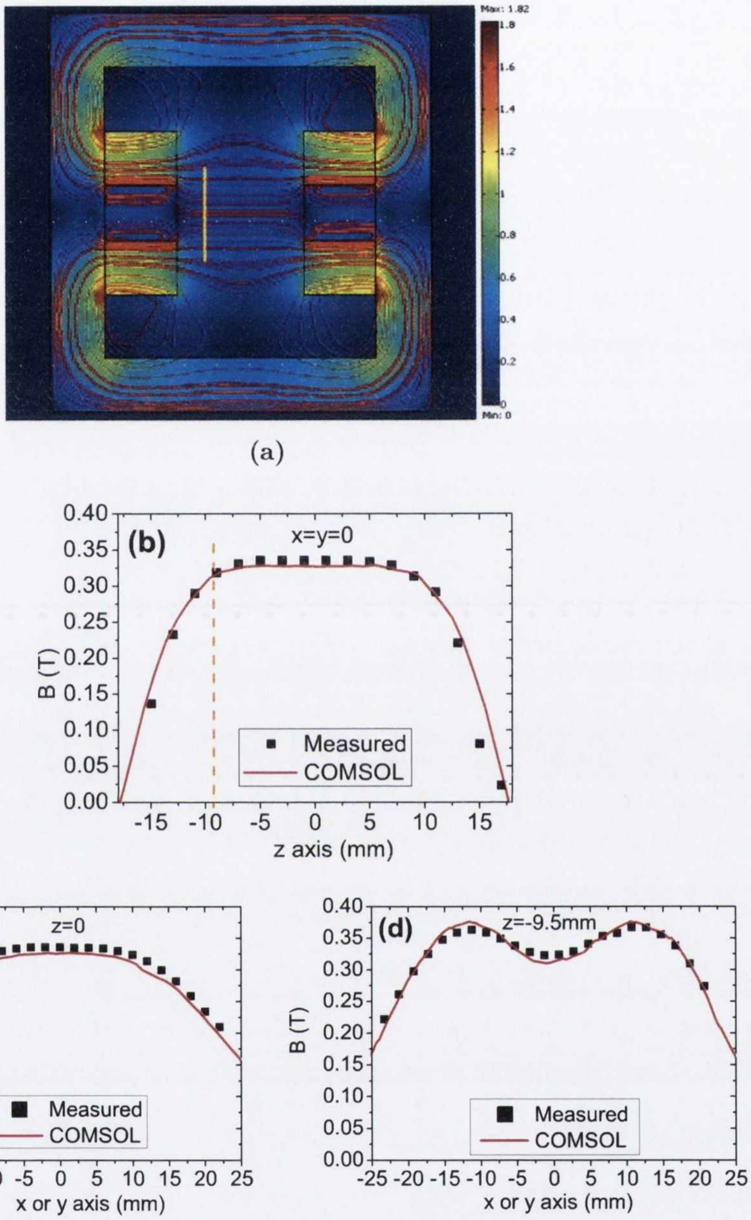

Figure 4.2: (a) Calculated magnetic field lines. The color scale indicates the magnetic field strength in T. The vertical orange line indicates the position of the target; (b), (c) and (d) comparison of the measured and calculated magnetic field profiles. The target is positioned at $z = -9.5\ mm$. In (b) the dashed line indicates the position of the target.

0.02 cm^2 giving a fluence of about 4 $J\ cm^{-2}$. The target was rotated to reduce drilling.

The influence of the magnetic field on the plasma flow was investigated as follows. The ion flux was measured using a planar ion probe negatively biased at $-10\ V$. The probe was $2 \times 2\ mm^2$ and was placed on the z axis at 20 mm from the target and oriented to face the target.

Time resolved optical imaging and time- and space-resolved optical emission spectrometry of the plasma self-emission was also used viewing the plasma in the y-direction, i.e. orthogonal to the target normal. The time resolved optical imaging shows the evolution of the shape of the plasma plume and it was done with an ICCD with a minimum gate time of 2 ns.

For the emission spectrometry, a spectrometer coupled with a second ICCD was used. The details of the optical setup was already described in the second chapter - see Fig. 2.2. Both the ICCDs used in this experiment were triggered to record the emission simultaneously and at various time delays after the laser had fired. At each time delay the background was acquired and subtracted from the corresponding emission signal.

Furthermore, depositions on glass substrates were made at 20 mm from the target to investigate how the magnetic field influences the amount and spatial distribution of the ablated material.

The set of measurements presented herein were repeated several times and they were found to be reproducible.

4.2 Mass ablated

At first, the mass ablated per pulse was measured in both cases, without and with the magnetic field. Keeping the target stationary, a small crater was formed in the Cu target with 1000 laser shots. The ablation spot was nearly elliptical with minor and major diameters of 1.25 mm and 2.1 mm, respectively. The elliptical crater was scanned using a surface profiler and the ablation mass per pulse estimated. Fig. 4.3 shows the crater profile along the minor axis. The maximum ablation depth per pulse was about 16 nm in both cases, without and with magnetic field. Without the magnetic field the number of atoms ablated per

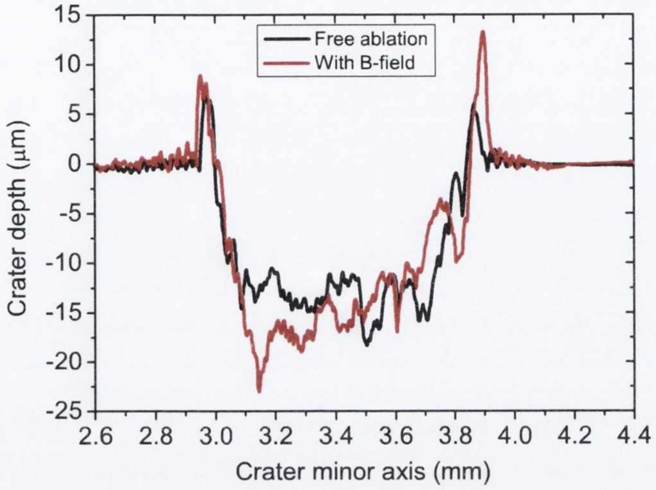

Figure 4.3: Comparison of the crater profiles along the minor axis obtained without and with magnetic field with 1000 laser shots.

shot was $(1.6 \pm 0.1) \times 10^{15}$ and with the magnetic field was $(1.8 \pm 0.1) \times 10^{15}$. Thus, within the accuracy of the measurement, the field does not influence the amount of material ablated.

4.3 Langmuir ion probe measurements

Fig. 4.4(a) shows the ion current per unit area at 2 cm from the target recorded on the Langmuir ion probe for both free ablation and in the presence of the magnetic field. The TOF at the maximum ion flux for the free ablation is 1.2 μs which corresponds to an ion velocity of 1.6×10^6 $cm\, s^{-1}$ and ion energy of 94 eV. In the free ablation case, since the expansion is self-similar, the ion signal was used to estimate the plasma density profile at 600 ns as a function of the distance and it is shown in Fig. 4.4(b). Indeed the ion TOF signal was used to find the ion energy distribution through equation (2.5) and it is shown in Fig. 4.4(c). The average energy is about 63 eV, but it can be seen that the ion energies range up to about 200 eV.

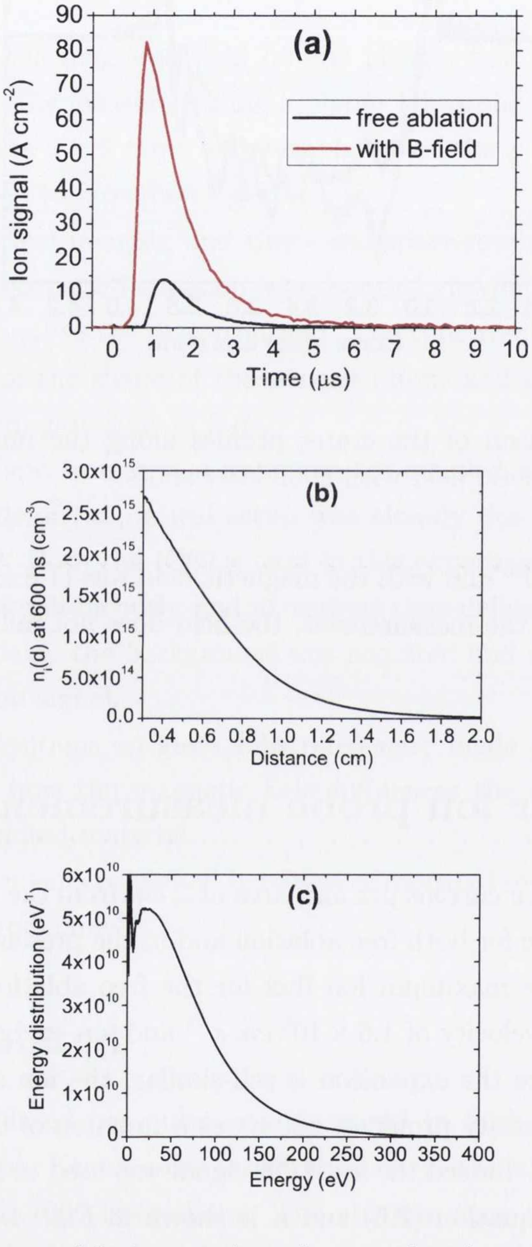

Figure 4.4: (a) Ion time of flight signals without and with magnetic field acquired with Langmuir probe at 2 *cm* from the target, at a laser fluence of 3 $J\ cm^{-2}$. (b) Ion density profile at 600 *ns* as function of the distance from the target and (c) ion energy distribution in the free ablation case.

	t_p (μs)	v_p ($cm\, s^{-1}$)	v_f ($cm\, s^{-1}$)	Ion yield ($ions\, cm^{-2}$)
Without B-field	1.2	1.6×10^6	2.4×10^6	1.15×10^{14}
With B-field	0.8	2.5×10^6	3.6×10^6	7×10^{14}

Table 4.1: Results obtained from the ion signals in Fig. 4.4(a). t_p is the time at the peak ion flux; v_p is the peak ion velocity; v_f is the front velocity.

Fig. 4.4(a) also shows the ion probe signal at 2 *cm* in the presence of the axial magnetic field. Since the magnetic field is normal to the surface of the probe, it should not significantly influence the ion signal due to plasma flow along the field lines. The peak ion current density is 6 times higher than the free ablation case, indicating substantial concentration of the plasma flow in the forward direction. Assuming the ions are mainly singly charged, the signals in Fig. 4.4(a) can be used to find the ion yields. The values are: $1.15 \times 10^{14}\ ions\, cm^{-2}$ without the field and $7 \times 10^{14}\ ions\ cm^{-2}$ with the field. It can also be noted that, with magnetic field, the arrival of the plasma at the probe and TOF at maximum of the ion signal occurs at earlier times than for the free ablation, which would seem to indicate a faster forward expansion, at least for some part of the flight from the target to the probe. Table 4.1 summarizes the main results found from the ion probe measurements.

4.4 ICCD imaging

Fig. 4.5 shows images of the plasma self-emission at various delays after the laser pulse. Longer gate widths were used for the longer delays, but the gain setting on the intensifier was kept constant. For free ablation the plume shows the normal, approximately semi-ellipsoidal, shape. The plume front moves out from the target at about $2.15 \times 10^6\ cm\, s^{-1}$, which is in good agreement with the value of $2.4 \times 10^6\ cm\, s^{-1}$ found from ion probe signal. In the presence of the magnetic field the plume is distinctly different. Up to delays of about 300 *ns* the two cases are quite similar, but at 300 *ns* the plume in the magnetic field begins to look more cylindrical. From 300 *ns* onwards a rather flat conical flare is observed near the

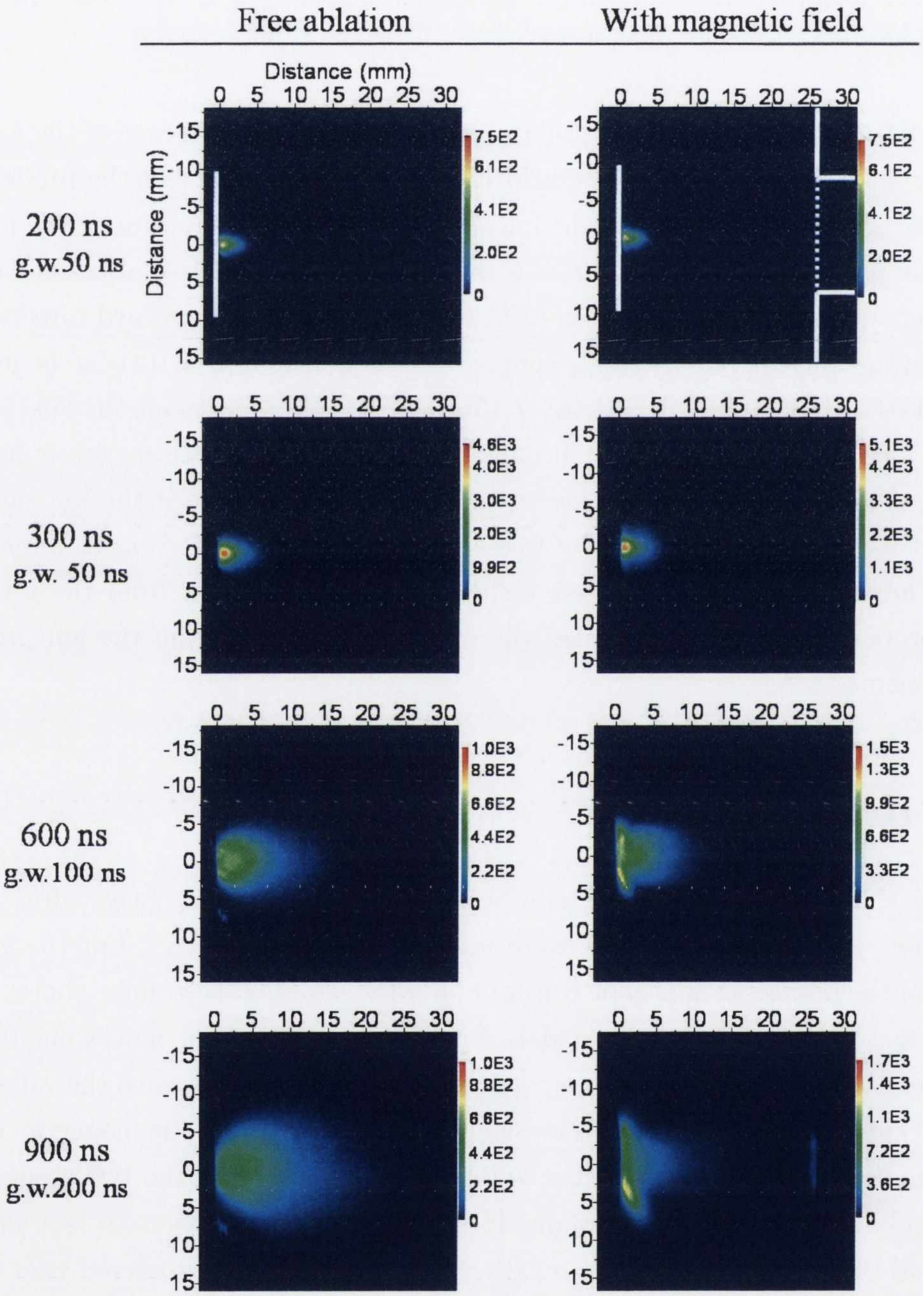
Free ablation
With magnetic field
Distance (mm)
Distance (mm)
0 5 10 15 20 25 30
-15 -10 -5 0 5 10 15
200 ns
g.w.50 ns
7.5E2
6.1E2
4.1E2
2.0E2
0
300 ns
g.w. 50 ns
4.6E3
4.0E3
3.0E3
2.0E3
9.9E2
0
5.1E3
4.4E3
3.3E3
2.2E3
1.1E3
0
600 ns
g.w.100 ns
1.0E3
8.8E2
6.6E2
4.4E2
2.2E2
0
1.5E3
1.3E3
9.9E2
6.6E2
3.3E2
0
900 ns
g.w.200 ns
1.0E3
8.8E2
6.6E2
4.4E2
2.2E2
0
1.7E3
1.4E3
1.1E3
7.2E2
3.6E2
0

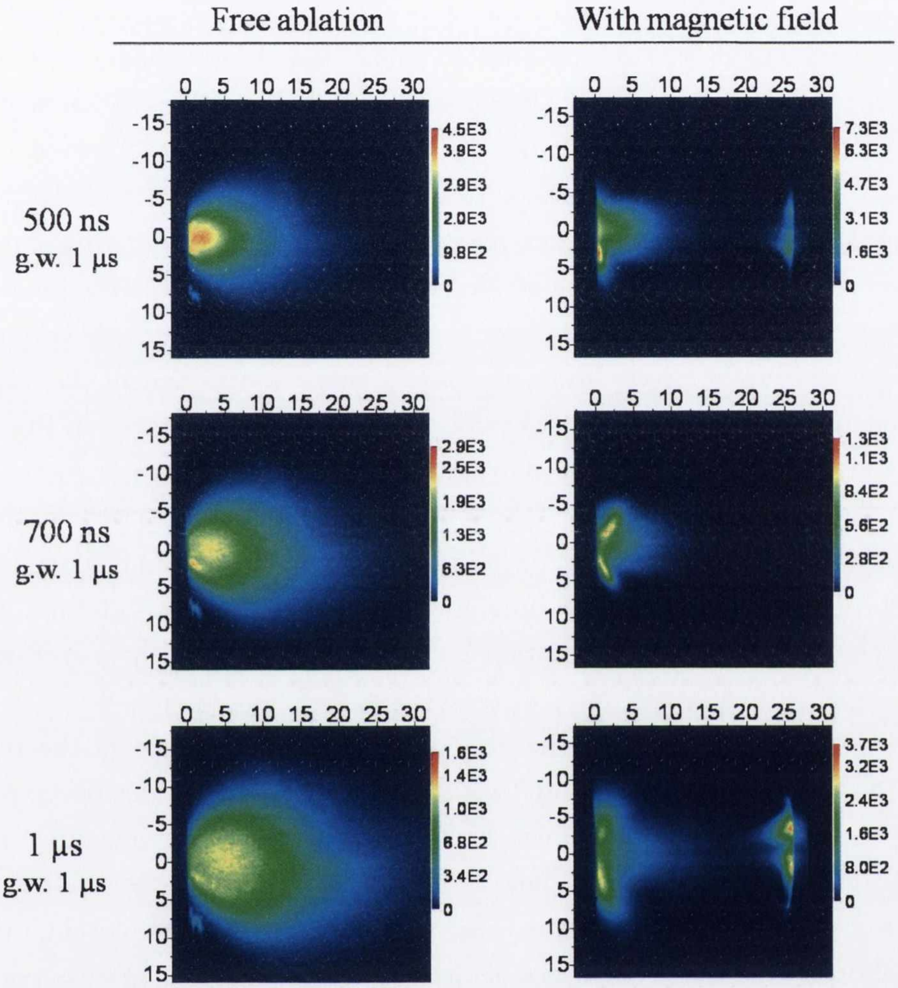

Figure 4.5: Time resolved images of the Cu plasma self-emission acquired with the ICCD without, and with, magnetic field. The time delays and the gate time-width, g.w., relative to each image are indicated in the first column. The images were acquired with the same gain and are background corrected. Top images show the position of the target and the magnets opposite to the target. The dashed line indicates the hole of the magnets.

target surface. From 600 *ns* onward the cylindrical plume shape is more evident and the flare structure continues to develop. The emission from the region beyond 10 *mm* remains weak, but clearly plasma is moving through this region since its arrival at the hole in the magnet in front of the target can be observed. The light emission from the region at the surface of the magnet in front of the target first appears at about 600 *ns*, indicating a plasma velocity of 4.5×10^6 $cm\ s^{-1}$, which is comparable with the value of 3.6×10^{-6} $cm\, s^{-1}$ found from the ion probe signal. At 1 μs delay the flare emission and the cylindrical plume between the magnets are very clear. In addition, intense emission is observed in the edge of the hole in the magnet in front of the target. In this region, as shown in Fig. 4.2, the magnetic field lines, which are axial in the region between the magnets, turn sharply to a more radial direction. There is then a component of field normal to the plasma velocity. The radial field will act to decelerate the axial flow (similarly to the experiment discussed in the previous chapter) and heat the plasma. Also, the confinement due to the deceleration increases collisions, which re-excites the plume.

Strong radial confinement of the plume by the magnetic field in the region between the magnets is expected and is similar to the confinement observed by Pisarczyk et al. [16], albeit for much hotter plasma and higher magnetic field. The X-ray images in that paper show an emission region of larger radius near the target, but not the flare described above. The flare emission may be due to an interaction near the target surface of the radial component of plasma velocity with magnetic field inducing an azimuthal current which heats the plasma in that region. However, full physical description requires detailed fluid modeling.

4.5 Spectroscopic measurements

Fig. 4.6 shows a comparison of space-resolved spectra without, and with, magnetic field which have been acquired simultaneously to the images in Fig. 4.5. From these spectral images it is possible to follow the expansion of the plume in the region from the surface (zero position) to 19 *mm* in front of the target. Thus the surface of the second magnet is not visible in these spectral images. The spectral lines observed here are the same as those observed in the experiment described

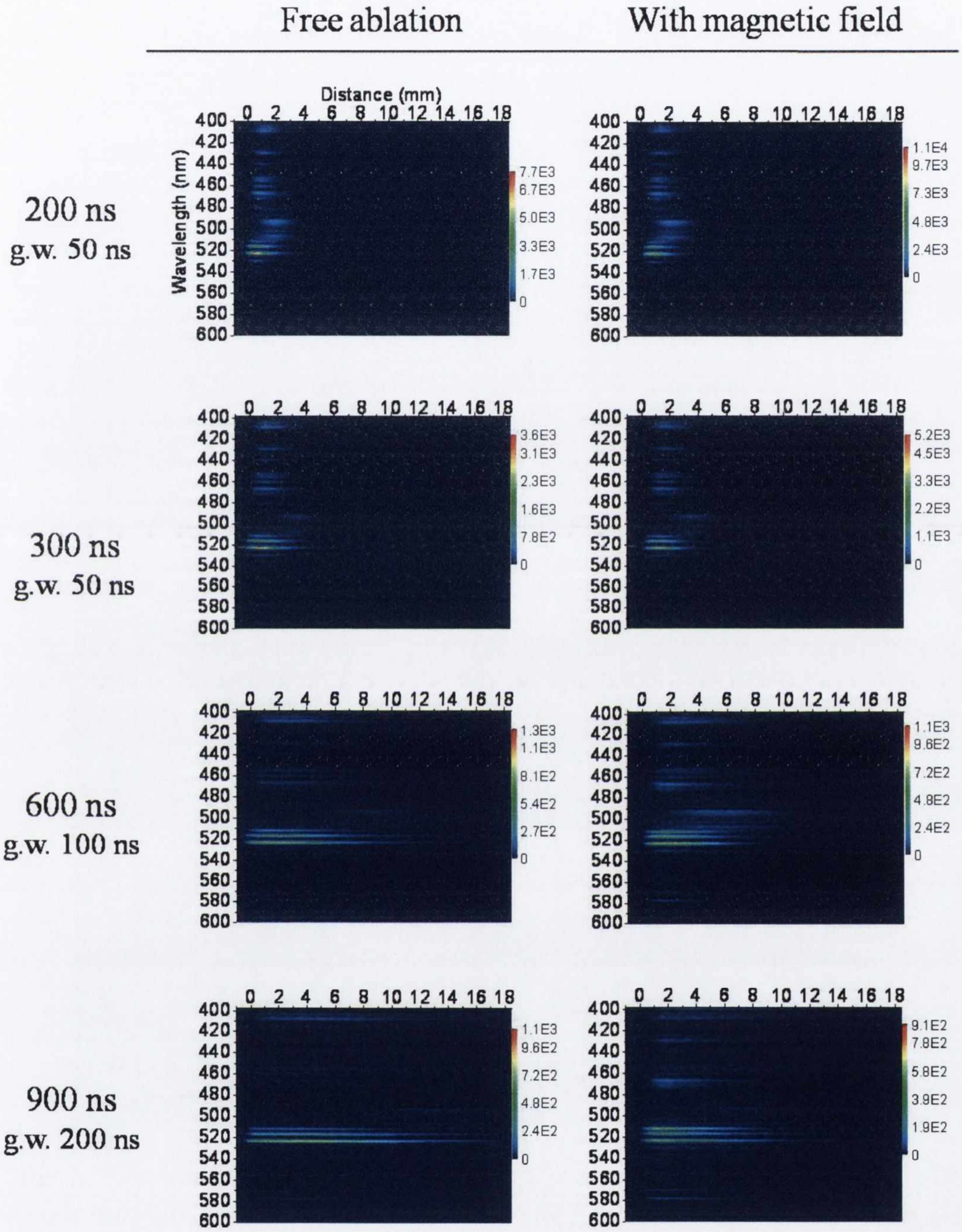
Free ablation
With magnetic field
200 ns
g.w. 50 ns
300 ns
g.w. 50 ns
600 ns
g.w. 100 ns
900 ns
g.w. 200 ns
Distance (mm)
Wavelength (nm)
0 2 4 6 8 10 12 14 16 18
400 420 440 460 480 500 520 540 560 580 600
7.7E3 6.7E3 5.0E3 3.3E3 1.7E3 0
1.1E4 9.7E3 7.3E3 4.8E3 2.4E3 0
3.6E3 3.1E3 2.3E3 1.6E3 7.8E2 0
5.2E3 4.5E3 3.3E3 2.2E3 1.1E3 0
1.3E3 1.1E3 8.1E2 5.4E2 2.7E2 0
1.1E3 9.6E2 7.2E2 4.8E2 2.4E2 0
1.1E3 9.6E2 7.2E2 4.8E2 2.4E2 0
9.1E2 7.8E2 5.8E2 3.9E2 1.9E2 0

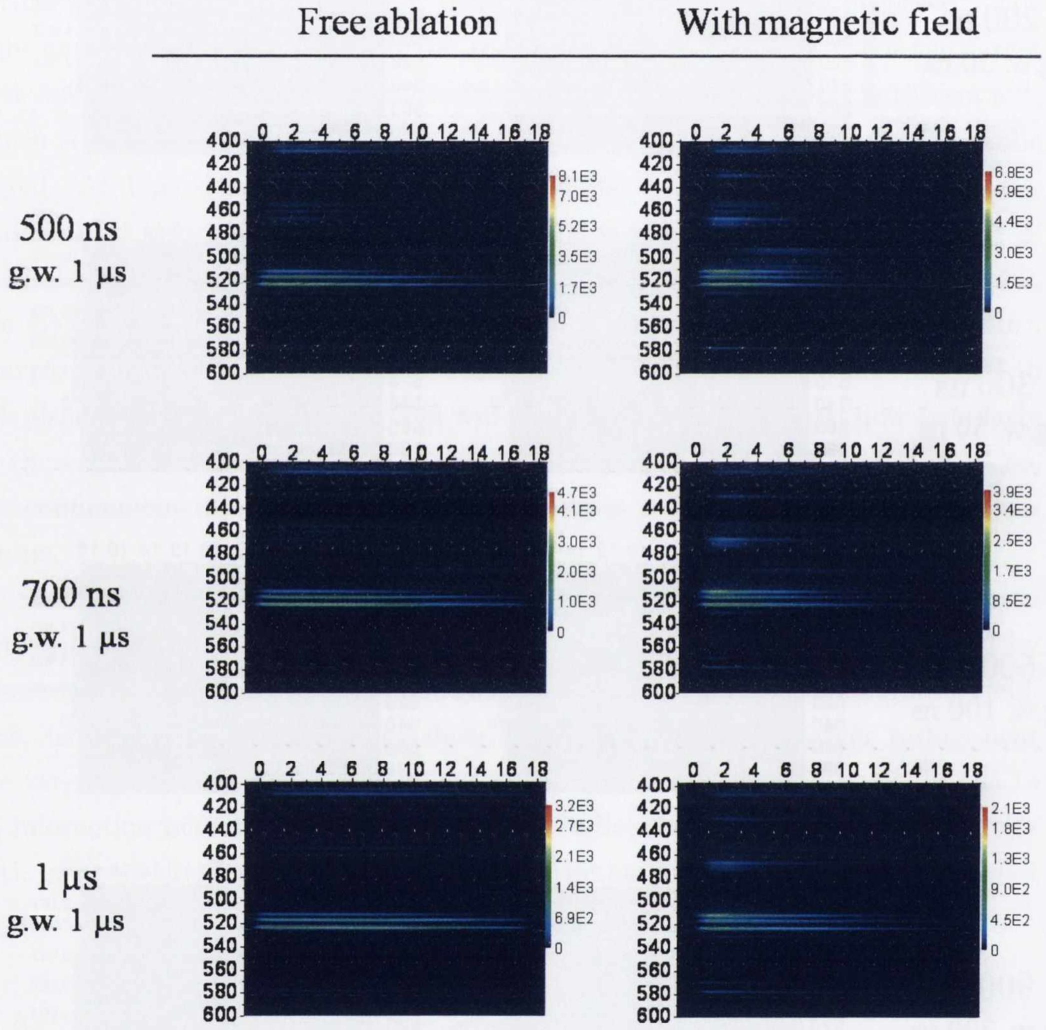

Figure 4.6: Time- and space-resolved spectra of the Cu ablation plume for various time delays, without and with magnetic field. The time delays and the gate time-width, g.w., relative to each image are indicated in the first column. The images were acquired with the same gain and are background corrected.

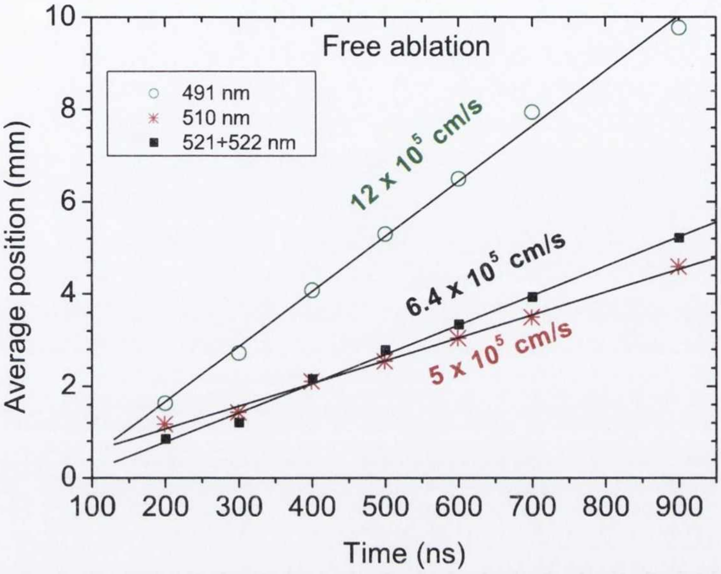

Figure 4.7: Average position of the emission of different lines as a function of time without magnetic field. Also indicated are the velocities obtained from the linear fits.

in the previous chapter. The three strongest lines are the neutral lines at 510.69, 515.32 and 522.15-521.81 *nm*. The Cu II emission about 491 *nm* is also observed. Fig. 4.7 shows the average position as a function of time of the emission of the ionic lines at about 491 *nm* and the two neutral lines at 510 and 521+522 nm for the free ablation. The emission of the Cu II lines moves away from the target with a velocity comparable to the values obtained from the ion probe and the time resolved imaging. Once again it can be noted the ion feature is moving away from the target more rapidly than the neutral lines and, as already discussed in Chapter 3, this is a normal feature of space resolved spectra from LPP. Fig. 4.8 shows the spectra obtained at 1 and 4 *mm* from the target at time 900 *ns* without and with magnetic field. In the free ablation case the spectra at 1 and 4 mm are very similar. From this specra and from the spectral images obtained without a magnetic field it can be noted that at times (900 $ns - 1\ \mu s$) the neutral emission is nearly uniform. It should be remembered however that in these space-resolved

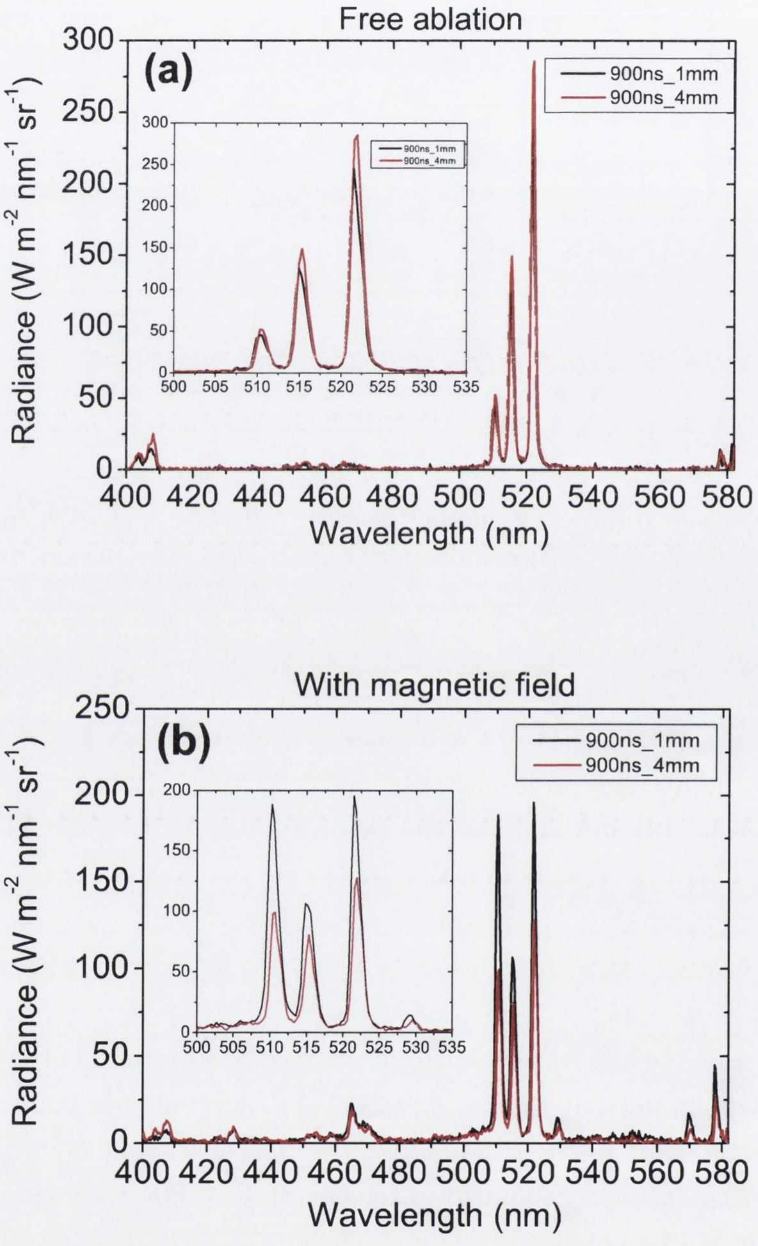

Figure 4.8: Spectra at 1 and 4 *mm* at 900 *ns* (a) without and (b) with magnetic field.

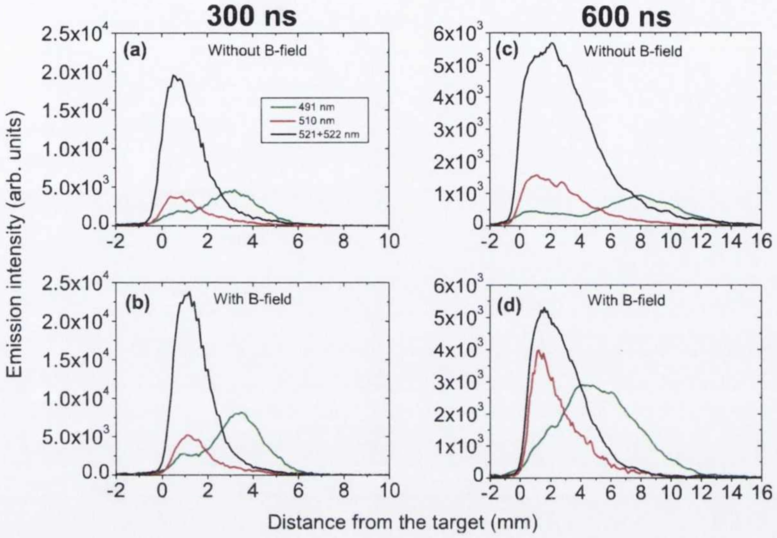

Figure 4.9: Spatial intensity profiles of the ionic lines at about 491 *nm* and of the neutral lines at 510, and 522 *nm* (a) and (c) without and (b) and (d) with magnetic field at 300 *ns* and 600 *ns*.

spectra, the emission is collected from a thin horizontal slice of the plume.

In the presence of the magnetic field the spectra are different in several respects from the free ablation case. For most of the time interval examined, with the magnetic field present, the lines are particularly bright near the target, which may be due to the flare structure. After about 10 *mm* the line intensity drops, in agreement with the images in Fig. 4.5. Furthermore, the intensity of the ionic lines at around 491 nm is distinctly stronger in the magnetic field. Fig. 4.9 shows the spatial intensity profiles of the ionic lines at around 491 *nm* and the two neutral lines at 510, 522 *nm*, without and with magnetic field. As can be seen, the ionic emission in the presence of the magnetic field is about 2-3 times higher than in the free ablation case. This suggests the magnetic field is concentrating the plasma along the axis of expansion. At times ≥ 600 *ns*, in the magnetic field case, there is an increase in the intensity of the 510 line relative to the 521+522 and 515 lines, as clearly showed in Fig. 4.8(b). This feature also was observed in the experiment described in Chapter 3, for plasma expanding in a transverse magnetic field. As

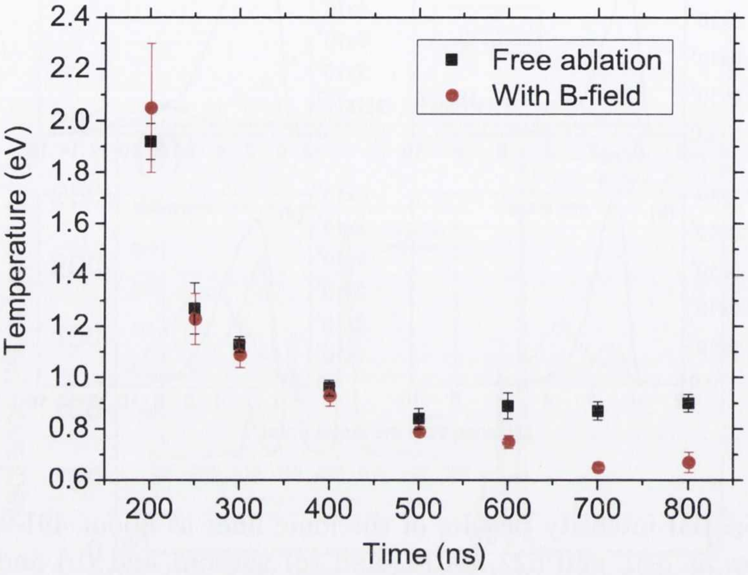

Figure 4.10: Temperature profile without and with magnetic field as a function of time at 2 *mm* from the target surface.

already showed in the previous chapter, this change in the relative intensity of the neutral lines is indicative of a lower electron temperature.

The evolution of the electron temperature was found by using a Boltzmann plot method. According to the plasma density profile derived from the ion signal in Fig. 4.4(a) in the free ablation case, it was found that at 2 *mm* from the target the McWhirter criterion is satisfied for delay time $\leq$ 800 *ns*. Since the plasma density is expected to be significantly higher when the magnetic field is present as consequence of the lateral confinement of the plasma, LTE also applies in the same time and space domain as without the field. Fig. 4.10 shows the temporal variation of T_e at 2 *mm* from the target for both free ablation and ablation in the magnetic field. As expected, it can be seen that at late time, $\geq$ 600 *ns*, T_e is slightly lower in the presence of the magnetic field.

4.6 Thin film depositions

To investigate the influence of the magnetic field on the amount and distribution of ablated material flowing away from the target, thin film depositions were made on

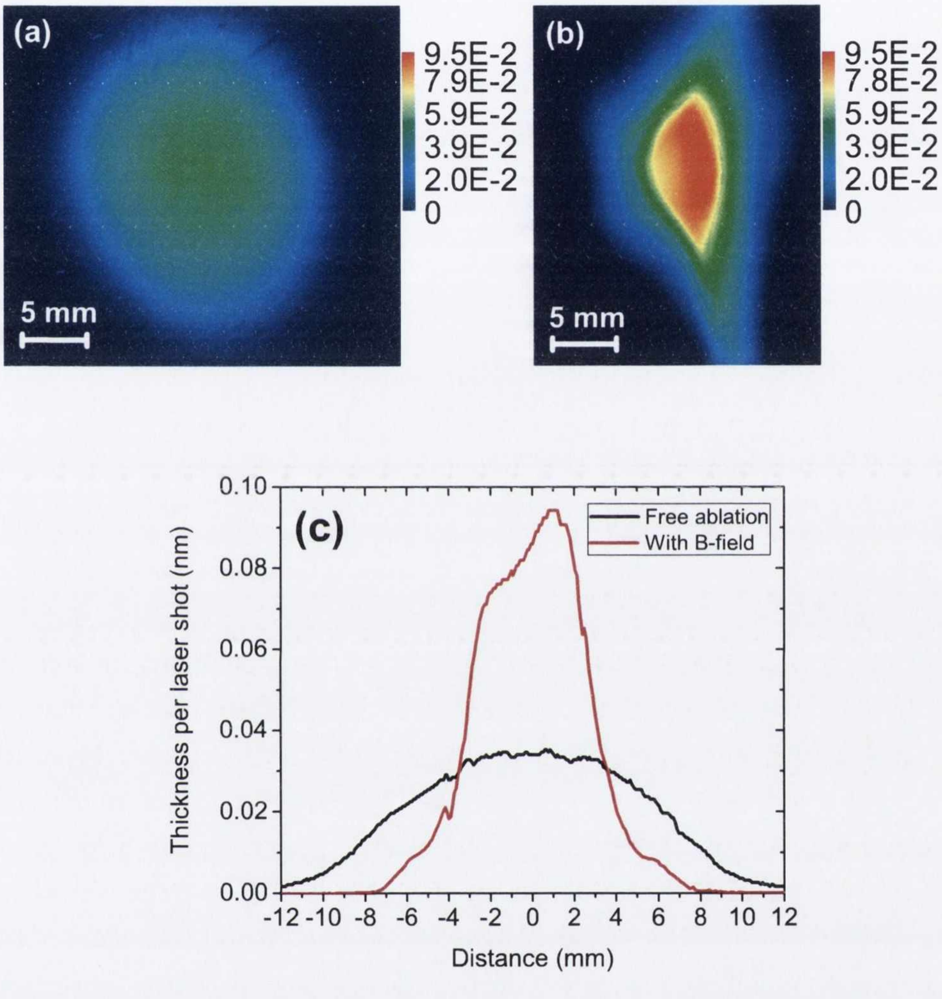

Figure 4.11: Distribution of Cu deposition per laser pulse on glass slides at 2 *cm* from the target: (a) without magnetic field, and (b) with magnetic field. The color scale indicates the thickness in nanometers; (c) comparison of the thickness profiles across the center of each thin film.

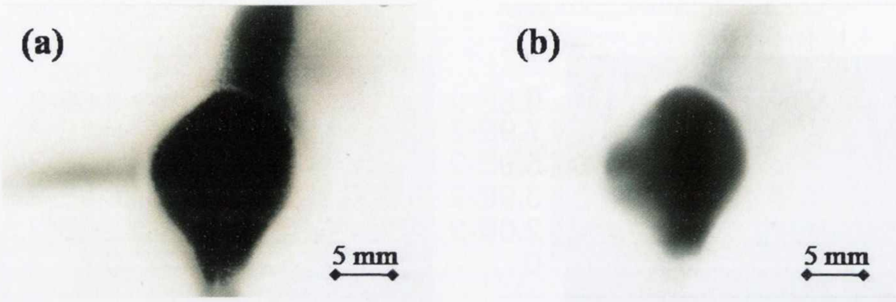

Figure 4.12: Images showing the distribution of Cu deposition on glass slides at 3.2 *cm* from target: (a) for 10000 laser shots and with the electrode at float, and (b) for 1000 laser shots and with the electrode at +10 *V*.

glass slides placed at 2 *cm* from the target. For free ablation 3000 laser shots were used, while in the magnetic field, where the deposition rate is higher, 750 shots were used. The depositions were analyzed according to the method discussed in Section 2.4. Fig. 4.11(a) and (b) show the images of the depositions for free ablation and for the magnetic field case, respectively. Fig. 4.11(c) overlaps the two cross sectional profiles of (a) and (b) at the center of both depositions. From the depositions, the followings can be noted: in the presence of a magnetic field the deposition is restricted to a significantly smaller area; the magnetic field affects the expansion of both neutral and ionic components in the plasma; the deposition rate at the center of the film is increased by a factor of ~ 2.6 and the shape of the deposition is less regular and shows fluted projections along the vertical direction, which may indicate the development of a plasma instability [4, 40].

A cylindrical electrode coaxial with the plasma expansion axis was placed midway between the magnets, with the aim of improving the collimation and also the symmetry of the plume. The electrode was 10 *mm* in diameter and 4 *mm* in length. The target was placed at $z = -16$ *mm*. Fig. 4.12 shows the deposition obtained on a glass slide placed at 3.2 *cm* from the target in two cases: (a) with no voltage on the electrode (electrode at floating potential) and (b) with +10 *V* on the electrode. As can be seen, the presence of the biased electrode further concentrates the plasma about the expansion axis. Although still irregular, an improvement is also seen in the symmetry of the distribution of material deposited.

4.7 Discussion

It has been shown that when a low temperature LPP is directed along a moderate (0.3 T) magnetic field, the lateral expansion of the plasma is severely constrained. In this regard, it was noted that the magnetic field affects the expansion of both neutral and ionic components of the plasma. Also, in the presence of the magnetic field, there is a very marked change in the relative intensities of the neutral lines. This behavior was already observed in the experiments described in the previous chapter, for a plasma expanding across a magnetic field and an explanation was offered in Section 3.4. The confinement of the neutral emission was explained by showing that there is a spatial correlation between the neutral emission and singly ionized species. It was also shown that it is the lower value of temperature with the magnetic field at late time (Fig. 4.10) which accounts for the relative enhancement of the lines at 510, 570 and 578 nm. The same arguments can be applied to the plasma expanding along the field of this scenario.

Furthermore, similarly to the discussion reported in the previous chapter, the lateral plasma confinement can be explained in terms of a simple MHD model of the interaction of the LPP with the magnetic field. From the ICCD images in Fig. 4.5, it was observed that up to delays of < 300 ns the images in the two cases, without and with magnetic field, are quite similar. The effects of the magnetic field on the plasma expansion become evident at 300 ns, when the plume begins to look more cylindrical. The plume size at which the magnetic field is expected to begin to influence the plasma flow can be estimated by equating the ram pressure, due to the plasma flow orthogonal to the field, to the magnetic pressure. The magnetic pressure for 320 mT is 4×10^4 $N\ m^{-2}$. For the free plume, the ram pressure in the z direction at the probe position (2 cm), at the time of maximum ion flux (1.2 μs), is $P_R = 1.7 \times 10^3$ $N\ m^{-2}$. For a 3-D inertial expansion, the ram pressure scales as (plume radius)$^{1/3}$ and its transverse component is k^2 times smaller than in the forward direction, where k is the aspect ratio in the x or y direction. From the images in Fig. 4.5 for the free ablation case, the aspect ratio, k_x, can be estimated and it was found to be ~ 2.6. Thus it is estimated that the ram pressure in the transverse direction will be equal to the magnetic pressure when the plume transverse radius is ~ 1.4 mm. This is close to the value of the transverse radius at 300 ns when influence of the magnetic field is first observed.

Chapter 5

Plasma expansion along a converging magnetic field

This chapter describes the results of a preliminary study aimed to investigate the effect of a combination of magnetic and electric fields on the plume expansion. A converging magnetic field parallel to the plasma flow was used and an electrode was utilized to apply the electric field.

5.1 Experimental setup

A schematic of the experimental setup is given in Fig. 5.1. The laser source was a Nd:YAG laser with 6 ns pulse width and a wavelength of 1064 nm. A silver (Ag) target was irradiated by the laser beam in a stainless steel vacuum chamber. The fluence chosen for this experiment was about 2 $J\,cm^{-2}$. The silver target was rotated to reduce drilling. The magnetic field was produced using a cylindrical Nd-Fe-B permanent magnet with a 5 cm diameter and 2 cm height. The magnet was placed in front of the target, 6 cm from the target surface, so that the plasma could flow along the magnetic field lines. The origin of the coordinate system used to describe the field is taken to be on the axis of the system and on the plane of the target surface. Fig. 5.2 shows the magnetic field calculated with COMSOL. In particular, Fig. 5.2(a) shows the magnetic field lines, Fig. 5.2(b) displays the calculated axial profile of the magnetic field and (c) shows the variation of the x

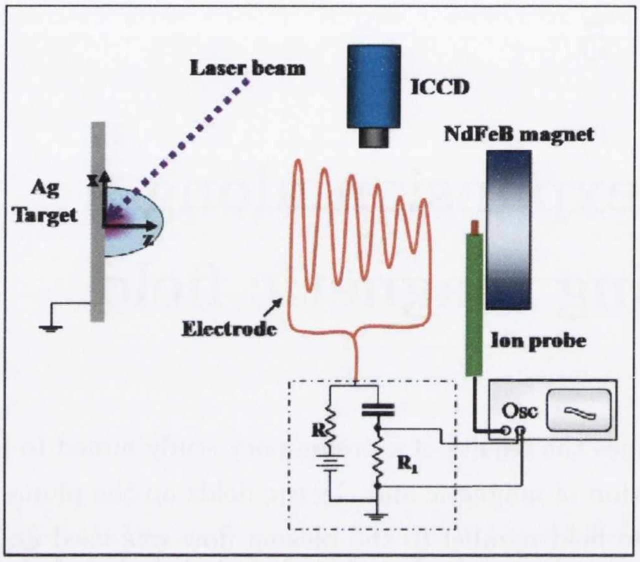

Figure 5.1: Schematic of the experimental setup. R is a load resistor of 1 $k\Omega$; R_1 is a resistor of 0.1 Ω; C is a capacitor of 1 μF; "Osc" is the oscilloscope.

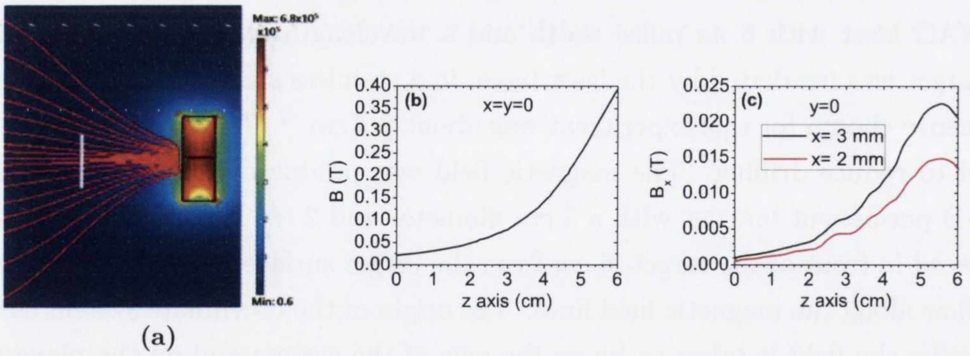

Figure 5.2: (a) Calculated magnetic field lines. The color scale indicates the magnetic field strength in T. The vertical grey line indicates the position of the target. (b) Magnetic field profile along the z axis, from the target surface, at zero position, to the magnet, at $z = 6$ cm. (c) Variation along the z axis of x-component of the magnetic field at x=2 and 3 mm.

component of the magnetic field along the z axis for $x = 2$ and 3 mm. As it can be seen, the axial magnetic field increases from a value of 20 mT at the target surface to $\sim$ 400 mT at the magnet surface. The orthogonal component of the field also increases with the distance from the target and is higher moving away from the z axis. As an example, at $x = 3$ mm, B_x is $\sim$ 1 mT at the target surface and $\sim$ 20 mT at the magnet surface.

The electric field was imposed using an electrode coaxial with the plasma expansion axis. As shown in Fig. 5.1, the electrode was made by winding a copper wire, giving a coil-like shape. It was 3 cm long with 6 turns, the smallest of radius 0.5 cm, the largest of radius 1.1 cm. The diameter of each winding was chosen to match the magnetic flux tube. The coil was connected to a capacitor placed outside the vacuum chamber. The circuit used to charge the coil is shown in Fig. 5.1.

To investigate the effects of the magnetic and electric fields on the plasma flow, time resolved optical images of the visible plasma emission as well as time-of-flight measurements were recorded. Furthermore, some simple depositions were made to analyze the amount and distribution of the deposited material. All the measurements were done in three different conditions: without magnetic and electric fields (free ablation), with magnetic field only and with both magnetic and electric fields, with the electrode at +50 V.

The set of measurements presented herein were repeated several times and they were found to be reproducible.

5.2 Langmuir ion probe measurements

A Langmuir probe of dimensions 3.28×2.08 mm was set at 5.5 cm from the target and oriented to face the plasma flow. Fig. 5.3 shows the measured ion signals for the three different cases here considered: free ablation, with magnetic field and with both magnetic and electric fields. As expected, this plot shows an increase in the ion signal when the magnetic field is present, with a further increase when the electric field is added to the magnetic field. From these ion signals, the ion yields were calculated. The values obtained and the time, t_p, of maximum ion flux are given in Table 5.1. As is clear from Table 5.1, the electrode bias causes a

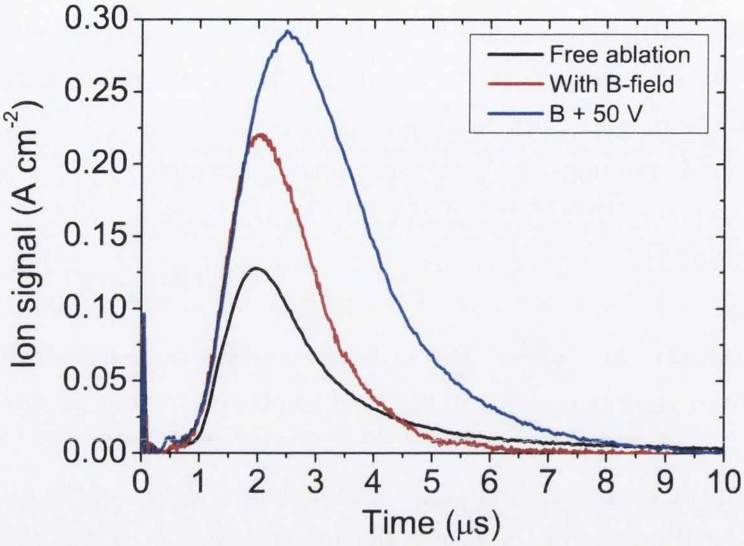

Figure 5.3: Ion signals acquired with the Langmuir probe at 5.5 *cm* from the target.

	t_p (μs)	Ion yield ($ions\ cm^{-2}$)
Free ablation	1.9	1.9×10^{12}
With B-field	2	2.6×10^{12}
With B-field + 50 V	2.5	5×10^{12}

Table 5.1: Time, t_p, corresponding to the peak ion flux and ion yield obtained from the ion signals in Fig. 5.3.

large increase in the ion yield. In fact, when the electrode is biased the ion yield is twice the ion yield obtained using only the magnetic field and is $\sim$ 2.6 times higher than the one for the free ablation. These results confirm that the magnetic field confines the lateral expansion of the plasma and that the electrode acts to further collimate it. Another interesting feature that emerges from the ion signals is the increased presence of slower ions when the fields are applied. This feature will be more clear from the ICCD images which are shown and discussed in the next section.

The current drawn from the electrode was also monitored during this experiment. Fig. 5.4 shows an example of current signal recorded at 50 V. The signal

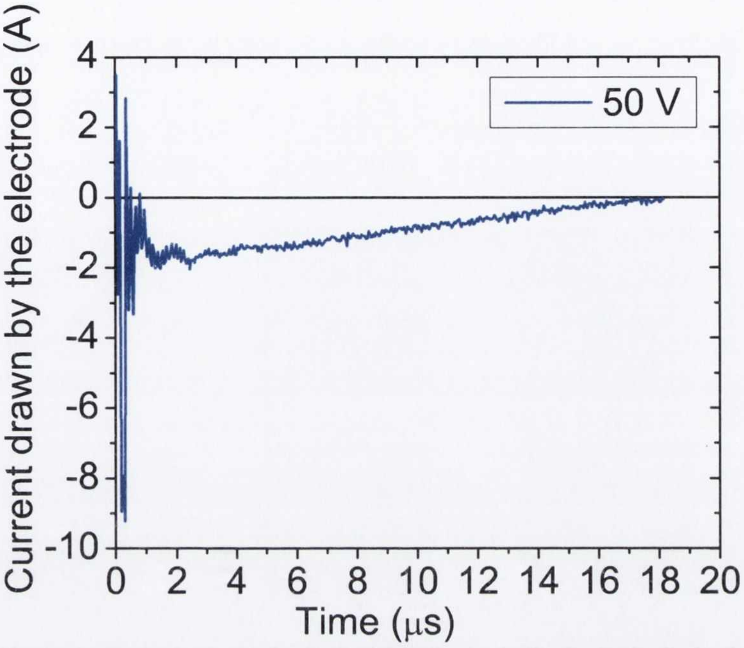

Figure 5.4: Current drawn by the electrode biased at 50 V.

presents a narrow peak at 0.25 μs and a much slower component that lasts until ~ 18 μs. The sign of the current drawn by the electrode is negative in agreement with the results reported in [7]. It seems possible that the fast electron peak is due to photoemission from the plasma causing the emission of photoelectrons from the chamber wall. These electrons are then collected by the positively biased electrode. However the behavior of the current has not been completely understood at the moment and further investigations are required.

5.3 ICCD imaging

Fig. 5.5 shows the images of the time evolution of the expanding plasma in three cases: 1) free ablation, 2) with the magnetic field and 3) with both magnetic and electric field. The ICCD imaged the region up to 5.5 cm in front of the target surface (at zero position in each image). In the free ablation case the normal semi-ellipsoidal expansion is observed. In the presence of magnetic field the dynamics of the expansion change significantly when compared to free ablation and these

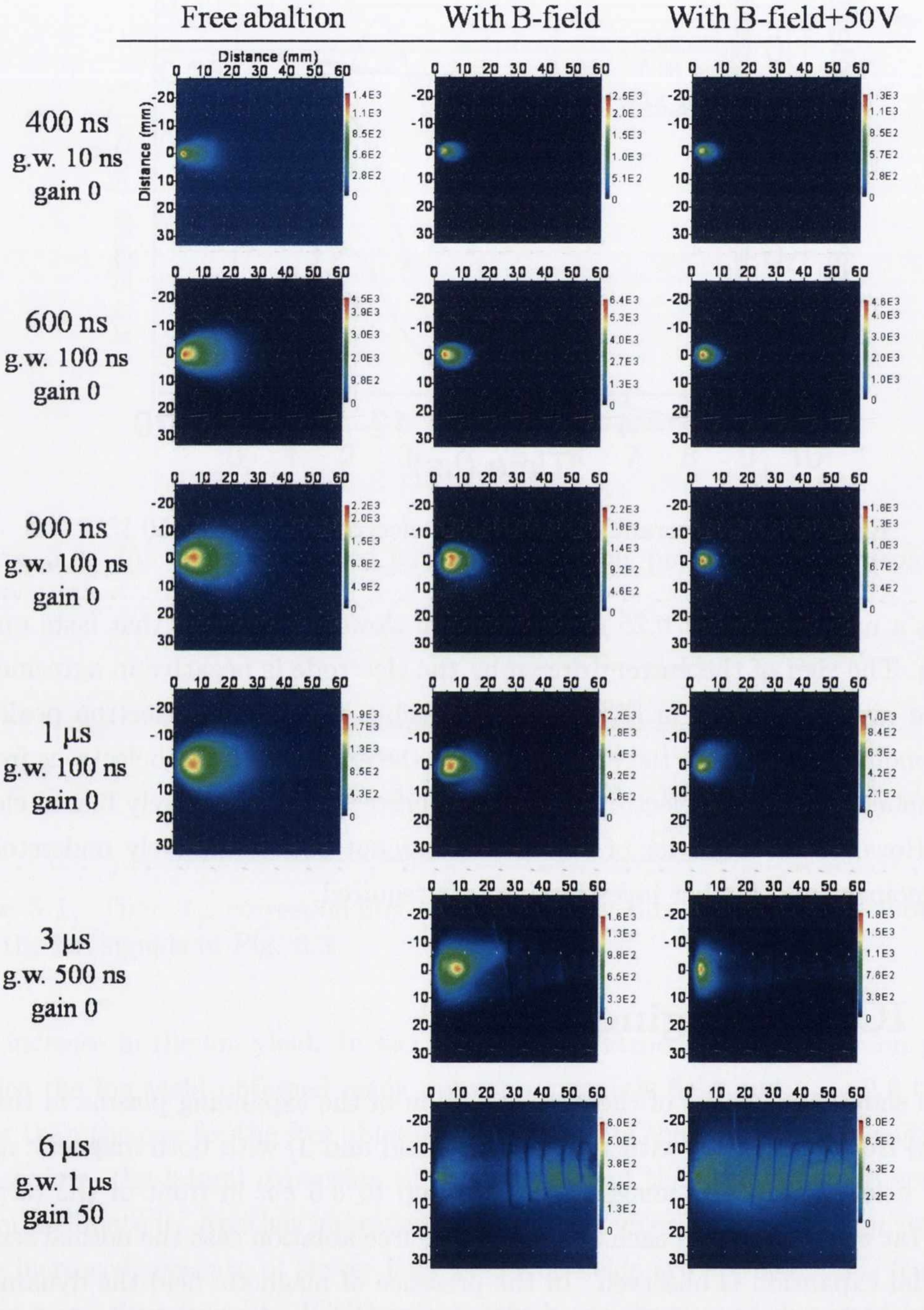

Figure 5.5: Time resolved images of the Cu plasma self-emission acquired with the ICCD without magnetic field, with magnetic field only and with both magnetic and electric field. The time delays, the gate time-width, g.w., and the gain relative to each image are indicated in the first column.

changes are further enhanced by applying voltage to the electrode. The imaging clearly shows that the magnetic field constrains the expansion to a smaller solid angle than in the case of free ablation. Another observable effect is how the rate of expansion is retarded. This is in agreement with the observed increase of slower ions in the probe signals in Fig. 5.3 and is due to the component of the magnetic field orthogonal to the expansion axis. It would seem that this relatively weak orthogonal magnetic field (Fig. 5.2(c)) near the target is acting to constrain the expansion of the plume. Moreover the positive voltage on the electrode further retards the plasma expansion. Furthermore, the plume emission is higher when only the magnetic field is present in agreement with the results of the experiments described in the previous chapter. However, surprisingly, when the electric field is added, the emission intensity is about the same as for the free ablation until time $\leq 600\ ns$ and becomes lower at later times.

5.4 Thin film depositions

The silver plasma was deposited on glass slides placed at 6 cm from the target. The depositions were realized with 30000 laser shots at a fluence of 2 $J\ cm^{-2}$. Samples of these are shown in Fig. 5.6(a) for the three different cases considered. The deposition profile was found by measuring the optical transmission of the film and is displayed in Fig. 5.6(b). It is clear from these figures that the magnetic field has a significant influence on the amount of material deposited and on its distribution. In agreement with the observed collimation of the plume, the deposit rate increases in the vicinity of the expansion axis by a factor of 5 compared to the normal ablation. However, contrary to our expectation, applying a voltage of 50 V to the electrode, in the presence of the same magnetic field, reduced this effect. In this case, the increase of the deposit rate is of a factor of 3 compared to the free ablation rate. Moreover the spatial distribution reveals some complex structures. With the magnetic field and magnetic field plus positive bias the deposition is quite non uniform. It seems that the film has been eroded in certain areas. The reason is not clear, but perhaps the plasma focusing is subject to instability [4]. Also there is a voltage of 50 V between the center and the edge of the plasma and the film may be acting to short that voltage and heat the material deposited.

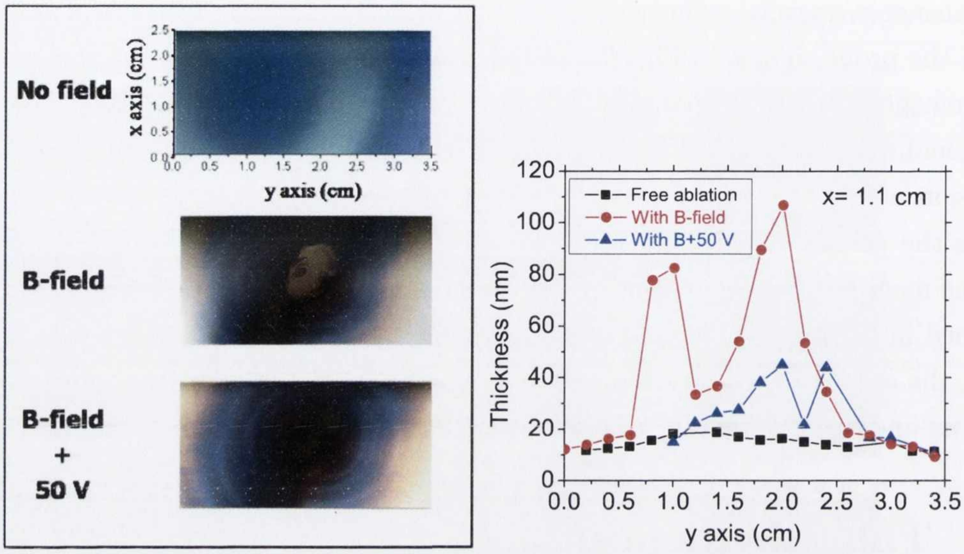

(a) (b)

Figure 5.6: Depositions of silver on glass slides placed at 6 *cm* from the target. 30000 laser shots at 2 $J\ cm^2$ were used to make these depositions. (a) Optical images of the depositions and (b) measured thickness.

Chapter 6

Focusing of LPP with a plasma lens

The main objective of the experiments described in this chapter was to characterize the laser produced plasma going through a plasma lens (PL), in an attempt to focus or collimate the plasma. Langmuir ion probe measurements and thin film depositions were used to study the plume expansion.

6.1 Experimental setup

A schematic of the experimental setup is shown in Fig. 6.1. The origin of the coordinate system used to describe the field is taken to be on the axis of the system and on the plane of the target surface, as shown in Fig. 6.1(a). The magnetic field configuration was designed using COMSOL [63] and is shown in Fig. 6.2. The plasma lens had an aperture of 10 *mm* and a length of 3.4 *cm*. The plasma lens entrance plane was placed at 4.2 *cm* from the target surface. As shown in Fig. 6.1(b) the plasma lens used consisted of five electrodes inserted in the magnetic field of the permanent magnets. The design of the plasma lens was based on the studies of Goncharov and co-workers discussed in Section 1.2.3. In order to produce the optimum magnetic field configuration, three Nd-Fe-B ring magnets alternated with four iron rings were used. Both iron and magnets had external diameter of 45 *mm* and internal diameter of 15 *mm*. The length of the central magnet was 8 *mm*;

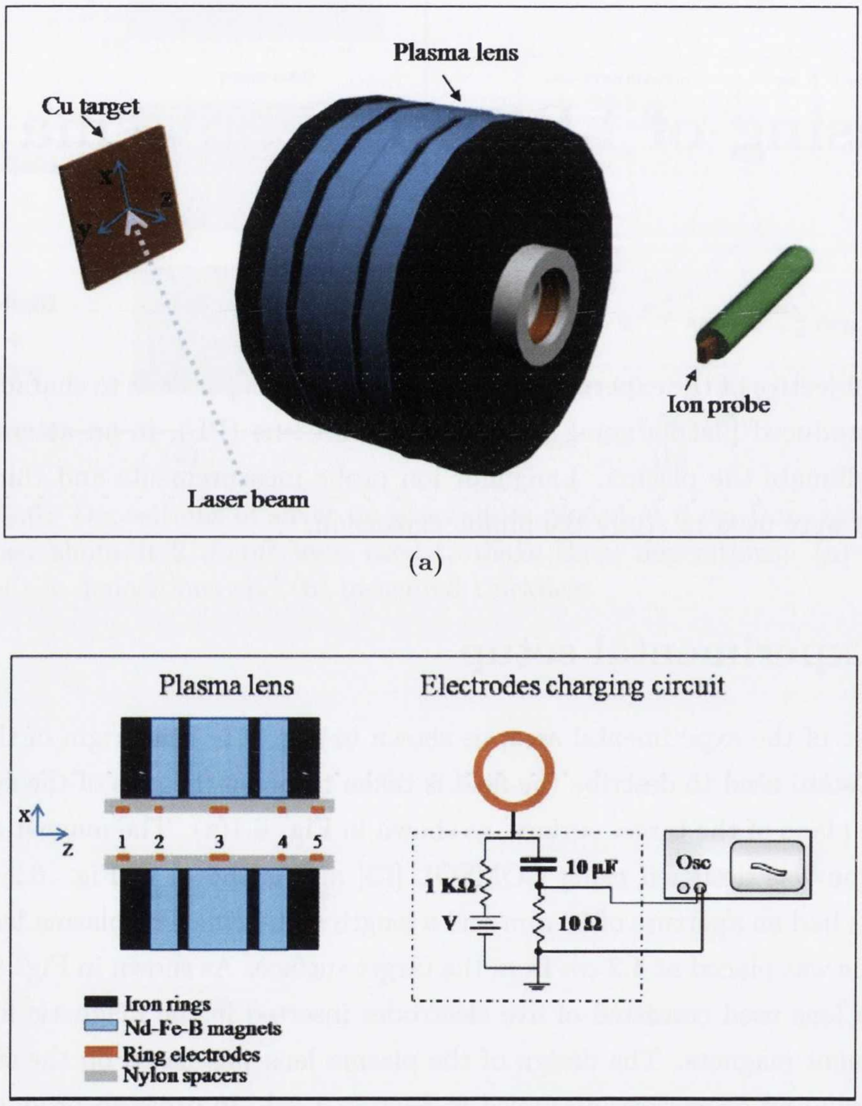

(a)

(b)

Figure 6.1: (a) Schematic of the experimental setup and (b) schematic of the plasma lens.

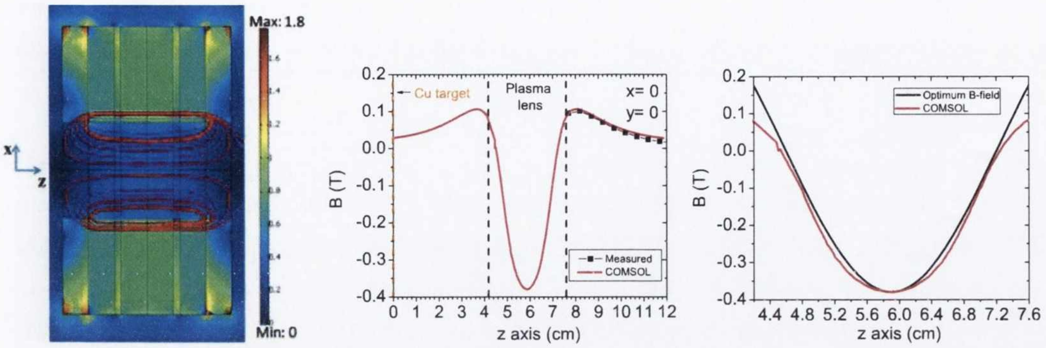

(a) (b) (c)

Figure 6.2: (a) Magnetic field lines inside the plasma lens in the x-z plane calculated with COMSOL. (b) Calculated magnetic field profile along the z axis. The target position ($z = 0$) is indicated by the orange dashed line, while the two black dashed lines mark the position of the plasma lens entrance and output, respectively at $z = 4.2\ cm$ and $z = 7.6\ cm$. Outside the plasma lens the calculated field is compared with the one measured. (c) Comparison between the calculated magnetic field inside the plasma lens (shown in (b)) and the optimum magnetic field given by equation (1.57).

while for the two other magnets it was 4 mm. The two iron rings attached next to the central magnet had length of 1 mm, while the two external iron rings had length of 4 mm. Fig. 6.2(b) shows the magnetic field profile along the z direction calculated with COMSOL. The magnetic field outside the PL was also measured with a Hall probe and found to be in good agreement with the calculated field. In Fig. 6.2(c) the axial magnetic field profile is compared with the optimum field as given by equation (1.57). The maximum magnetic field strength is at the center of the plasma lens, where it has an absolute value of $\sim 380\ mT$. At the target position, $z = 0$, the magnetic field strength is about 28 mT and at the plasma lens entrance, $z = 4.2\ cm$, it is 43 mT.

Five copper ring electrodes were introduced inside the hole of the magnet+iron rings to produce the electric field. The electrodes were mounted in a nylon tube, to provide insulation between the magnets and the electrodes. Nylon rings spacers were also used to separate and insulate the electrodes from each other. The total length of the nylon spacers+electrodes was 3.4 cm. The electrodes had a diameter of 10 mm. Electrodes 1 and 5 in Fig. 6.1(b), were 2.5 mm long and will be referred here as external electrodes or EE. Electrodes 2 and 4 were 2.5 *mm* long and will be referred as lateral electrodes or LE. Finally, the electrode 3 is the central electrode, CE, and it was 4 *mm* long. The central and lateral electrodes were connected to a capacitor placed outside the vacuum chamber. The circuit used to charge the electrodes is shown in Fig. 6.1(b). Two of these circuits were used: one for the central electrode and one for the two lateral electrodes, which were connected together. The two external electrodes were grounded. Measurements were done with all the electrodes at floating potentials and also for different potential distributions. When voltages were applied, the central and lateral electrodes were positively biased (with higher voltages on the central electrode) while the two external electrodes were always grounded. As shown in Fig. 6.1(b), the signals across the resistor of 10 Ω were acquired to monitor the current drawn by the central and lateral electrodes during the plasma flow inside the PL.

A 248 *nm* , 20 *ns* excimer laser was used to irradiate the Cu target in a stainless steel vacuum chamber at pressure of approximately 10^{-4} *mbar*. The laser spot area was 0.02 cm^2 giving a fluence of about 4 $J\ cm^{-2}$. The target was rotated to reduce drilling.

In the experiments described in this chapter the main interest was the characterization of the plasma leaving the PL. Since the exit plane of the PL was quite far from the target surface ($z = 7.6\ cm$), the plasma exiting the PL had a very weak emission. Therefore, it was not possible to use optical emission spectroscopy and fast imaging as diagnostic techniques. Hence Langmuir ion probe and depositions were the main diagnostics used in these experiments. The Langmuir probe used here was a $2 \times 2\ mm^2$ planar probe. For most of the measurements presented here, the probe was placed on the z axis at 10 *cm* from the target (i. e. at 2.4 *cm* from the exit of the plasma lens) and oriented to face the target.

6.2 Langmuir ion probe measurements

First, the electron temperature was measured to characterize the plasma in the free ablation case. In order to do that the probe was placed at 10 *cm* from the target surface and oriented parallel to the plasma flow. As discussed in Section 2.2.1, the parallel orientation of the probe gives a more reliable measurement of the

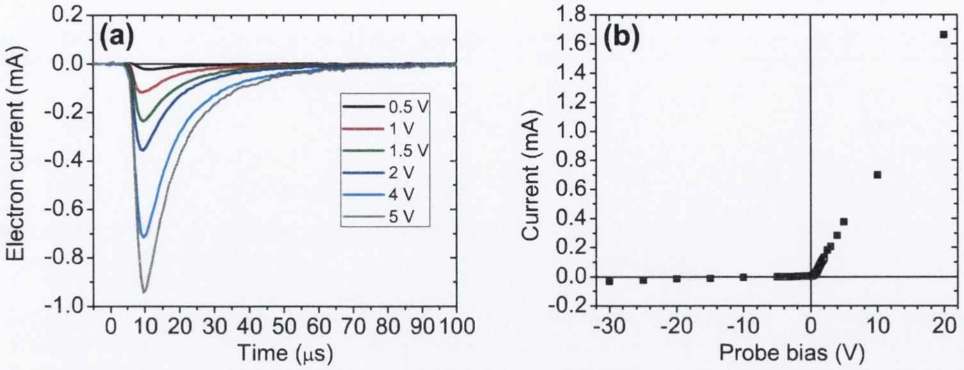

Figure 6.3: (a) Electron signals acquired at different probe bias in the free ablation case. The probe was oriented parallel to the plasma flow and was placed at 10 *cm* from the target. (b) I-V characteristic obtained at 20 μs.

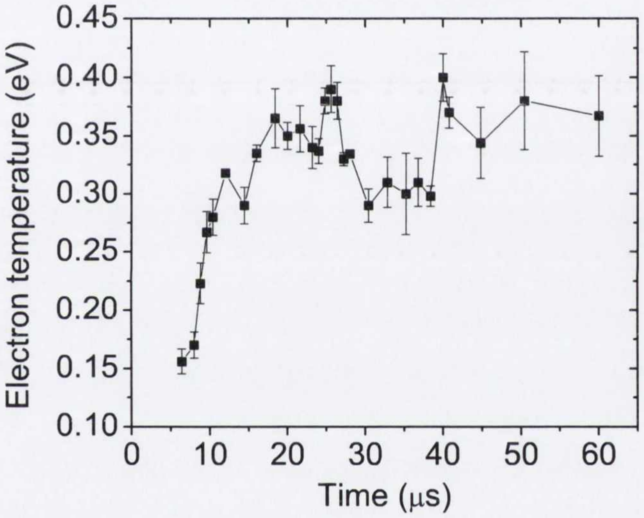

Figure 6.4: Electron temperature variation determined from a range of I-V characteristics with the probe parallel to the plasma flow.

electron temperature than the perpendicular orientation [60]. The probe bias was varied from negative to positive voltages. As an example, Fig. 6.3(a) shows some electron signals acquired at different positive voltages on the probe. If at a specific time the value of the measured current is plotted versus the applied voltage, the I-V characteristic is obtained. Fig. 6.3(b) shows the I-V characteristic obtained for a TOF of 20 μs. According to equation (2.2), the electron temperature at the

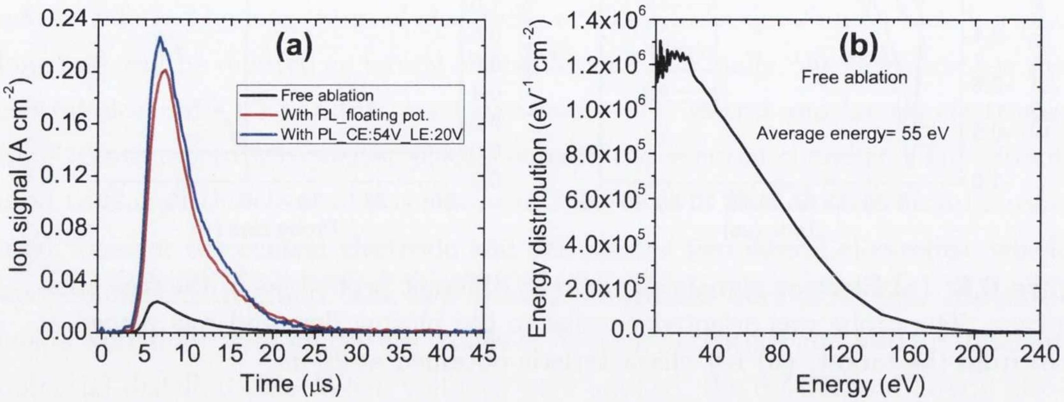

Figure 6.5: (a) Ion current density acquired with the Langmuir probe at 10 cm from the target and a laser fluence of 4 $J\,cm^{-2}$. The signals were acquired in three different cases: 1) free ablation; 2) with the plasma lens and the five electrodes at floating potentials and 3) with the plasma lens with the central electrode, CE, at 54 V, the lateral electrodes, LE, at 20 V and the external electrodes, EE, grounded. (b) Energy distribution in the free ablation case.

chosen time is then found from the slope of the semi-logarithmic plot of the I-V curve in the electron-retarding region. Repeating this procedure for several TOFs, the temperature as function of the time is obtained and is shown in Fig. 6.4. As it can be seen, the electron temperature is found to be about $0.3 - 0.4\ eV$.

For the rest of the following measurements the probe was oriented perpendicular to the plasma flow. Fig. 6.5(a) shows the ion current density at 10 cm from the target recorded on the Langmuir ion probe for three different cases: 1) free ablation; 2) with the plasma lens and no voltage on the electrodes (electrodes at floating potentials); 3) with the plasma lens with the following voltage distribution on the electrodes: 54 V on the central electrode, 20 V on the two lateral electrodes and 0 V on the two external electrodes. In the free ablation case, the maximum in the ion flux occurs at 6.4 μs. This corresponds to an ion velocity of $1.6 \times 10^{6}\ cm\,s^{-1}$ and ion energy of about 80 eV. Fig. 6.5(b) shows the ion energy distribution obtained in the free ablation case. The average energy is about 55 eV, but it can be seen that the ion energies range up to about 200 eV. Conversely, when the plasma lens is present, the TOF at the maximum ion flux occurs at slightly later times, specifically at 7.2 μs with a floating potential and at 6.6 μs

with an applied voltage. However, in this case it is not possible to give a reliable estimate of the ion energies. This is because it is likely that the plasma in the PL is accelerated during some part of the flight and decelerated in another. Already in the experiment described in the previous chapter, it was shown that the relatively weak magnetic field near the target was acting to retard the rate of the forward expansion of the plume and that this effect was enhanced by applying positive voltage to the electrode. It is possible to apply the same reasoning to the converging magnetic field between the target and the PL entrance of this scenario. This effect would act to decelerate the plasma before entering the PL. The positive voltage on the electrodes would act to further increase this effect. As a consequence of this, the assumption of constant velocity might not be a good approximation for the plasma expanding into the PL.

From Fig. 6.5(a) it can be seen that with the plasma lens a much higher ion current was recorded. The peak ion current density with the plasma lens electrodes at floating potential is about 9 times higher than the free ablation case and a further small increase is obtained with voltage on the electrodes. Assuming the ions to be mainly singly charged, the ion yields were calculated from the signals in Fig. 6.5(a). The values are: for the free ablation case $\sim 9.8 \times 10^{11}\, ions\, cm^{-2}$; with the plasma lens electrodes at floating potentials $\sim 9.5 \times 10^{12}\, ions\, cm^{-2}$ and in the third case considered here $\sim 9.7 \times 10^{12}\, ions\, cm^{-2}$. Hence, the plasma lens causes an increase by a factor of ~ 10 in the ion yield compared with the free ablation case. This increase indicates that the ions are strongly concentrated towards the expansion axis.

The influence of the potential distribution on the ion probe signals was investigated by varying the voltage applied to the electrodes. Also, for each potential distribution probe measurements were done at different distances by moving the probe in both the y and z directions. Fig. 6.6 shows a sample of ion signals acquired at several potential distributions with the probe at $10\, cm$ from the target. The measured current of these signals is lower than the one shown in Fig. 6.5(a). This is because of day-to-day variation of the laser pulse duration. Contrary to our expectation, the applied voltage seems to have very little effect on the ion signals. The value and the TOF of the peak ion current density are about the same for the different voltage distributions. The most evident effect is on the tail

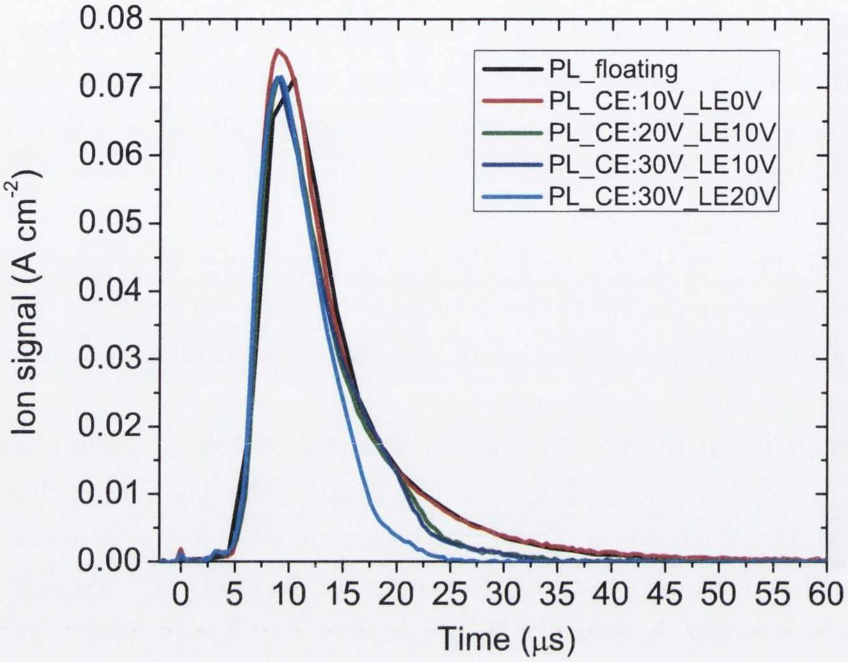

Figure 6.6: Ion current densities acquired with the Langmuir probe at 10 *cm* from the target, i.e. 2.4 *cm* from the PL exit, at several potential distributions. The signal in black was acquired with all the five electrodes at floating potential. For the other signals the external electrodes were grounded and the voltage on the CE and LE are indicated in the figure legend.

of the ion signal, which becomes shorter as the voltage is increased. This effect could be due to the reflection of lower energy ions back towards the target for the combined effect of magnetic and electric fields or it could be related to the fact that ions of different energies will not be focused on the same plane. Lower energy ions are expected to be focused by the plasma lens at shorter distances from the target compared to the more energetic ions. Hence ions focused before the probe plane will arrive at the probe plane as a diverging beam. The fraction of these ions should then increase moving further from the expansion axis.

In order to clarify this point, ion probe measurements were taken at several distances from the expansion axis. The probe was placed at $z = 10$ *cm* and moved along the y direction. To better compare the profiles of the ion signals acquired at different distances and voltages, the signals were normalized and are shown in Fig. 6.7. As can be seen in Fig. 6.7(a), for the free ablation case, the shape of

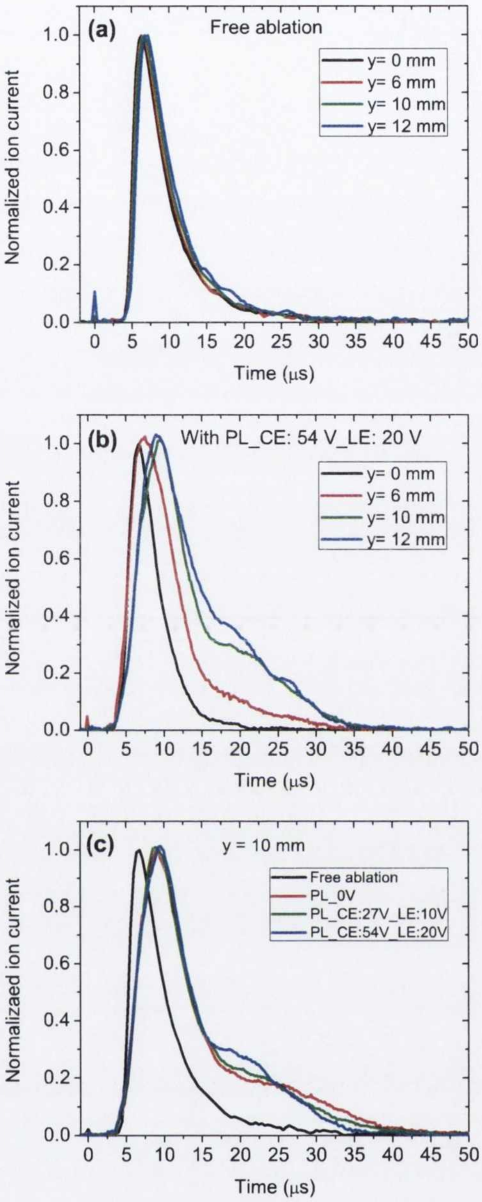

Figure 6.7: Normalized ion signals acquired with the probe at $z = 10$ cm and at different y-positions (a) in the free ablation case; (b) with the plasma lens with the following voltage distribution: 54 V on the central electrode, 20 V on the lateral electrodes and 0 V on the external electrodes. (c) Comparison of the normalized ion signals at $y = 10$ mm for different voltage distributions (the external electrodes were always grounded).

the normalized signals does not change with the distance. A very different behavior was observed when the PL was used. In this case, the ion profiles change as the distance from the z axis is increased. Specifically, from Fig. 6.7(b), it can be seen that at $y = 6\ mm$ a second component appears at times $\geq 15\ \mu s$ and at $y = 12\ mm$ a third component appears at time $\sim 26\ \mu s$. Also, the fraction of slower ions increases with increasing lateral distance. Fig. 6.7(c) shows the normalized ion signals at $y = 10\ mm$ in the free ablation case and for several potential distributions on the plasma lens. Two main features can be noted. First, the maximum ion flux of the plasma after going through the PL occurs at later times when compared with the free ablation case. Second, increasing the voltage applied to the lens electrodes causes the slower ion component to move towards shorter times. The first point made above together with the behavior described in Fig. 6.7(b) seems to support the hypothesis that lower energy ions are focused before the probe plane. However the dynamics of the plasma expanding into the PL are quite complex and not fully understood. It seems clear though that the plasma lens changes both the trajectories and energies of the expanding plasma as indicated by the TOF measurements.

Also very interesting is the variation of the ion yield as a function of the distance, Fig. 6.8. These ion yields were calculated from the ion signals acquired at different y-distances. As it can be seen, the plasma lens has a dramatic effect on the ion distribution. While in the free ablation case, the distribution is fairly uniform, with the plasma lens it is strongly peaked, indicating that the plasma is being focused. The peak ion yield with the electrodes at floating potential is 4 times higher than the one for free ablation. Applying voltage on the plasma lens electrodes a further increase is observed. However, the value of the voltage seems not to influence the ion yield profile and for all the voltages (including the case when the five electrodes are at $0\ V$) the peak ion yield was 5 times higher than the one for free ablation.

The Langmuir ion probe was also moved along the z axis to acquire ion signals at different distances from the plasma lens exit. From these signals the ion yields were calculated and they are shown in Fig. 6.9. It is evident that with the plasma lens a much higher ion yield is obtained compared with the free ablation. However it is also clear that this increase is not constant, but it decreases with the distance

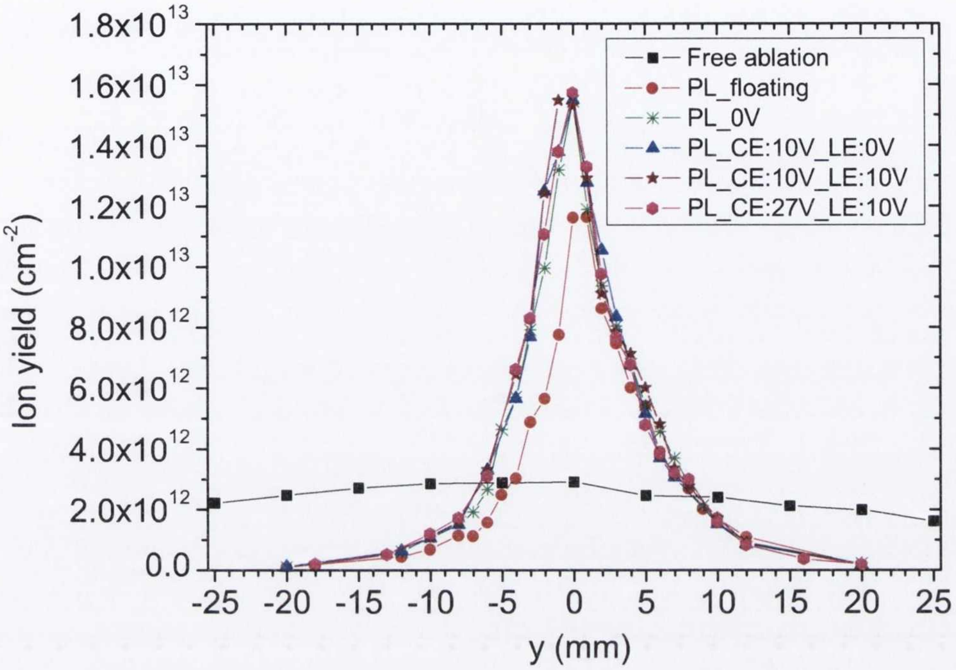

Figure 6.8: Ion yield variation along the y axis at $z = 10\ cm$.

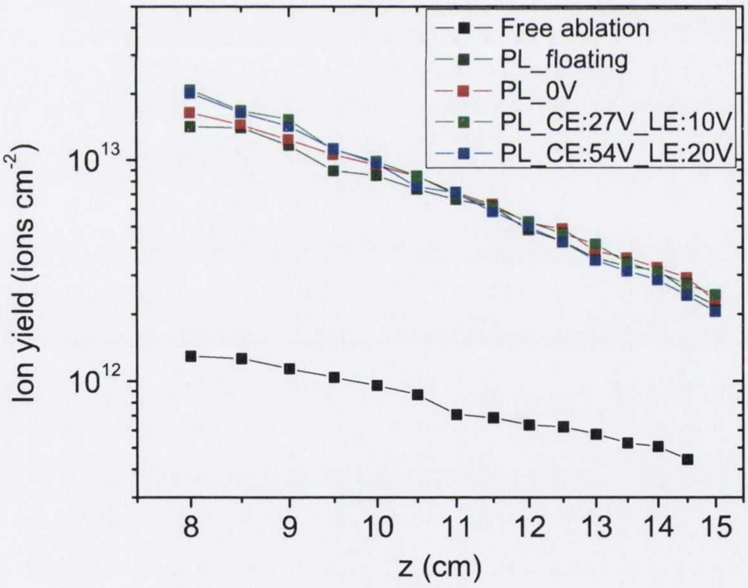

Figure 6.9: Ion yield as a function of the distance from the target for the free ablation case and for the plasma exiting the PL for several potential distributions. Both axis are on a logarithmic scale.

from the target. From the curves in Fig. 6.9 the slope of the logarithm of the ion yield as function of the logarithm of the distance was estimated. In the free ablation case, in absence of recombination, the ion yield decreases as the (distance from the target)^2. Hence the slope is expected to be ~ -2. From Fig. 6.9 the slope in the free ablation case was found to be is $\sim -1.85 \pm 0.06$, which is close to the expected value. With the plasma lens, a higher slope of $\sim -3.62 \pm 0.05$ was found. Hence, the plasma lens causes the ion yield to decrease faster with the distance from the target compared with the free ablation case. The increase in the ion yield with the PL goes from a factor of ~ 16 at 8 cm to ~ 4.5 at 15 cm from the target surface. However, the origin of this behavior has not been understood yet.

6.3 Floating potential on and current drawn by electrodes

As mentioned above, the voltage across the resistor of 10 Ω in Fig. 6.1(b) was acquired to monitor the current drawn by the central and lateral electrodes during the plasma flow inside the PL. The floating potentials were also measured by connecting the electrodes directly to the oscilloscope and selecting the 1 $M\Omega$ input impedance. As shown in Fig. 6.10, the floating potentials are positive and the amplitude on the central electrode is about 2 times that on the LE. The temporal profiles of the current signals, Fig. 6.10(c) and (f), were strongly dependent on the applied voltage. For a bias of 0 V the current drawn by the electrodes is mostly positive. Increasing the voltage causes the current to become negative and clearly as the bias is increased the electron current to the electrodes increases. It is also worth noticing that the voltage on the lateral electrodes influences both the profile and the value of the current drawn by the central electrode. As an example we can look at the three current signals in Fig. 6.10(e) acquired by fixing the potential of CE to 30 V for three different LE bias. When 0 V are applied on the lateral electrodes, the current drawn by the central electrode has a single peak at about 7 μs. With 10 V on the LE, two effects can be seen on the current drawn by the CE: 1) the value of the peak current at about 7 μs is reduced from 15 mA to

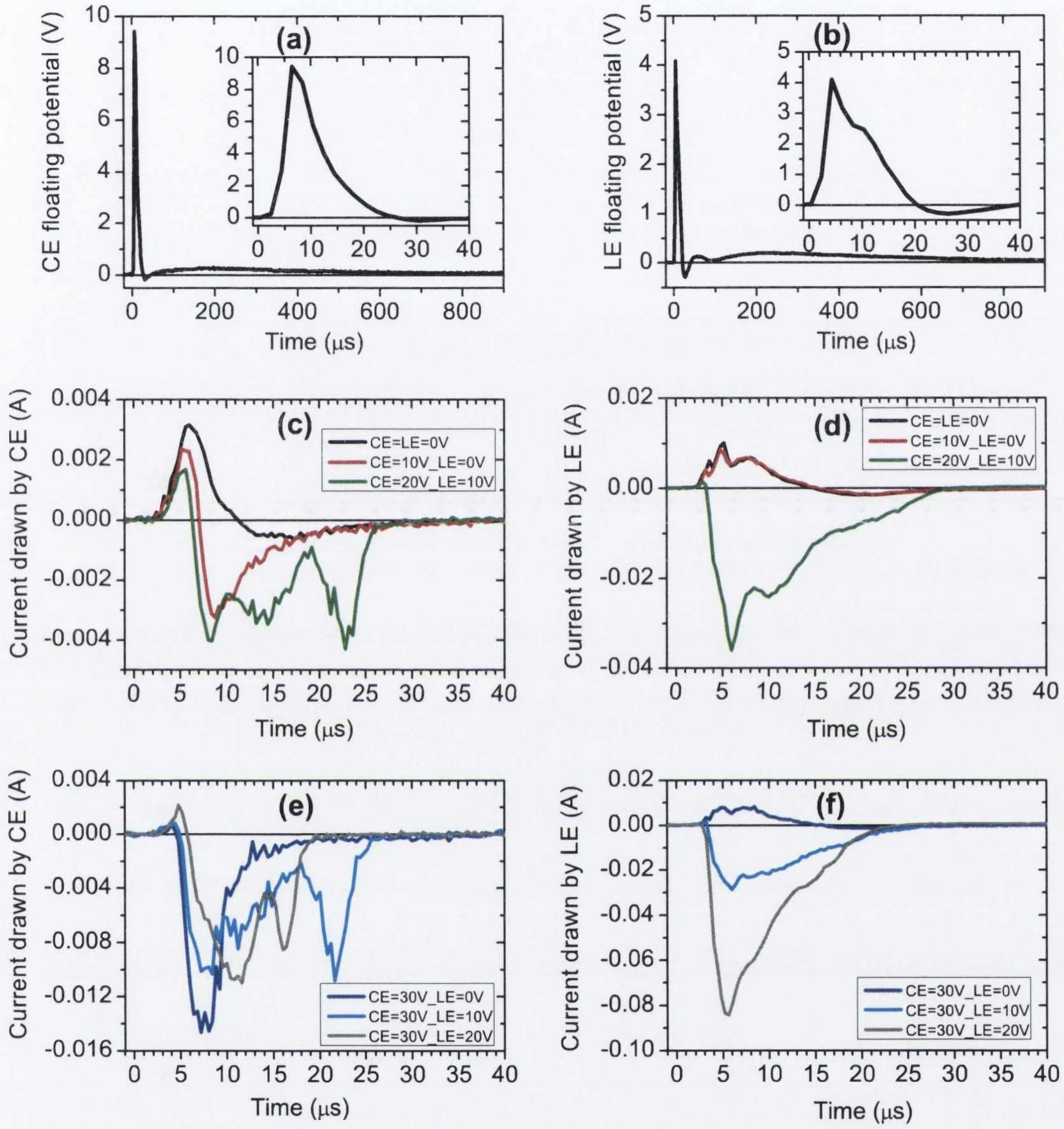

Figure 6.10: (a) and (b) Floating potentials; (c) and (e) current measured on the central electrode and (d) and (f) current measured on the lateral electrodes.

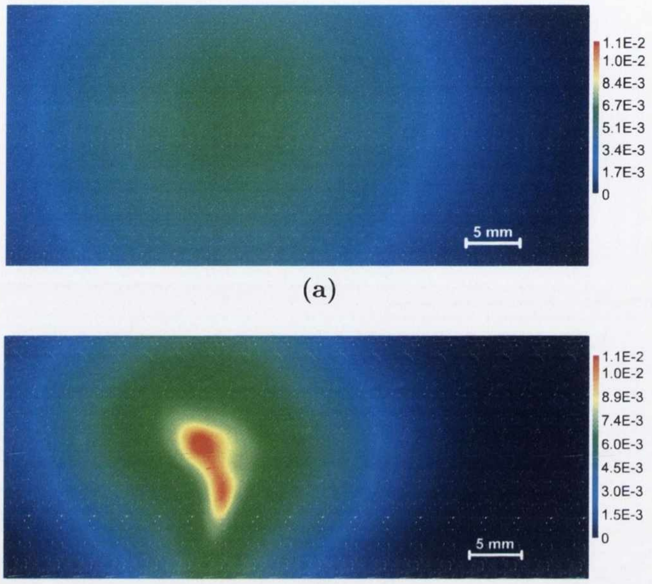

(a)

(b)

Figure 6.11: Images showing the distribution of Cu deposition per laser pulse on glass slides at 4 *cm* from the target (a) for the free ablation case and (b) with the plasma lens electrodes at floating potential. The color scale indicates the thickness in nanometers.

10 mA and 2) two more peaks at later times ($\sim$ 12 and 22 μs) appear. A further increase in the LE bias to 20 V causes a significant change in the time at which the peaks are observed.

6.4 Thin film depositions

Material distribution both entering and leaving the plasma lens was analysed by placing a glass substrate directly in front and at the exit of the plasma lens. Depositions were also done in the free ablation case. Fig. 6.11(a) and (b) show the images of the depositions done at 4 *cm* from the target surface without and with the plasma lens, respectively. For free ablation 10000 laser shots were used, while with the plasma lens, because the deposition rate is higher, 5000 laser shots were used. The total number of atoms deposited per laser shot was about the same in both cases: 2.5×10^{14} and 2.7×10^{14} without and with the plasma lens,

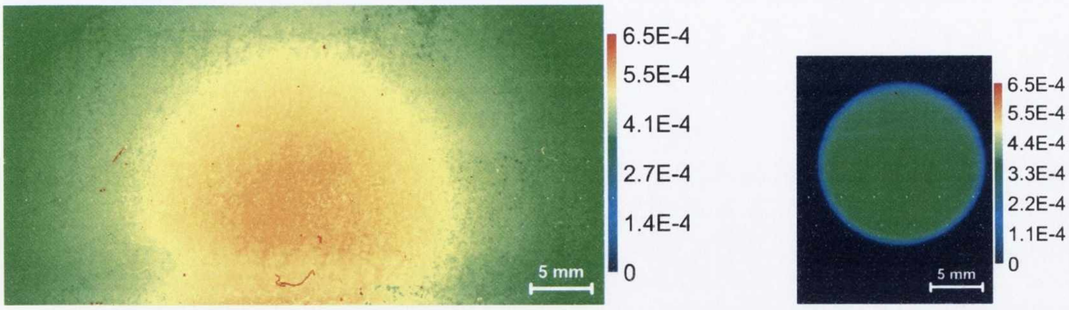

(a) Free ablation **(b)** Free ablation

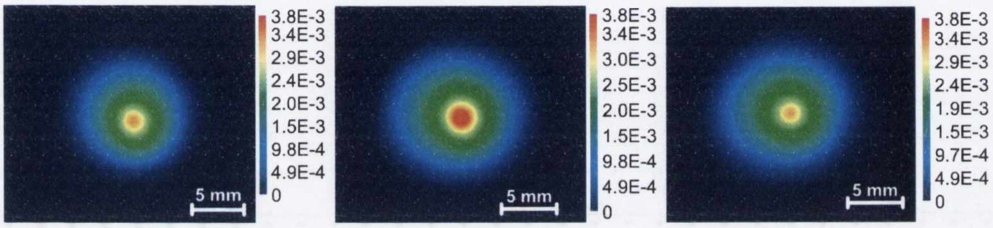

(c) PL at floating potential **(d)** PL at 0 V **(e)** PL at EC: 27 V; EL: 10 V; EE: 0 V

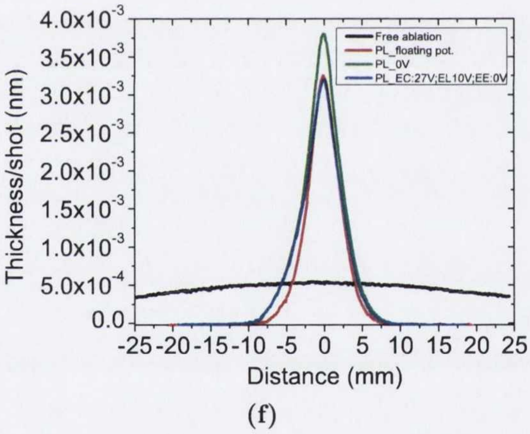

(f)

Figure 6.12: Images showing the distribution of Cu deposition per laser pulse on glass slides at 11.5 cm from target: (a) for free ablation; (b) for free ablation and with a nylon cylinder; (c)-(e) are the depositions done with the plasma lens at three different electrode potentials. The color scale indicates the thickness in nanometers. (f) Shows the comparison of the thickness profiles across the center of the thin film (a), (c), (d) and (e).

respectively. It is evident from Fig. 6.11(b) that the magnetic field outside the plasma lens has a significant effect in the distribution of the material deposited. Firstly, the deposition rate in the center of the film is increased by a factor of ~ 2.6 with respect to the free ablation case indicating a concentration of the plasma toward the expansion axis. This is a positive effect because it improves the efficiency of the PL. Secondly, the shape of the deposition is very irregular, probably as consequence of a plasma instability. This is consistent with the results of experiments described in the previous chapters. It was in fact already observed that in the case of plasma expanding along a magnetic field the distribution of the material deposited was rather asymmetrical.

Fig. 6.12 shows the depositions done at 11.5 *cm* from the target, i.e. at 3.9 *cm* from the exit of the plasma lens. In particular, Fig. 6.12(a) shows the deposition done in the free ablation case. To emulate the geometrical shape of the plasma lens, a nylon cylinder having identical physical dimensions was used as a lens substitute. In this way we can understand the effect of the geometry of the plasma lens on the amount of material deposited without the effects of its magnetic and electric fields. The deposition obtained is shown in Fig. 6.12(b). Fig. 6.12(c)-(e) show the depositions at the exit of the plasma lens for three different potential distributions. Thickness profiles across the center of each thin film done at the plasma lens exit are compared with the free ablation profile in Fig. 6.12(f). The plasma lens has a dramatic effect on the distribution and amount of material deposited and these effects are consistent with the probe measurements. The depositions clearly show that the plasma lens has a strong focusing effect on the expanding plasma. Also, the deposition rate in the center of the film is increased by a factor of $\sim 6-7$ compared to the free ablation case and by a factor of $\sim 12-13$ when compared with the deposition done placing a nylon tube between the target and the substrate. The analysis of the depositions also confirmed that the voltage on the electrodes does not have a substantial influence on the overall plasma dynamics. Another very important feature that should be noted is that the material deposited at the PL exit has a very regular axi-symmetric distribution. This suggests that, although the plasma entering the PL is unstable, the focusing of the plasma is hydrodynamically stable. Hence the plasma lens has the effect of removing the instability. The number of atoms deposited and the peak thickness per laser shot

Conditions	D_{T-S} (cm)	*Material deposited* $atoms/shot$	*Peak thickness* $(cm/shot)$
Free ablation	4	2.5×10^{14}	4×10^{-10}
With PL	4	2.7×10^{14}	1×10^{-9}
Free ablation	11.5	4.7×10^{13}	5.5×10^{-11}
Free ablation with a nylon cylinder	11.5	4×10^{12}	2.8×10^{-11}
With PL at floating potential	11.5	6.4×10^{12}	3.3×10^{-10}
With PL at $CE = LE = EE = 0\ V$	11.5	1.1×10^{13}	3.8×10^{-10}
With PL at EC:27 V, EL:10 V, EE:0 V	11.5	1.3×10^{13}	3.3×10^{-10}

Table 6.1: Results obtained from the depositions in Fig. 6.11 and 6.12. D_{T-S} indicates the distance between the target and the glass substrate.

of each deposition are summarized in Table 6.1.

6.5 Weaker magnetic field

It has been already noted above that the bias of the plasma lens electrodes plays a marginal role in influencing the plasma expansion properties. The effect of the magnetic field in the plasma lens seems by far to exceed the effect of the electric field. Therefore a lower magnetic field was used to see if some dependence on the electrode bias could be observed in that case.

The experimental setup and the design of the plasma lens were the same as those used in the case of the higher magnetic field (Fig. 6.1), with the difference that in this case ferrite magnets were used instead of Nd-Fe-B magnets. In this way a much lower magnetic field was obtained. Fig. 6.13 shows the axial field produced with the ferrite magnets calculated with COMSOL. In this case, the

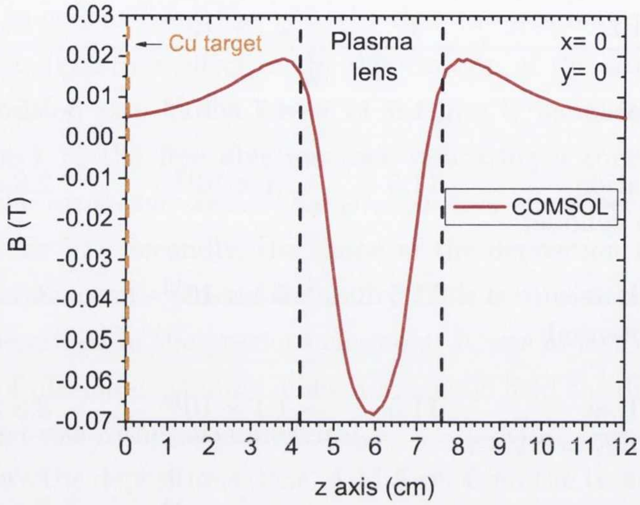

Figure 6.13: Calculated magnetic field profile along the z axis. The target position ($z = 0$) is indicated by the orange dashed line, while the two black dashed lines mark the position of the plasma lens entrance and output, respectively at $z = 4.2\ cm$ and $z = 7.6\ cm$.

maximum magnetic field strength at the center of the lens was 68 mT and the field at the target surface was 5 mT.

Langmuir probe measurements and depositions were repeated as above, but in this case with the lower magnetic field value. The overall plasma expansion dynamics did not show any substantial difference to the case of the higher magnetic field. However, these results cannot be quantitatively compared with the those obtained with the stronger B-field because of day-to-day variation of the laser pulse duration. Some examples of the ion signals and depositions under these conditions are shown below.

Fig. 6.14(a) compares the ion signals acquired at 8.5 cm from the target without and with the plasma lens. The peak current is about 8 times higher when the plasma lens is used. The ion yields calculated from these signals were $4 \times 10^{11}\ ions\ cm^{-2}$ without the plasma lens and $3 \times 10^{12}\ ions\ cm^{-2}$ with the lens. Fig. 6.14(b) shows the ions signals acquired with the plasma lens at different voltages. As for the higher magnetic field, also in this case the voltage on the electrodes had very little effect, causing only very small changes in the tail of the ion signals.

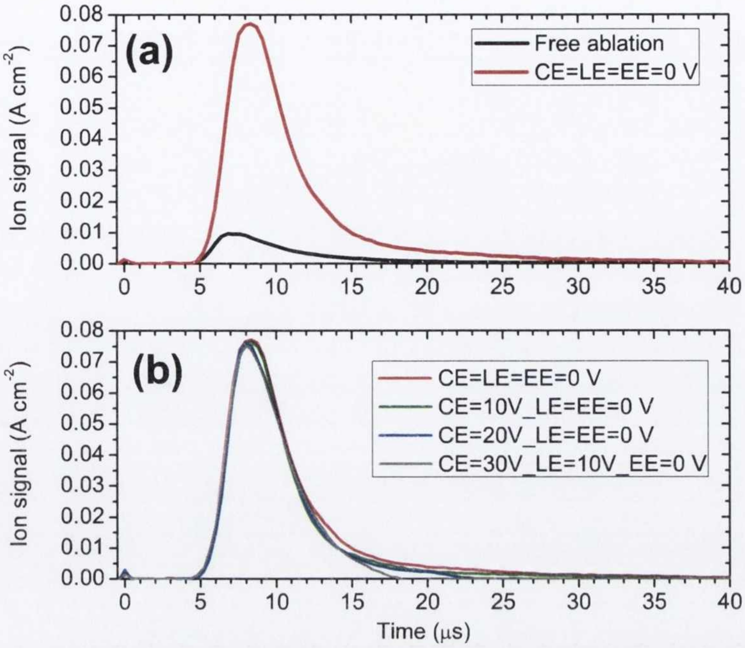

Figure 6.14: Ion current densities acquired with the Langmuir probe at 8.5 cm from the target, i.e. 9 mm from the PL exit, and a laser fluence of 4 $J\ cm^{-2}$. (a) Comparison between the signals acquired in the free ablation case and the one with the plasma lens with all the electrodes at 0 V. (b) Ion signals acquired with the plasma lens at several potential distributions.

Depositions were done at the plasma lens entrance and exit, respectively, by placing a glass substrate at 4 cm and at 10 cm from the target surface. Fig. 6.15 shows some examples of the films obtained. The films deposited show the same characteristics as those in Fig. 6.11 and 6.12. Also in the lower magnetic field case, in fact, the depositions clearly show the strong focusing effect of the plasma lens. In the presence of the plasma lens, the film thickness in the center is about 8 times higher than the one for free ablation. Also, the distribution of the material deposited at the PL input were irregular, suggesting that the plasma entering the PL is unstable; while the axi-symmetric distribution of the material at the PL output suggests that focusing is stable. The number of atoms deposited and the peak thickness per laser shot of each deposition are summarized in Table 6.2.

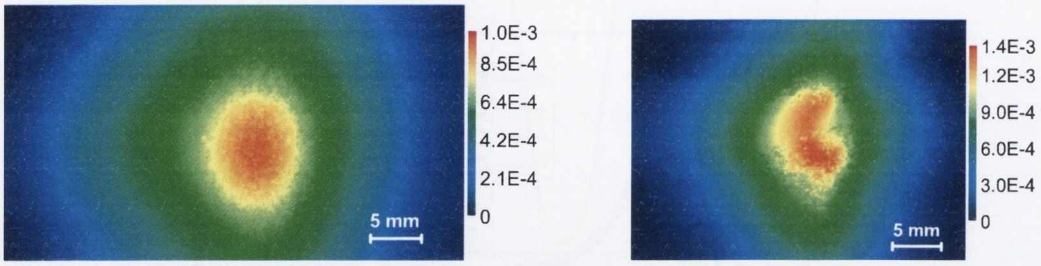

(a) Free ablation **(b)** PL at floating potential

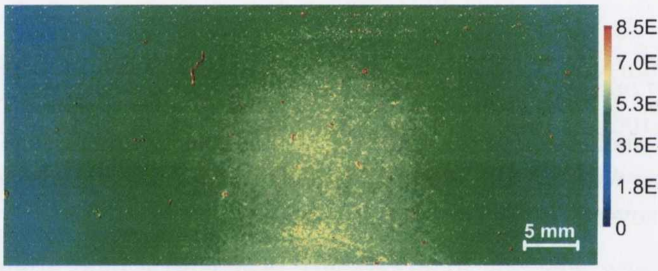

(c) Free ablation

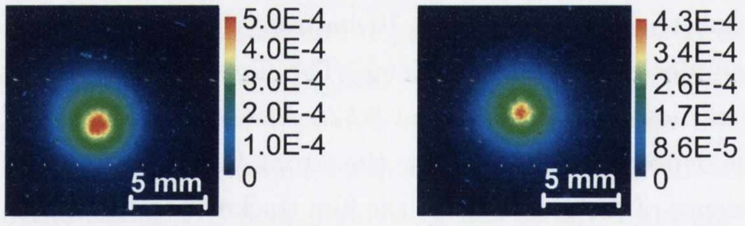

(d) PL at floating potential **(e)** PL at EC: 27 *V*; EL: 10 *V*; EE: 0 *V*

Figure 6.15: Images showing the distribution of Cu deposited per laser pulse on glass slides. (a) and (b) show the deposition done at 4 *cm* from the target for the free ablation and with the plasma lens at floating potential, respectively. (c), (d) and (e) are the depositions done at 10 *cm* from the target without and with the plasma lens.

Conditions	D_{T-S} (cm)	*Material deposited* $atoms/shot$	*Peak thickness* $(cm/shot)$
Free ablation	4	3.3×10^{13}	8.8×10^{-11}
With PL	4	2.6×10^{13}	1.5×10^{-10}
Free ablation	10	4.7×10^{12}	6.5×10^{-12}
With PL at floating potential	10	5.4×10^{11}	5×10^{-11}
With PL at EC:27 V, EL:10 V, EE:0 V	10	4×10^{11}	4×10^{-11}

Table 6.2: Results obtained from the depositions in Fig. 6.15. D_{T-S} indicates the distance between the target and the glass substrate.

Chapter 7

Conclusions and future work

In this final chapter some conclusions are drawn based on the main findings discussed in the previous chapters. Some ideas are also proposed as possible experiments to continue this research work.

7.1 Conclusions

Plume expansion dynamics were successfully modified using several magnetic and electric field configurations. A variety of diagnostics were used to study these effects and they included Langmuir probe, fast photography, optical emission spectroscopy and thin film deposition.

Time- and space resolved optical emission spectroscopy has shown that a magnetic field leads to significant enhancement of the intensity of both neutral and ion emission lines. Furthermore, it was shown that, not only the ionic, but also the neutral component of the plasma was confined by the magnetic field. While these results confirm the results of earlier experiments [12], an explanation was offered of why the neutral emission is strongly confined by the magnetic field. It was shown that the neutral emission is spatially correlated with singly ionized species through collisions. This results in a strong collisional exchange between the excited levels and the next ion. As a consequence the whole plume is guided by the magnetic field. From the temperature measurements obtained by using the relative intensity of the spectral lines, it was also observed that magnetic fields oriented orthogonal or parallel to the plasma flow cause a faster cooling of the plasma.

Time-resolved optical imaging has shown that when the LPP is directed along a magnetic field, the lateral expansion of the plasma is severely constrained. From Langmuir probe measurements and the analysis of the film depositions, the ion yield and the deposition rate was found to increase in the vicinity of the expansion axis in agreement with the observed collimation of the plume.

In particular, in a nearly uniform magnetic field, an increase by a factor of 6 in the ion yield and 2.6 in the deposition rate with respect to the free ablation case was obtained. A higher increase in the deposition rate was observed in the presence of a converging magnetic field, where the deposition showed a 5 fold increase in the film thickness. In this case it was also observed that the magnetic field decelerates the forward expansion of the plume. In this magnetic configuration also an electric field was added by applying 50 V to an electrode. It was seen that the combination of magnetic and electric field further confines the expansion of the plasma. In both configurations of magnetic field (uniform and converging) the spatial distribution of the material deposited were quite irregular suggesting the excitation of a MHD instability.

Focusing of the plasma was further investigated by using a plasma lens. The plasma lens was used for the first time with laser produced plasma and as a novel deposition device. The results obtained clearly show that the plasma lens strongly focuses the plasma. As a consequence, both ion yield and deposition rate were strongly enhanced. Ion yield up to 16 times higher than the one for the free ablation were observed. Increase in the deposition rate in the center of the film by a factor of $\sim 6-8$ was also obtained. Moreover, although the plasma entering the plasma lens was unstable, the material deposited at the plasma lens output was symmetrically concentrated around the expansion axis, indicating that plasma confinement is stable. However, it is not clear why the potential distribution on the plasma lens electrodes has only a very little effect on the plasma expansion properties.

7.2 Future work

Plasma confinement. A magnetic field orthogonal to the plasma expansion was used to confine the plasma. For this experiment time- and space-resolved optical emission spectroscopy was the main diagnostic used. Despite the strong confinement of the plasma in the forward direction, the density was found to be slightly lower in the presence of the magnetic field than the one in the free ablation case. This could be due to a significant expansion along the magnetic field lines. Fast photography and thin film depositions would help to clarify this point. Furthermore, they would reveal the presence of MHD instabilities, if any. In the experiment described in Chapter 5, it was shown that by adding an electric field to the magnetic field the deceleration of the forward plasma expansion was enhanced. Hence a combination of a magnetic field orthogonal to the plasma flow and an electric field could be investigated in order to better confine the plasma expansion.

MHD model. It has been shown that when a low temperature LPP is directed along a moderate (0.3 T) magnetic field, the lateral expansion of the plasma is severely constrained. However the depositions showed that the distribution of the material deposited is rather asymmetrical. The excitation of an MHD instability was suggested to be the cause of this distribution. Also, a novel and intriguing conical flare was observed to develop near the ablation target. It would be of interest to develop an MHD model to find a deeper understanding of these interesting features. In this regard, effort has been made during this work to initiate the development of such a model through a collaboration. However, it seems that it will take several months to complete that analysis.

Very interesting results have also been obtained in the case of plasma expanding into a plasma lens. It is therefore worthwhile to further investigate the use of the plasma lens with a laser produced plasma. Some suggestions follow.

Solenoidal magnetic field. Two different magnetic field strengths were used in this work with maxima of $\sim 400\ mT$ and $\sim 68\ mT$. From the experiments described in Chapter 6, it was shown that at the magnetic field strengths used here, no differences were observed in the plasma dynamics between the higher and the lower field case. Furthermore, while the plasma expansion was strongly influenced by the presence of a magnetic field, the external electric field had very little effect. It would then be of interest to be able to continuously change the magnetic field strength to find an optimum value and also the conditions under which, if any, the electric field starts to have a more significant effect on the plasma expansion properties. The electric field would then be an extra parameter that could be adjusted to control the plasma dynamics. A solenoidal magnetic field seems to be a more appropriate choice for this phase of investigation. In this way the magnetic field could be easily varied to find the optimum working conditions of the plasma lens.

Aperture. In an ideal case, the focusing properties of the plasma lens should not be dependent on the angular spread of the plasma entering the lens. However, if spherical aberrations are present, ions entering the lens with the same energy, but at different angles, will be focused on different planes. To investigate this point a small aperture could be placed at the plasma lens entrance. The aperture could be moved to different radial positions to select a portion of the plume expanding at different angles. Thin film depositions at the plasma lens exit could then give information on the trajectories of the selected portions of the plasma.

Curved geometry. Curved magnetic filters have been widely investigated by several authors to address the particulate contamination problem [4, 5, 6, 7]. Although particulate-free films have been produced, the deposition rates of these filters are very low because of the plasma loss at the wall. Since the focusing of the plasma by the plasma lens causes a remarkable increase in the deposition rate, it would be of interest to investigate the use of a curved plasma lens to produce particulate free thin films.

Pre-field. To increase the efficiency of the plasma lens, a magnetic or electric field or a combination of both could be used to collimate the plasma between the target and the lens entrance.

Appendix: Publications

- Focusing of a laser produced plasma by a plasma lens, in preparation.

- Lateral confinement of laser ablation plasma in magnetic field, C. Pagano and J. G. Lunney, *J. Phys D: Appl. Phys.* **43**, 305202, 2010.

- Influence of transverse magnetic field on expansion and spectral emission of laser produced plasma, C. Pagano, S. Hafeez and J. G. Lunney, *J. Phys D: Appl. Phys.* **42** 155205, 2009.

- Influence of fast electrical discharge on expansion of laser produced plasma, E. Sterling, C. Pagano and J. G. Lunney, *Appl. Phys. A* **92**, 1031, 2008.

References

[1] S. Amoruso, R. Bruzzese, N. Spinelli, R. Velotta, M. Vitiello, X. Wang, G. Ausanio, V. Iannotti, and L. Lanotte. Generation of silicon nanoparticles via femtosecond laser ablation in vacuum. *Appl. Phys. Lett.*, 84:4502–4504, 2004.

[2] R. Dolbec, E. Irissou, M. Chaker, D. Guay, F. Rosei, and M. A. El Khakani. Growth dynamics of pulsed laser deposited Pt nanoparticles on highly oriented pyrolitic graphite substrates. *Phys. Rev. B*, 70:201406(R), 2004.

[3] A. A. Puretzky, D. B. Geohegan, X. Fan, and S. J. Pennycook. Dynamics of single-wall carbon nanotube synthesis by laser vaporization. *Appl. Phys. A*, 70:153–160, 2000.

[4] A. Anders, S. Anders, and I. G. Brown. Transport of vacuum arc plasmas through magnetic macroparticle filters. *Plasma Sources Sci. Technol.*, 4:1–12, 1995.

[5] A. Anders, S. Anders, and I. G. Brown. Effect of duct bias on transport of vacuum arc plasma through curved magnetic filter. *J. Appl. Phys.*, 75(10):4900–4905, 1994.

[6] B. Alterkop, E. Gidalevich, and R. L. Boxman. Vacuum arc plasma jet propagation in a toroidal duct. *J. Appl. Phys.*, 79(9):6791–6802, 1996.

[7] R. Jordan, D. Cole, and J. G. Lunney. Pulsed laser deposition of particulate-free thin films using a curved magnetic filter. *Appl. Surf. Sci.*, 109/110:403–407, 1997.

[8] Y. Y. Tsui, D. Vick, and R. Fedosejevs. Guiding and confinement of a laser produced plasma by curved magnetic field. *Appl. Phys. Lett.*, 70(15):1953–1955, 1997.

[9] G. Radhakrishnan and P. M. Adams. Pulsed-laser deposition of particulate-free tic coatings for tribological applications. *Appl. Phys. A*, 69:S33–S38, 1999.

[10] S. Weissmantel, D. Rost, and G. Reisse. Magnetic field assisted increase of growth rate and reduction of particulate incorporation in pulsed laser deposited boron nitride films. *Appl. Surf. Sci.*, 197/198:494–498, 2002.

[11] de J. C. Ferandez, J. L. Vassen, and D. Givord. Thin film deposition by magnetic field assisted pulsed laser assembly. *Appl. Surf. Sci.*, 138/139:150–154, 1999.

[12] D. Harilal, M. S. Tillackand B. O'Shay, C. V. Bindhu, and F. Najmabadi. Confinement and dynamics of laser-produced plasma expanding across a transverse magnetic field. *Phys. Rev. E*, 69:026413, 2004.

[13] L. Dirnberger, P. E. Dyer, S. R. Farrar, and P. H. Key. Observation of magnetic-field-enhanced excitation and ionization in the plume of KrF-laser-ablated magnesium. *Appl. Phys. A*, 59:311–316, 1994.

[14] A. Neogi and R. K. Thareja. Dynamics of laser produced carbon plasma expanding in a nonuniform magnetic field. *J. Appl. Phys.*, 85:1131–1136, 1999.

[15] S. Suckewer, C. H. Skinner, H. Milchberg, C. Keane, and D. Voorhees. Amplification of stimulated soft x-ray emission in a confined plasma column. *Phys. Rev. Lett.*, 55:1753–1756, 1985.

[16] T. Pisarczyk, A. Farynski, H. Fiedorowicz, P. Gogolewski, M. Kuserz, J. Makowski, R. Miklaszewski, M. Mroczkowski, P. Parys, and M. Szczurek. Formation of an elongated plasma column by a magnetic confinement of a laser-produced plasma. *Laser Particle Beams*, 10:767–776, 1992.

[17] T. Kobayashi, H. Akiyoshi, and M. Tachiki. Development of prominent PLD (Aurora method) suitable for high-quality and low-temperature film growth. *Appl. Surf. Sci.*, 197-198:294–303, 2002.

[18] A. N. Mostovych, B. H. Ripin, and J. S. Stamper. Laser-produced plasma jets: collimation and instability in strong transverse magnetic fields. *Phys. Rev.Lett.*, 62:2837–2840, 1989.

[19] V. N. Rai, A. K. Rai, F. Yueh, and J. P. Singh. Optical emission from laser-induced breakdown plasma of solid and liquid samples in the presence of a magnetic field. *Appl. Opt.*, 42:2085, 2003.

[20] R. R. Parasad and M. Krishnan. Theoretical and experimental study of rotation in a vacuum-arc centrifuge. *J. Appl. Phys.*, 61:113–119, 1987.

[21] M. Geva, M. Krishnan, and J. L. Hirshfield. Element and isotope separation in a vacuum-arc centrifuge. *J. Appl. Phys.*, 56:1398–1413, 1984.

[22] V. S. Lisitsa and A. A. Skovoroda. On a magnetic confinement of femtosecond laser pulse plasmas. *Eur. Phys. J. D*, 38:571–574, 2006.

[23] S. Amoruso. Modelling of UV pulsed-laser ablation of metallic targets. *Appl. Phys. A*, 69:323–332, 1999.

[24] J. G. Lunney and R. Jordan. Pulsed laser ablation of metals. *Appl. Surf. Sci.*, 127-129:941–946, 1998.

[25] A. Bogaerts, Z. Chen, R. Gijbels, and A. Vertes. Laser abaltion for analytical sampling: what can we learn from modeling? *Spectrochimica Acta Part B*, 58:1867–1893, 2003.

[26] B. Wu and Y. C. Shin. Modelling of nanosecond laser ablation with vapor plasma formation. *J. Appl. Phys.*, 99:084310, 2006.

[27] D. R. Lide. *Handbook of chemistry and physics.* CRC Press, 78th edition, 1997.

[28] J. Miller and R. F. Haglund. *Laser ablation and desorption*, volume 30. Academic Press.

[29] Y. B. Zel'dovich and Y. P. Raizer. *Physics of shock waves and high-temperature hydrodynamic phenomena.* Dover, Mineola, 2002.

[30] S. I. Anisimov, D. Bauerle, and B. S. Luk'yanchuk. Gas dynamic and film profiles in pulsed-laser deposition of materials. *Phys. Rev. B*, 48:12076–12081, 1993.

[31] S. I. Anisimov, B. S. Luk'yanchuk, and A. Luches. An analytical model for three-dimensional laser plume expansion into vacuum in hydrodynamic regime. *Appl. Surf. Sci.*, 96-98:24–32, 1996.

[32] R. K. Singh and J. Narayan. Pulsed-laser evaporation technique for deposition of thin films: Physics and theoretical model. *Phys. Rev. B*, 41:8843–8859, 1990.

[33] J.G. Lunney, B. Doggett, and Y. Kaufman. Langmuir probe diagnosis of laser ablation plasmas. *J. Phys.: Conf. Ser.*, 59:470–474, 2007.

[34] T. N. Hansen, J. Schou, and J. G. Lunney. Langmuir probe study of plasma expansion in pulsed laser ablation. *Appl. Phys. A*, 69:S601–S604, 1999.

[35] J. Schou B. Toftmann and J. G. Lunney. Dynamics of the plume produced by nanosecond ultraviolet laser ablation of metals. *Phys. Rev. B*, 67:104101–8859, 2003.

[36] M. Goossens. *An introduction to plasma astrophysics and Magnetohydrodynamics.* Kluwer Academic Publishers, 2003.

[37] R. J. Goldston and P. H. Rutherford. *Introduction to plasma physics.* Institute of Physics Publishing, 1997.

[38] T. J. M. Boyd and J. J. Sanderson. *The physics of plasmas.* Cambridge University Press, 2003.

[39] F. F. Chen. *Introduction to plasma physics and controlled fusion*, volume 1. Plenum Press.

[40] B. H. Ripin, J. D. Huba, E. A. McLean, C. K. Manka, T. Peyser, H. R. Burris, and J. Grun. Sub-alfvénic plasma expansion. *Phys. Fluids B*, 5:3491–3506, 1993.

[41] A. I. Morozov. Focusing of cold quasineutral beams in electromagnetic fields. *Sov. Phys. Dokl.*, 10:775–777, 1966.

[42] D. Gabor. A space-charge lens for the focusing of ion beams. *Nature*, 160:89–90, 1947.

[43] A. I. Morozov and S. Lebedev. *Plasma optics in Reviews of Plasma Physics*, volume 8. Consultants Bureau, 1975.

[44] Yu. M. Chekh, A. M. Dobrovolsky, A. A. Goncharov, I. M. Protsenko, and I. G. Brown. Compression of large area, high-current ion beams by an electrostatic plasma lens. *Nucl. Inst. Meth. Phys. Res. B*, 243:227–231, 2006.

[45] Yu. M. Chekh, A. A. Goncharov, and I. M. Protsenko. Static and dynamic characteristics of plasma lens with modified magnetic field geometry. *Rev. Sci. Instr.*, 75:1668–1670, 2004.

[46] A. A. Goncharov, A. M. Dobrovolsky, I. M. Protsenko, G. Yu. Yushkov, and I. G. Brown. Focusing of high-current, large-area, heavy-ion beams with an electrostatic plasma lens. *Appl. Phys. Lett.*, 75:911–913, 1999.

[47] A. A. Goncharov, I.M. Protsenko, G. Y. Yushkov, and I. G. Brown. Manipulating large-area, heavy metal ion beams with a high-current electrostatic plasma lens. *IEEE Trans. Plasma Sci.*, 28:2238–2246, 2000.

[48] A. A. Goncharov, I. V. Litovko, I. M. Protsenko, and V. F. Zadorodzny. Role of aberrations in high-current plasma lenses. *IEEE Trans. Plasma Sci.*, 25:709–713, 1997.

[49] A. A. Goncharov, A. N. Dobrovolsky, A. V. Zatuagan, and I. M. Protsenko. High-current plasma lens. *IEEE Trans. Plasma Sci.*, 21:573–577, 1993.

[50] A. A. Goncharov, A. V. Zatuagan, and I. M. Protsenko. Focusing and control of multiaperture ion beams by plasma lenses. *IEEE Trans. Plasma Sci.*, 21:578–581, 1993.

[51] A. A. Goncharov and I. G. Brown. High-current heavy ion beams in the electrostatic plasma lens. *IEEE Trans. Plasma Sci.*, 32:80–83, 2004.

[52] H. R. Griem. *Principles of plasma spectroscopy.* Cambridge University Press, 1997.

[53] A. Thorne, U. Litzén, and S. Johansson. *Spectrophysics - Principles and applications.* Springer-Verlag, Heidelberg, 1999.

[54] M. Ortiz and R. Mayo. Measurement of Stark broadening for several lines of singly ionized gold. *J. Phys. B: At. Mol. Opt. Phys.*, 38:3953–3961, 2005.

[55] N. M. Shaikh, B. Rashid, S. Hafeez, S. Mahmood, M. Saleem, and M. A. Baig. Diagnostics of cadmium plasma produced by laser ablation. *J. Appl. Phys.*, 100:073102, 2006.

[56] S. Amoruso, R. Bruzzese, N. Spinelli, and R. Velotta. Characterization of laser-ablation plasmas. *J. Phys. B: At. Mol. Opt. Phys.*, 32:R131–R172, 1999.

[57] N. Konjevic and W. L. Wiese. Experimental Stark widths and shifts for spectral lines of neutral and ionized atoms. *J. Phys. Chem. Ref. Data*, 19(6):1307–1385, 1990.

[58] http://www.prism-cs.com/software/prismspect/prismspect.htm.

[59] D. W. Koopman. Langmuir probe and microwave measurements of the properties of streaming plasmas generated by focused laser pulses. *Phys. Fluids*, 14:1707–1716, 1971.

[60] B. Doggett and J. G. Lunney. Langmuir probe characterization of laser ablation plasmas. *J. Appl. Phys.*, 105:033306, 2009.

[61] R. H. Huddlestone and S. L. Leonard. *Plasma diagnostic techniques.* Academic Press, 1965.

[62] http://www.esrf.eu/computing/scientific/xop2.1/extensions.html.

[63] http://www.comsol.com/.

[64] K. Fu, M. Jogwich, M. Knebel, and K. Wiesemann. Atomic transition probabilities and lifetimes for the Cu I system. *Atomic data and nuclear data tables*, 61:1–30, 1995.

[65] http://www.nist.gov/pml/data/asd.cfm.

[66] X. Wang, S. Amoruso, and J. Xia. Temporally and spectrally resolved analysis of a copper plasma plume produced by ultrafast laser ablation. *Appl. Surf. Sci.*, 255:5211–5214, 2009.

[67] M. S. Qaisara and G. J. Pert. Laser ablation of Mg, Cu, and Pb using infrared and ultraviolet low-fluence lasers. *J. Appl. Phys.*, 94:1468–1477, 2003.

List of Figures

List of Tables